

# **Coherent Dijets in Ultra-peripheral Pb+Pb Collisions at**

$$\sqrt{s_{NN}} = 5.02 \text{ TeV}$$

By

**Samuel Steed Boren**

Submitted to the graduate degree program in Department of People who read Abstracts and the Graduate Faculty of the University of Kansas in partial fulfillment of the requirements for the degree of Doctor of Philosophy.

---

MEMBER 1, Chairperson

---

MEMBER 2, Occasional Visitor

Committee members

---

MEMBER 3

---

MEMBER 4, The One Who Never Answers Email

---

The One with an Extra Long Name

---

The Fifth Beatle

Date defended: \_\_\_\_\_ October 02, 2016 \_\_\_\_\_

The Thesis Committee for Samuel Steed Boren certifies  
that this is the approved version of the following thesis :

Coherent Dijets in Ultra-peripheral Pb+Pb Collisions at  $\sqrt{s_{NN}} = 5.02$  TeV

---

MEMBER 1, Chairperson

Date approved: \_\_\_\_\_ October 06, 2016 \_\_\_\_\_

## Abstract

This dissertation describes the study of coherent dijet photoproduction in ultra-peripheral heavy-ion collisions. Ultra-peripheral collisions have impact parameters larger  $2R$  where  $R$  is the radius of the heavy-ion. These collisions are mediated entirely by the exchange of low-virtuality photon according to the Weizacker-Williams approximation. The angular correlation of coherently photoproduced dijets is sensitive to elliptic gluon distribution. The azimuthal anisotropy of the ion recoil momentum  $P_T$  and the dijet transverse momentum  $Q_T$  is presented for two bins of  $Q_T$ :  $0 < Q_T < 5 \text{ GeV}$  and  $5 < Q_T < 10 \text{ GeV}$ .

## **Acknowledgements**

# Contents

<b>1</b>	<b>Introduction</b>	<b>1</b>
1.1	The Standard Model . . . . .	2
1.2	Quantum electrodynamics . . . . .	4
1.3	Quantum chromodynamics . . . . .	5
1.4	Deep inelastic scattering . . . . .	7
1.5	PDFs . . . . .	8
1.6	Quark gluon plasma . . . . .	10
<b>2</b>	<b>Ultra-peripheral collisions and photoproduction</b>	<b>17</b>
2.1	Ultra-peripheral heavy-ion collisions . . . . .	17
2.2	VM photoproduction . . . . .	19
2.3	Dijet photoproduction . . . . .	23
2.4	Wigner distribution . . . . .	27
<b>3</b>	<b>The CMS experiment at CERN LHC</b>	<b>29</b>
3.1	Large Hadron Collider . . . . .	29
3.1.1	ATLAS . . . . .	29
3.1.2	ALICE . . . . .	30
3.1.3	LHCb . . . . .	30
3.1.4	TOTEM . . . . .	30
3.1.5	CASTOR . . . . .	31
3.2	Compact Muon Solenoid . . . . .	31
3.2.1	Tracker . . . . .	32

3.2.1.1	Pixel tracker . . . . .	34
3.2.1.2	Strip tracker . . . . .	34
3.2.2	Electromagnetic calorimeter . . . . .	34
3.2.3	Hadronic calorimeter . . . . .	35
3.2.3.1	Hadronic forward calorimeters . . . . .	37
3.2.4	Muon detector . . . . .	38
3.2.5	Zero degree calorimeter . . . . .	39
3.2.6	Particle flow algorithm . . . . .	40
<b>4</b>	<b>Measuring luminosity</b>	<b>43</b>
4.1	Instantaneous luminosity . . . . .	43
4.2	Luminometers . . . . .	44
4.2.1	Pixel cluster counting . . . . .	44
4.2.2	Pixel luminosity telescope . . . . .	45
4.2.3	Hadronic forward calorimeter . . . . .	46
4.2.4	Fast Beam Conditions Monitor . . . . .	46
4.3	Van de Meer scanning calibration . . . . .	47
4.4	Corrections to VDM scans . . . . .	47
4.5	Systematic uncertainty . . . . .	49
4.6	Author's contributions . . . . .	49
<b>5</b>	<b>Trigger development and performance</b>	<b>54</b>
5.1	Triggering at CMS . . . . .	54
5.2	Author's contributions . . . . .	57
<b>6</b>	<b>Data analysis</b>	<b>60</b>
<b>7</b>	<b>Systematic uncertainties</b>	<b>78</b>
<b>8</b>	<b>Results and conclusions</b>	<b>81</b>



## List of Figures

1.1	Feynman diagram of coherent dijets in dipole framework [12]. . . . .	3
1.2	QCD coupling constant as a function of $Q^2$ [20]. . . . .	6
1.3	Collision cross section as a function of Bjorken- $x$ , with data compared to HERA-PDF calculations [26]. . . . .	8
1.4	Suppression factor of nucleus PDF as a function of Bjorken- $x$ . At different Bjorken- $x$ and $Q^2$ values various nuclear effects are seen: shadowing, anti-shadowing, EMC, and Femi motion. [31]. . . . .	9
1.5	Subnuclear tomography. This figure illustrates that at higher energies the substructure of the hadron can be resolved until researching the gluon saturation regime. [33]. . . . .	10
1.6	Pictorial time-line of the Universe, showing the various phase transitions, including the appearance of the QGP phase where quarks and gluons are present in a deconfined state [39]. . . . .	11
1.7	QCD phase diagram showing the temperature $T$ as a function of baryon chemical potential $\mu_B$ . Different phases such as the critical point, QGP, and hadron gas are seen [37]. . . . .	12
1.8	$J/\psi$ suppression as a function of transverse energy $E_T$ in Pb-Pb collisions at SPS. Data from different periods are shown and compared to theories that do not incorporate QGP [34]. . . . .	13
1.9	Heavy-ion overlap region, showing the elliptic flow produced [54]. . . . .	14
1.10	$v_2$ as a function of collision energy for various heavy ion experiments [34]. . . . .	14
1.11	Space-time diagram of a heavy-ion collision [55]. . . . .	15

2.1	(a.) electromagnetic field of stationary charge (b.) eletromagnetic field of boosted charge [62]. . . . .	18
2.2	$AuAu \rightarrow AuAu\rho^o$ , (a.) UPC exclusive $\rho^o$ diagram, (b.) with mutual nuclei excitation [74]. . . . .	20
2.3	UPC exclusive $\rho^o p_T$ , (a.) topology triggered (b.) minimum bias triggered [74]. . . . .	21
2.4	$\gamma + \text{proton} \rightarrow J/\psi + \text{proton}$ cross section, showing the ALICE and HERA data [84]. . . . .	21
2.5	(a) dimuon invariant mass spectrum, (b) dimuon $p_T$ spectrum for $J/\psi$ candidates. The data has been compared to STARLIGHT MC [81]. . . . .	22
2.6	Differential cross section versus rapidity for coherent $J/\psi$ photoproduction in ultra-peripheral PbPb collisions at $\sqrt{s_{NN}} = 2.76$ TeV. Data are compared to theories incorporating the impulse approximation and the leading twist approximation [81]. . . . .	22
2.7	Suppression factor of Pb PDF as a function of Bjorken- $x$ . Theoretical models are compared to ALICE and CMS data. . . . .	23
2.8	Feynman diagrams for coherent jet photoproduction in (a) direct photon in ep interactions, (b) resolved photon in ep interactions. [99]. . . . .	24
2.9	Ratio of H1 data cross section to NLO-QCD cross section [99]. . . . .	25
2.10	H1, diffractive $e + p$ products, kinematics [103]. . . . .	26
2.11	Interconnectedness of parton distributions [106]. . . . .	28
3.1	Cutout of CMS; radial cross section view [115]. . . . .	32
3.2	Pseudorapidity acceptance of tracker [117]. . . . .	33
3.3	ECAL components [118]. . . . .	35
3.4	Reconstructed data, ECAL energy resolution [120]. . . . .	36
3.5	L1 trigger, ECAL energy resolution, showing the results for calorimetry (calo) and particle flow (PF) approaches [120]. . . . .	36
3.6	HCAL energy resolution as a function of pseudorapidity [120]. . . . .	37
3.7	HCAL components; HB, HE, and HF [120]. . . . .	38

3.8	Pseudorapidity acceptance of muon detector [120]. . . . .	39
3.9	Performance of particle flow alorgithm compared to calorimeter readout [129]. . .	41
4.1	PLT triple coincidence. . . . .	45
4.2	PCC VdM Scans [130]. . . . .	48
4.3	CMS Run Registry. . . . .	51
4.4	CMS lumi during the 2015 PbPb run. . . . .	52
4.5	Total integrated luminosity for the various pp periods in 2010 until 2017. . . . .	53
5.1	Flow of information in L1 trigger [139]. . . . .	55
5.2	High multiplicity PbPb collision. . . . .	56
5.3	UPC Upsilon candidate. . . . .	56
6.1	29, 34. . . . .	60
6.2	39. . . . .	61
6.3	40. . . . .	62
6.4	41. . . . .	63
6.5	43, 44, 45. . . . .	64
6.6	46. . . . .	65
6.7	49. . . . .	66
6.8	52. . . . .	67
6.9	55, 56. . . . .	68
6.10	57. . . . .	69
6.11	mc gap comp. . . . .	70
6.12	mc 2D gap comp. . . . .	71
6.13	60, 61. . . . .	72
6.14	62. . . . .	73
6.15	66. . . . .	74
6.16	70. . . . .	75

6.17	109.	76
6.18	Individual Jet.	77
7.1	Jet Pt sys.	78
7.2	Vertex sys.	79
7.3	Correction factor.	80
A.1	RAPGAP process: boson-gluon fusion.	95
A.2	Left: Energy Distribution Before Fitting, Right: Energy Distribution After Fitting	96

## List of Tables

4.1	Systematic uncertainty during the 2015 pp run [130]. . . . .	49
4.2	Luminosity by CMS fill. . . . .	50
5.1	L1 Trigger Average Rates for Run 263757 . . . . .	58
5.2	HLT Average Rates for Run 263757 . . . . .	58
5.3	L1 Trigger Average Rates for Run 285530 . . . . .	58
5.4	HLT Average Rates for Run 285530 . . . . .	59

# Chapter 1

## Introduction

Microseconds after the big bang, the universe was filled with a hot, dense state of strongly interacting subnuclear particles [1]. There is evidence that this phase of matter, the quark gluon plasma (QGP), is recreated in the high energy densities reached by ultra-relativistic heavy-ion collisions [2]. Measurements at the Relativistic Heavy Ion Collider (RHIC) and the Large Hadron Collider (LHC) are consistent with the QGP having the sheer viscosity of a perfect fluid [3]. At present the field of ultra-relativistic heavy-ion collisions focuses on measuring the QGP properties in detail. In particular, initial state properties of the nucleus at high energies must be rigorously measured to distinguish between the effects of the QGP and of the inherent properties of the nucleus.

This thesis seeks to further knowledge of initial state phenomena in heavy-ion collisions by measuring the gluon distribution within the nucleus. We have studied coherent dijet photoproduction in ultra-peripheral collisions (UPC), as the distribution of the so-called "elliptic" gluons is encoded in the angular correlation of the dijets [4]. In UPCs all interactions between nuclei are from electromagnetic or electroweak processes, thus initial state physics are easily accessible [5]. Such photo-nuclear interactions are described via the equivalent photon approximation from the Weizacker-Williams formalism [6, 7], as discussed in Chapter 2.

Before discussing the physics of ultra-peripheral collisions and that of UPC dijets, we will give an overview of the standard model of high energy physics, followed by an introduction to relativistic heavy-ion collisions and how these are connected to photon-induced interactions.

## 1.1 The Standard Model

At the turn of the century, Ernst Rutherford probed the gold atom by bombarding a gold sheet with alpha-particles. The angular distribution of the scattered alpha-particles demonstrates that the mass of the atom is concentrated in a small volume, i.e, the atom is mostly empty space. Further experiments revealed that the atomic nuclei consisted of separate positively and neutrally charged particles: protons and neutrons.

Today, the Standard Model describes the fundamental particles of the universe in terms of fermions and bosons. Fermions are particles with half-integer spin, while bosons have integer-spin. Fermions must obey the Pauli Exclusion Principle: only one fermion at a time can occupy a given state. However, multiple bosons can simultaneously occupy a specific state [8]. Protons and neutrons, as subnuclear particles, contain large numbers of both fermions and bosons. Fermions and bosons have different statistical properties. Fermi-Dirac statistics describe the energy distribution of fermions. Likewise, the boson energy distribution is described by Bose-Einstein statistics [9].

Among the fermions are the leptons, neutrinos, and quarks. The leptons consist of the electron, muon, and tau, as well as their anti-particles. The leptons are believed to be fundamental: high energy experiments have yet to observe internal lepton-structure. Neutrinos are weakly interacting particles detected primarily through the precise measuring of missing transverse energy in the products of particle collisions. Quarks are the constituent particles of baryons, which contain three valence quarks, and mesons, which contain two valence quarks. In addition to the valence quarks are the sea quarks, which appear and disappear as quark-antiquark pairs within hadrons. The hadrons are particles made of quarks and gluons. Gluons are particles that mediate the strong nuclear force; likewise, photons mediate the electromagnetic force, and weak-gauge bosons mediate the weak nuclear force. A fourth boson, the graviton, is expected to transmit the gravitational force, but this particle has not been observed [10].

The behavior of fundamental particles is best described within the framework of quantum field theory (QFT). QFT defines a Lagrangian for fundamental particles. This Lagrangian then predicts the outcome of particle collisions. Different terms in the Lagrangian correspond to the various

interactions between particles. The Standard Model Lagrangian,  $\mathcal{L}_{StandardModel}$  can be broken down into three basic terms:

$$\mathcal{L}_{StandardModel} = \mathcal{L}_{QED} + \mathcal{L}_{QCD} + \mathcal{L}_{Higgs} + \dots, \quad (1.1)$$

where  $\mathcal{L}_{QED}$  is the QED Lagrangian,  $\mathcal{L}_{QCD}$  is the QCD Lagrangian, and  $\mathcal{L}_{Higgs}$  is the Higgs Lagrangian [10]. The most accessible approach to quantum field theory is through the use of Feynman diagrams. First, one imagines an interaction between particles. Then, one draws this process into a Feynman diagram, which is essentially a pictorial representation of exchanges between particles. The Lagrangian can be interpreted into Feynman rules. These rules describe how the Feynman diagram translates into a calculation for the quantum mechanical amplitude of the process. The quantum mechanical amplitude, in turn, is proportional to the cross section of the process. This is important because, since the cross section is invariant between experiments, one can use it to effectively test for invariant quantities in the Lagrangian [11].

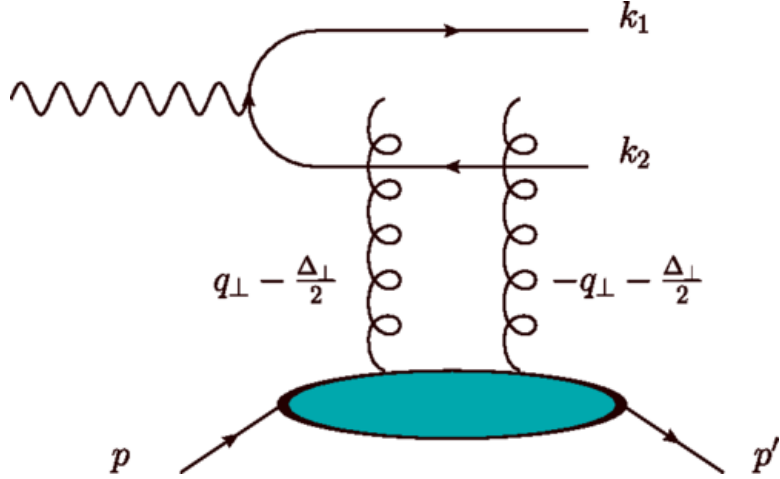


Figure 1.1: Feynman diagram of coherent dijet photoproduction in dipole framework [12].

Figure 1.1 is the Feynman diagram of coherent dijet photoproduction in an photon-proton interaction.  $k_1$  and  $k_2$  are the four vectors of the dijets.  $q_{\perp}$  is the average momentum of the dijets, and  $\Delta_{\perp}$  is the proton recoil momentum. This is the Feynman diagram of the physics analysis presented in this thesis and the physics motivation for this process is discussed in Chapter 2.

## 1.2 Quantum electrodynamics

Quantum electrodynamics (QED) is a theory of electromagnetic interactions in terms of relativistic quantum field theory. The QED Lagrangian is

$$\mathcal{L} = \bar{\psi}(i\gamma^\mu D_\mu - m)\psi - \frac{1}{4}F_{\mu\nu}F^{\mu\nu}, \quad (1.2)$$

where  $\psi$  is spin- $\frac{1}{2}$  field,  $\gamma^\mu$  are the Dirac matrices,  $D_\mu$  is the gauge covariant derivative,  $m$  is the electron mass, and  $F_{\mu\nu}$  is the electromagnetic field tensor [11].

QED addresses three specific processes: photon motion, electron motion, and the emission or absorption of a photon by an electron. First a Lagrangian is established based on Maxwell's laws and quantum mechanics. The photon constitutes a spin-1 solution to the differential equations derived from the QED Lagrangian. Likewise electrons are described, at non-relativistic scales, by the Schrödinger equation, and at relativistic scales by the Dirac equation. There are three processes allowed by QED: the translation of an electron, the translation of a photon, and the scattering of a photon off an electron [13].

The QED coupling constant  $\alpha_{em}$  is approximately 1/137 at perturbative scales [14]. In general, the cross section of a given process is proportional to the  $(\alpha_{em})^n$  where  $n$  is the number of vertices in the Feynman diagram. The more complex the Feynman diagram, the smaller its cross section. However, at small scales, i.e. non-perturbative momentum transfers  $Q^2$ , the coupling constant increases.  $\alpha_{QED}$  is defined as

$$\alpha_{QED}(Q^2) = \frac{\alpha_{em}}{(1 - \frac{\alpha_{em}}{3\pi})\ln(\frac{Q^2}{m^2})}, \quad (1.3)$$

where  $\alpha_{QED}(Q^2)$  is the QED coupling constant at high  $Q^2$ , and  $m$  is the electron mass [15]. High values of  $Q^2$  are non-perturbative because, at small scales and high momentum, the fluctuation of photons into electron-positron pairs begins to saturate. Particle and anti-particle pairs can pop into existence for a short time and then annihilate so long as quantum numbers are conserved.

### 1.3 Quantum chromodynamics

The parton model, first proposed by Richard Feynman, posits that hadrons in general, and nucleons in specific, are made of more fundamental constituent particles which may or may not be the quarks implied by the SU(3) symmetry. In addition to the quarks, the partons also include any field quanta associated with nuclear forces. These field quanta are named "gluons" [16].

The quarks are a family of fermions that compose the baryons and the mesons. Baryons consist of three quarks in a color neutral state, while mesons consist two quarks in a color neutral state. "Color" in this context refers to the six kinds of strongly-interacting charge available to quarks: red and anti-red, blue and anti-blue, and green and anti-green. Color charge has no relation to optical phenomena, but provides a useful analogy for the stable combinations of quarks. The net color-charge of a baryon or meson is colorless. By way of analogy, a red quark, green quark, and blue quark can together form a hadron, in the way that conventional red, green, and blue colors can together form the color white [17].

Gluons are the QCD analogues of the photons in QED. Gluons are spin-1 and massless, but unlike photons, which do not carry electromagnetic charge, gluons carry strongly-interacting charge [18]. The QCD Lagrangian, which encodes the interactions of gluons and quarks, is

$$\mathcal{L}_{QCD} = \bar{\psi}_i (i(\gamma^\mu D_\mu)_{ij} - m \delta_{ij}) \psi_j - \frac{1}{4} G_{\mu\nu}^a G_a^{\mu\nu}, \quad (1.4)$$

where  $m$  here represents the quark mass, the  $\delta_{ij}$  is the delta function and  $G_{\mu\nu}^a$  is gluon field tensor,

$$G_{\mu\nu}^a = \partial_\mu \mathcal{A}_\nu^a - \partial_\nu \mathcal{A}_\mu^a + g f^{abc} \mathcal{A}_\mu^b \mathcal{A}_\nu^c. \quad (1.5)$$

The SU(3) symmetry group of the quarks is indexed as  $i, j, \dots$ ; the adjoint SU(3) group, for the gluons, is indexed  $a, b, c$ .  $\mathcal{A}_\nu^a$  is the gluon field,  $f^{abc}$  are the SU(3) structure constants, and  $g$  is the strong coupling [19].

Unlike QED, the QCD coupling increases with distance [20]. Figure 1.2 shows the running of the QCD coupling with  $Q^2$ :

$$\alpha_{QCD}(Q^2) = \frac{4\pi}{(11 - \frac{2}{3}n_f)\ln(\frac{Q^2}{\Lambda_{QCD}^2})}, \quad (1.6)$$

where  $n_f$  is the number of quark flavors,  $Q^2$  is the momentum transfer, and  $\Lambda_{QCD}^2$  is the mass

scale [21]. The running coupling has the practical consequence of the strong-interactions being stronger in high momentum transfer collisions. The direct results of the running QCD coupling include the dual phenomena of asymptotic freedom and color confinement. At large distances, string tension describes the binding force of the quarks. At short distances, however, Coulomb-like interactions dominate [22]. The QCD coupling constant can be measured via the cross-section of inelastic proton-proton collisions, and also the cross section of electron-positrons into triple jets [23].

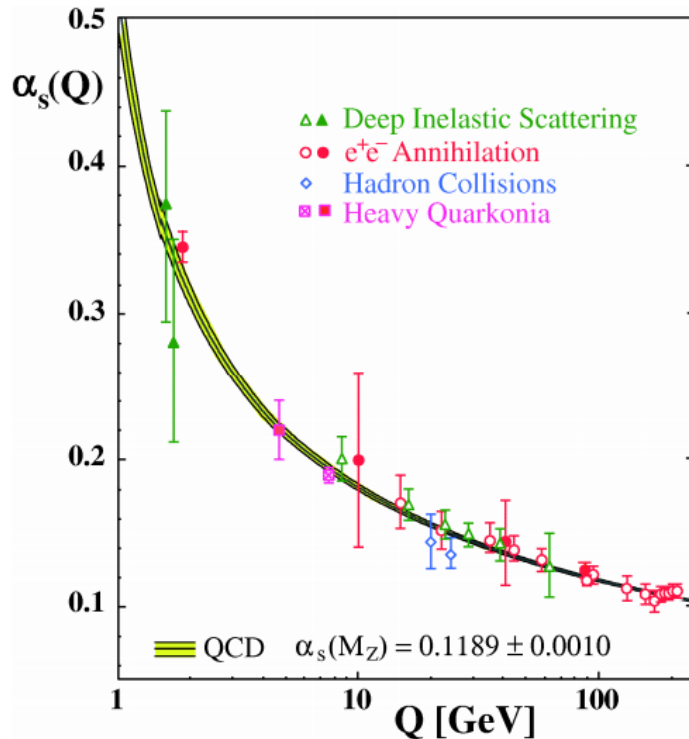


Figure 1.2: QCD coupling constant as a function of  $Q^2$  [20].

The existence of jets is a direct result of QCD confinement. In hadron collisions, it is possible for the hadron's constituent partons to fragment away. However, QCD confinement demands that only colorless objects can independently exist. Therefore, as the fragment partons separate, they manifest new partons around themselves and screen the color charge. The formation of colorless composites, out of colored partons, is called "hadronization". The process of hadronization continues until the kinetic energy of all the fragmented partons drops below the potential energy the

binding strong force. The result is a narrow cone of hadrons fanning out from a common source: a "jet". Analyzing a jet can elucidate the properties of its mother parton [24].

## 1.4 Deep inelastic scattering

Scattering experiments are the basic tool for exploring the nucleus. In particular, DIS commonly refers to the scattering of a lepton off hadrons. For example, experiments at HERA focused on electron-proton collisions. In these collisions, the electron was used as a source of photons and neutrinos. When these particles scatter off the proton, the dependence of the collision cross section, on momentum transfer and scattering angle of the source electron, reflects the structure of the proton. The momentum transferred,  $Q^2$ , is an important quantity for characterizing DIS measurements. In addition to  $Q^2$ , Bjorken- $x$  is necessary to describe the nuclear phase space. Bjorken- $x$  represents the momentum fraction of partons. In lepton-proton scattering it was observed that at high momentum transfers the structure functions of the proton were functions of  $Q^2/v$ , where  $Q^2$  is the squared four-momentum of the virtual photon emitted by the electron, and  $v$  is the energy lost by the electron in the collision [22]. DIS experiments provided the first evidence of two phenomena: the parton model (discussed in Section 1.3) and Bjorken-scaling.

"Scaling" is an interpretation of the data from DIS. First proposed by James Bjorken, scaling is reflected in the incoherence of photon-proton interactions at photon energies above  $1 \text{ GeV}/c$  [25]. Predictions from perturbative QCD are in good agreement with DIS data from HERA, as seen in Figure 1.3 [26]. In this graph the Bjorken- $x$  momentum fraction is designated  $x$ , and  $\sigma_r$  represents the  $F_2$  structure function, and  $Q^2$  is the transferred momentum from the electron to the proton. The order of magnitude of  $\sigma_r$  set by the Bjorken- $x$ .

At the small scales probed by high energy photons, the decreasing QCD coupling causes quarks and gluons to interact weakly. This phenomena is called "asymptotic freedom". Because gluons themselves carry color charge, the gluons about a quark tend to have an anti-screening behavior: the gluon color adds to the quark color, increasing the net color charge of the area. At smaller distances to a quark, then, there are fewer and fewer gluons augmenting the color interaction.

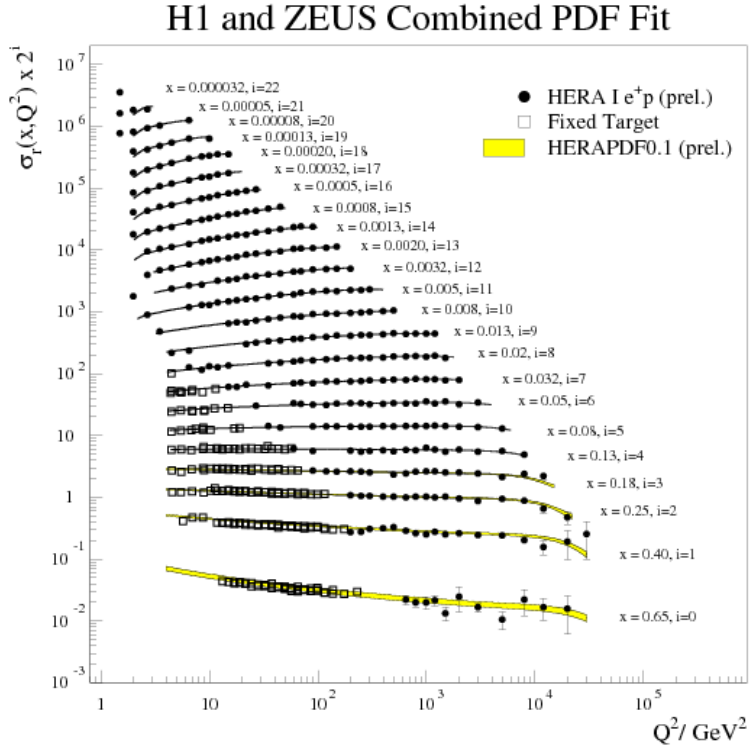


Figure 1.3: Collision cross section as a function of Bjorken- $x$ , with data compared to HERA-PDF calculations [26].

As discussed in Chapter 2, in UPCs at RHIC and LHC it is possible to study DIS-like processes. In particular, in the study of coherent dijets in UPCs at the LHC is that it is possible to access both the Bjorken- $x$  and  $Q^2$  dependence.

## 1.5 PDFs

QCD describes the interaction between quarks and gluons, but within a nucleon the calculations are too complicated to solve for the behavior of each individual parton. Theorists employ the factorisation theorem to use data from DIS experiments to make predictions, as shown in Figure 1.3. The factorisation theorem is discussed in greater detail later in Section 2.3. Parton distribution functions (PDFs) are a method of encoding data, mainly from DIS experiments, in the form of probability density. PDFs give the probability of finding a species of parton with given momentum fraction,  $x$ , and a given squared energy scale,  $Q^2$  [27–30].

In electron-proton deep inelastic scattering, the electron interacts with the proton electromagnetically by the emission of a virtual photon. This virtual photon has a four momentum  $q$  and a virtuality  $Q^2 = -q^2$ . When virtuality is low, the virtual photon is approximately "real"; these quasi-photons are discussed in greater detail in Chapter 2. The virtual photon, originating from the electron, interacts with a parton and changes its initial momentum fraction,  $x$ . The  $Q^2$  of the probing virtual photon and Bjorken-x of interacting parton are determined from the collision products. The data can be used to fill out a probability density,  $F_i(x, Q^2)$ , of finding a parton species  $i$  at a given momentum fraction  $x$  with a probe of virtuality  $Q^2$ . The suppression factor  $R$  is the ratio of the nucleus PDF to the free proton one, without nuclear effects. Figure 1.4 shows the suppression factor of the nucleus PDF as a function of Bjorken- $x$  [31].

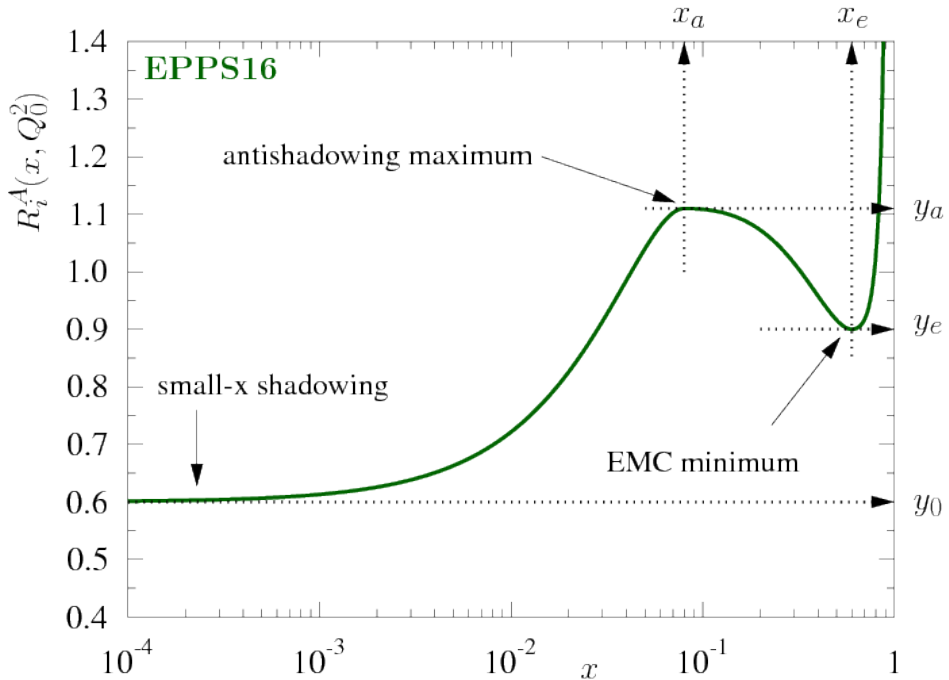


Figure 1.4: Suppression factor of nucleus PDF as a function of Bjorken- $x$ . At different Bjorken- $x$  and  $Q^2$  values various nuclear effects are seen: shadowing, anti-shadowing, EMC, and Femi motion. [31].

One of the most interesting HERA results is that the parton density rapidly increases as the momentum fraction decreases. Conservation of momentum demands that the splintering of partons must eventually cease. The specific saturation point, where recombination begins dominates, is a

characteristic of high energy gluons within a hadron. The search for gluon saturation effects in the proton and the nucleus is one of the key lines of research in high energy heavy-ion collisions today. The Color Glass Condensate (CGC) model is one approach to describe gluon saturation [32]. Figure 1.5 shows an illustration of how the nucleus appears at varying momentum fractions [33]. In addition, PDFs model the longitudinal momentum distribution of the partons. The study of both proton and nuclear PDFs is essential for understanding final state effects produced in high energy nucleus-nucleus collisions where the Quark Gluon Plasma can be formed. With the advent of more precise data in nuclear collisions, the PDF analyses are now supplemented by transverse momentum distributions (TMDs) and generalized parton distributions (GPDs). In addition to transverse momentum, GPDs describe the transverse spatial distribution. TMDs and GPDs are derived from the final state particles of a collision.

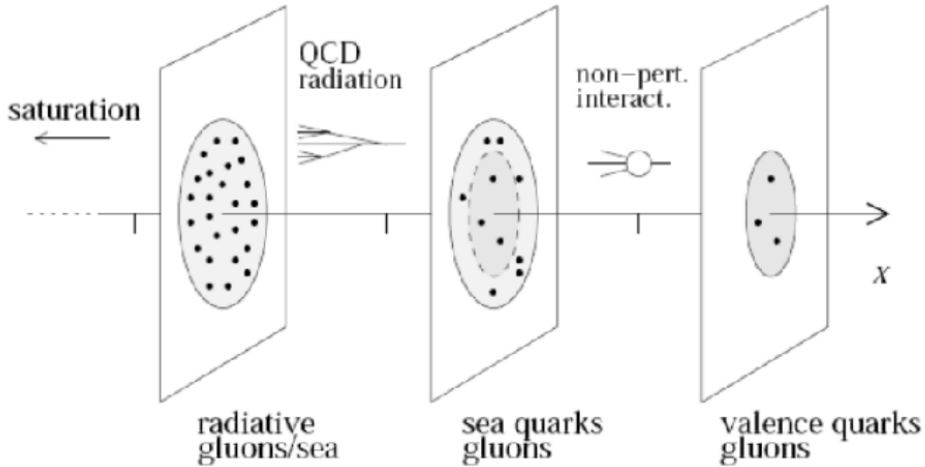


Figure 1.5: Subnuclear tomography. This figure illustrates that at higher energies the substructure of the hadron can be resolved until researching the gluon saturation regime. [33].

## 1.6 Quark gluon plasma

From 1980's to 2000's, the Super Proton Synchrotron (SPS) and the Relativistic Heavy Ion Collider (RHIC) performed heavy ion experiments to study the possibility of deconfined plasma in a high parton density medium [34–36]. These experiments confirmed the developing model of the QCD

phase space; see Figure 1.7 [37]. Essentially, quark matter organizes itself differently depending on temperature and baryon density. At low energies, quark matter exists in bound states: the hadrons. However, in the high energy limit, quarks and gluons take the form of a strongly interacting plasma: QGP. The QGP represents the extreme case of asymptotic freedom; the QCD coupling constant becomes small enough that quarks and gluons no longer behave as bound states. There are two ways of achieving the high energies necessary to form QGP. High baryon densities cause the quarks of separate hadrons to interact at small distances where asymptotic freedom takes effect. It is not currently possible to achieve these densities in laboratory experiments, though this state is thought to occur in neutron stars. By contrast, particle colliders like the LHC increase the energy density by colliding heavy-ions at ultra-relativistic velocities. The high temperature environment produces QGP. The early universe, mere milliseconds after the Big Bang, is thought to have existed as QGP [38].

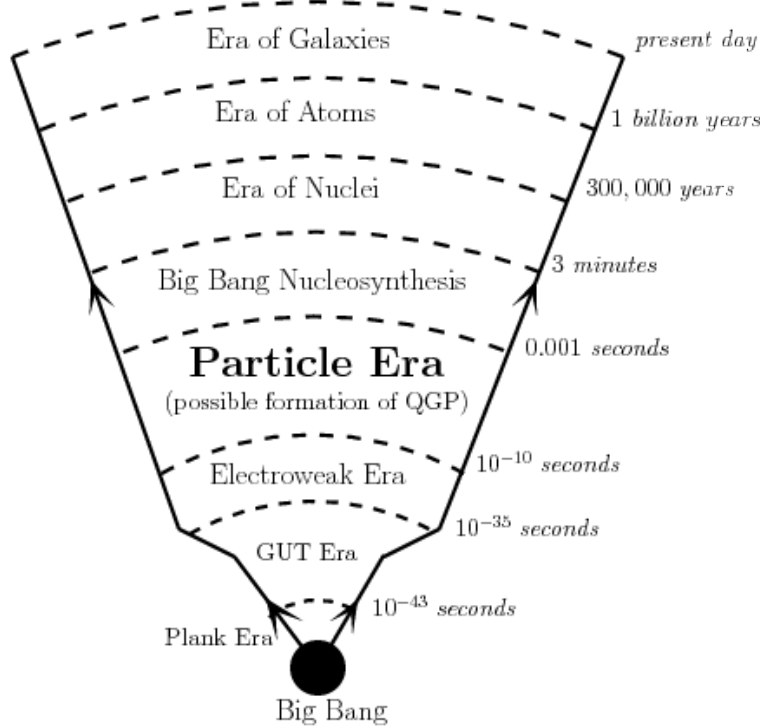


Figure 1.6: Pictorial time-line of the Universe, showing the various phase transitions, including the appearance of the QGP phase where quarks and gluons are present in a deconfined state [39].

Figure 1.6 is a simplified cosmological timeline. In the first hundred or so microseconds after

the Big Bang, the universe was small, dense, and highly energetic [39]. The energy density of the early universe would have been in excess of  $1 \text{ GeV}/(fm)^3$ . Note that  $1 \text{ GeV}/(fm)^3$  is the energy density at which QGP is thought to form. The universe cools and hadrons form out of the quarks and gluons. The protons and neutrons condense into nuclei. The positively charged nuclei gather negatively charged electrons, forming the atoms that in cosmic time become stars [40].

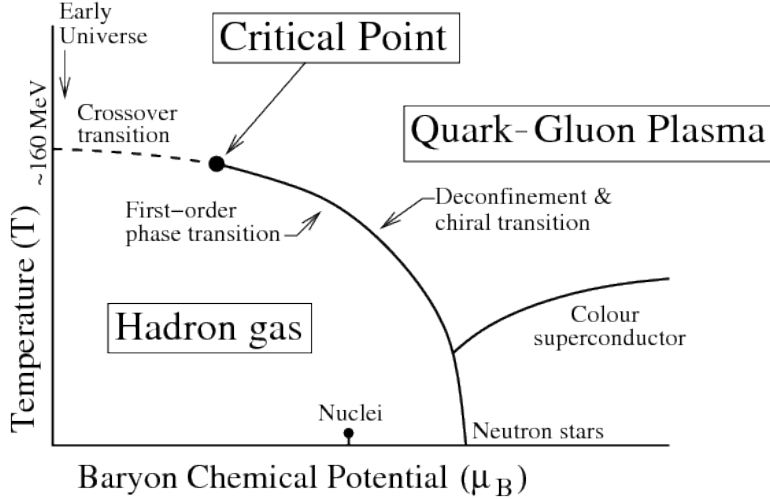


Figure 1.7: QCD phase diagram showing the temperature  $T$  as a function of baryon chemical potential  $\mu_B$ . Different phases such as the critical point, QGP, and hadron gas are seen [37].

There are a number of experimental signatures of QGP formation. Thermal physics understands phase transitions as occurring at specific temperatures and densities. At the boundary between two phases, one can define a critical point at which there is a discontinuous change in the behavior of observables. For the SPS heavy-ion programs the main observables were charm suppression and strangeness enhancement, while for the RHIC heavy-ion experiments the studies focused on elliptic flow, and jet quenching [41–43].

Figure 1.8 shows the suppression of  $J/\psi$  with respect to Drell-Yan scattering in Pb-Pb collisions at SPS [34]. The QGP is thought to suppress the production of  $J\psi$  mesons in heavy-ion collisions.

At RHIC, it was demonstrated that heavy-ion collisions can produce a state of hadronic matter, often referred to as "the medium", that exhibits elliptic flow. The predicted viscosity of QGP would cause elliptic flow in the overlap region of heavy-ion collisions [44]. The angular corre-

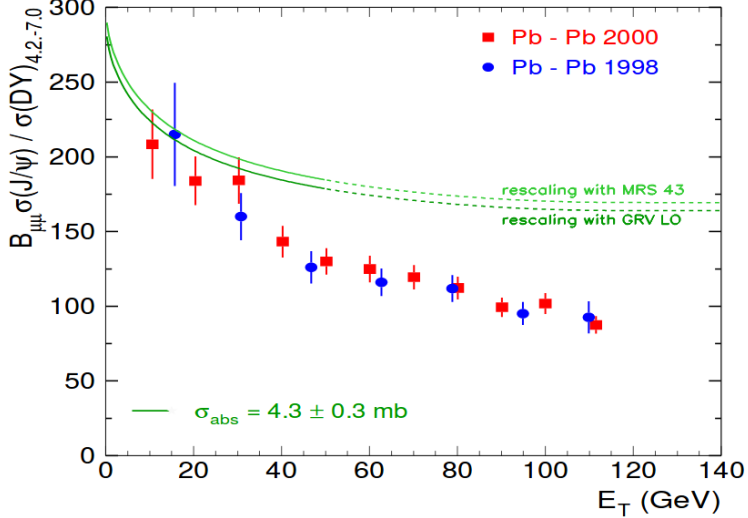


Figure 1.8:  $J/\psi$  suppression as a function of transverse energy  $E_T$  in Pb-Pb collisions at SPS. Data from different periods are shown and compared to theories that do not incorporate QGP [34].

lations of the final state particles, produced by heavy-ion collisions, were analyzed and shown to be consistent with the medium flowing as a nearly ideal fluid [45]. "Ideal fluid" refers to how the high temperature nuclear medium can be modelled by hydrodynamic equations in which the shear viscosity is extremely low [46].

As the QGP is a perfect fluid, the initial state properties of the heavy-ion will propagate through the collision and have a significant effect on the final state particles. The angular distribution of final state particles can be modelled using Fourier series,

$$1 + \sum_{n=1}^{\infty} 2v_n \cos[n(\phi - \Psi)], \quad (1.7)$$

where  $n$  is the order of the Fourier expansion,  $v_n$  is the Fourier coefficient,  $\phi$  is the azimuthal angle, and  $\Psi$  is the event-plane angle. The 2nd order term,  $v_2$ , is referred to as "elliptic flow" and is predicted to quantify the pressure gradient of the overlap-region in the heavy-ion collision. Figure 1.9 is an illustration of the overlap region of a heavy-ion collision. Because the pressure gradient is higher for the short axis than for the long axis, the nuclear medium in the overlap region will flow outward along the short axis, and this is reflected in the alignment of the tracks in the direction of the flow [47–53].

A highly viscous medium will resist deformation such that the shape of the overlap region,

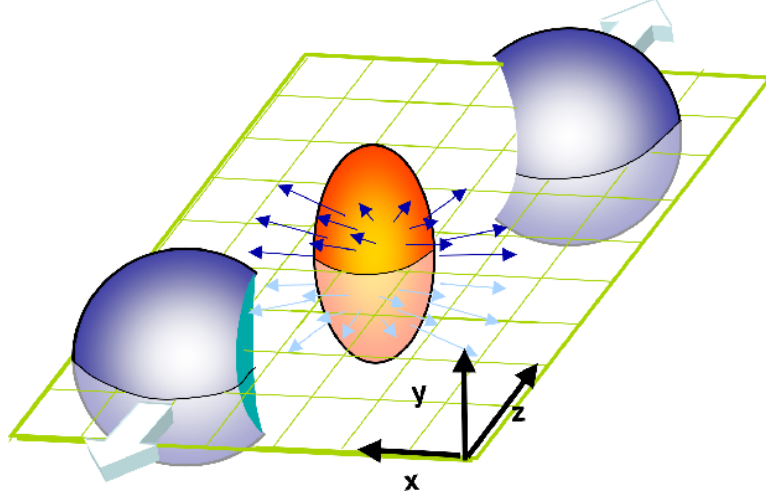


Figure 1.9: Heavy-ion overlap region, showing the elliptic flow produced [54].

i.e. its ellipticity, will not necessarily carry over to the final-state tracks. However, because the QGP medium is a nearly ideal liquid, the elliptic correlation of the final-state should arise from that of the initial-state. The RHIC result emphasizes the great importance of a precisely understood heavy-ion initial state. Figure 1.10 compares the  $v_2$  elliptic flow results from various heavy-ion experiments [34].

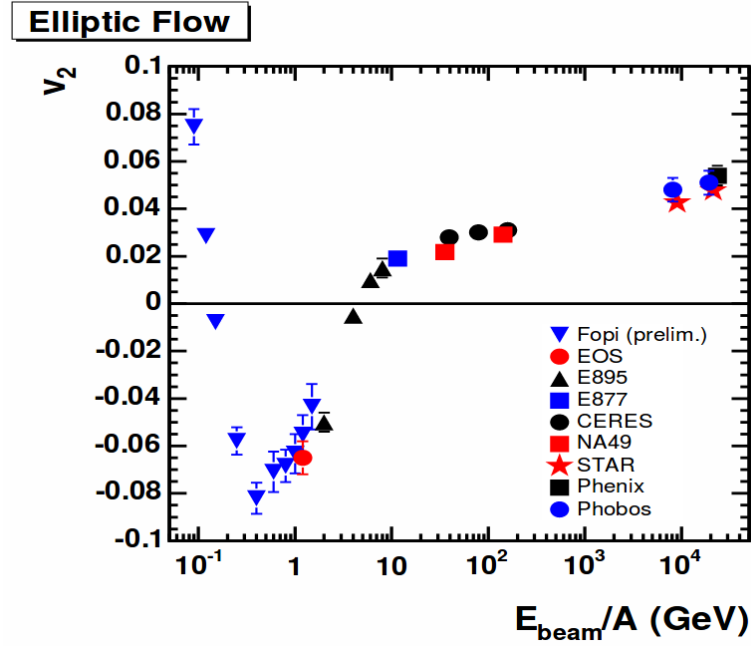


Figure 1.10:  $v_2$  as a function of collision energy for various heavy ion experiments [34].

The phase transitions from a hot, dense medium to stable hadrons are seen in heavy-ion collisions, as illustrated by Figure 1.11 [55]. The y-axis represents time, and the x-axis represents the longitudinal separation of the ions. Notice that after the ions cross, there is a "cascade" during which the partons take on thermal energy until reaching a critical temperature for QGP formation. The hadron gas passes through two temperature "freeze-out". When particles stop forming the chemical freeze-out temperature. These particles stop exchanging kinetic energy after cooling beyond the "kinetic freeze-out" [56].

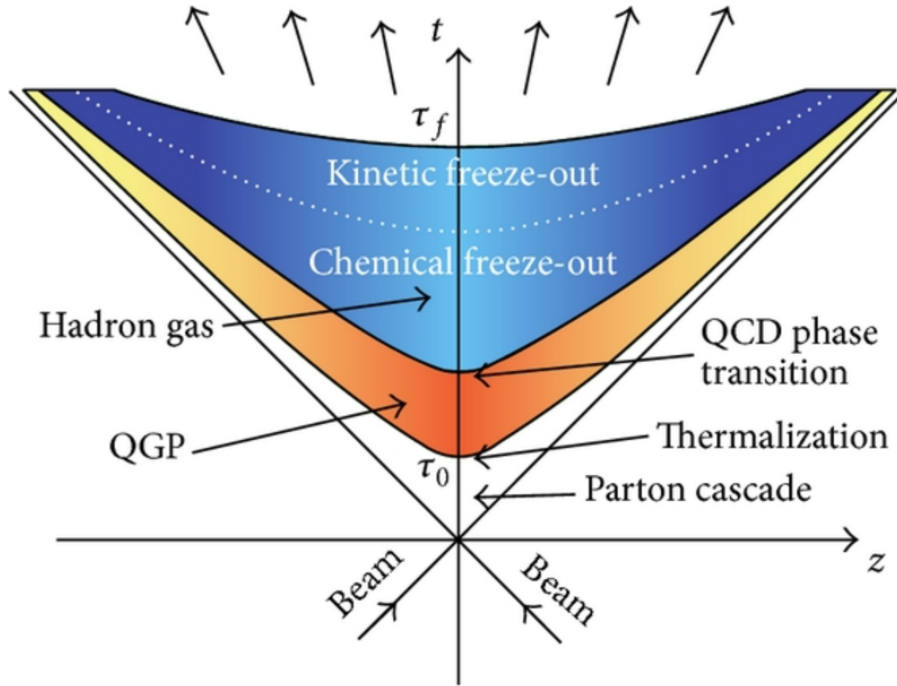


Figure 1.11: Space-time diagram of a heavy-ion collision [55].

Lastly, hadronic jets would interact strongly with the QGP; therefore, dijets will have significant energy imbalance depending on the multiple interactions of the components jet with the QGP. All of these cases require a good understanding the heavy-ion initial state as a basis for comparison [57].

The Large Hadron Collider (LHC) stands at the forefront of high energy nuclear physics research. The LHC is capable of reaching heavy-ion collision energies of up to 7 TeV per nucleon-nucleon, which is sufficient energy for a QGP to be formed and to last long enough to measure its

properties [58–60].

# Chapter 2

## Ultra-peripheral collisions and photoproduction

In this chapter, we will review recent LHC results on ultra-peripheral collisions (UPCs). First we will discuss the unique features of UPCs, and how they are selected. We then present the results from ALICE and CMS on vector meson photoproduction as an example of how UPCs can probe the nuclear gluon distribution. The final section explains dijet photoproduction in UPCs, and how the factorisation theorem informs the interpretation of coherent dijet correlation. Finally, we present the physics motivation to study the angular correlation of UPC dijet, which is the analysis presented in this thesis.

### 2.1 Ultra-peripheral heavy-ion collisions

Ultra-peripheral collisions occur at impact parameters greater than the sum of the heavy-ion radii. In these collisions, hadronic interactions are strongly suppressed while photonuclear activity is enhanced proportional to the square of the nuclear charge [5]. The electromagnetic field of an incoming heavy-ion, from the perspective of a target, is equivalent to a flux of virtual photons; Figure 2.1 illustrates the Lorentz contraction of the field of a boosted charge [61, 62].

UPC models typically address two elements: the photon flux,  $N_{\gamma/Pb}$ , and the photoproduction cross-section,  $\sigma_{\gamma Pb}$ . These quantities are related to the UPC cross-section,  $\sigma_{PbPb}$ , in the following equation

$$\frac{d\sigma_{PbPb}}{dy} = N_{\gamma/Pb}(y, M)\sigma_{\gamma Pb}(y) + N_{\gamma/Pb}(-y, M)\sigma_{\gamma Pb}(-y), \quad (2.1)$$

where there are two terms to reflect that either heavy-ion can be a source of photons [63].

The Weizsäcker-Williams appoximation (WWA) calculates the density of photons, about the

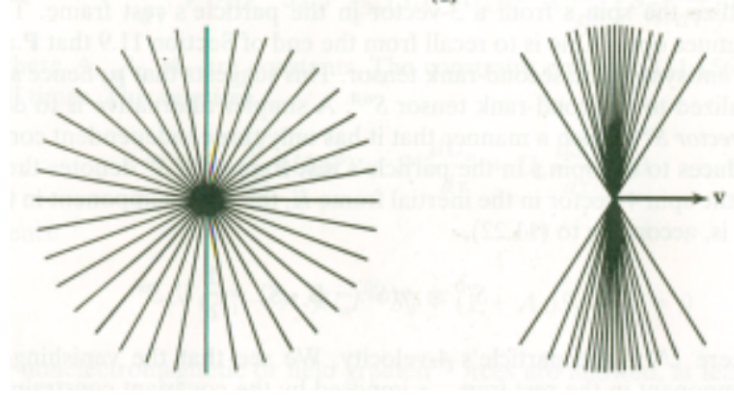


Figure 2.1: (a.) electromagnetic field of stationary charge (b.) electromagnetic field of boosted charge [62].

nucleus, as a function of energy. WWA is a semi-classical formulation. Maxwell's equations are solved for a stationary point charge boosted to an ultra-relativistic velocity. In the target's frame, the Fourier transform of the source field is taken. The Fourier frequency modes are interpreted through the quantum mechanical equation of photon energy. The photon flux as function of energy is given by

$$N(\omega, b) = \frac{\alpha}{\hbar\omega} \left( \frac{Z}{b\beta\pi} \right)^2 \left( \frac{\omega b}{\gamma v} \right) K_1^2 \left( \frac{\omega b}{\gamma v} \right), \quad (2.2)$$

where  $\alpha$  is the QED coupling constant,  $\omega$  is the photon energy,  $Z$  is the atomic number of the nuclei,  $b$  is the impact parameter,  $\beta$  is the ratio of the nuclei speed to the speed of light,  $\gamma$  is the Lorentz boost of the nuclei,  $K_1^2$  is a Bessel function, and  $v$  is the photon frequency [62].

The photon flux can be written as a function of the photon wavelength:

$$n(k) = \frac{2\alpha Z^2}{\pi} \left[ \xi K_0(\xi) - \frac{\xi^2}{Z} (K_1^2(\xi) - K_0^2(\xi)) \right] \quad (2.3)$$

For a given final state  $X$ , the collision cross section is given as

$$\sigma_X = \int d\omega \frac{n(\omega)}{\omega} \sigma_X^\gamma(\omega), \quad (2.4)$$

where  $n(\omega)$  is the number of photons emitted at an energy  $\omega$ , and  $\sigma_X^\gamma(\omega)$  is the photonuclear cross-section of the photon-nucleon interaction. The Weizacker-Williams approximation provides  $n(\omega)$ . The integral reflects how a state  $X$  can result from the interaction of a quasi-real photon of varying energy [64]. At low momentum transfer, photons interact electromagnetically, i.e. directly, with partons [65]. High energy, "resolved" photons possess a hadronic structure; instead of directly

interacting with the nuclei, these photons fluctuate into mediating quark-antiquark pairs.

UPCs can generate a wide variety of particles both from photon-proton and photon-hadron interactions.. In the next section we will discuss current results on vector meson photoproduction.

## 2.2 VM photoproduction

The vector mesons are a subset of the mesons that have spin-1 and negative parity. There are three vector mesons that have recently been studied in UPSCS: the  $\rho^0$ , the  $J/\psi$ , and the  $\Upsilon(1S)$ . The  $\rho^0$  is an antisymmetric superposition of up and down quark-antiquark pairs,  $(1/\sqrt{2})(u\bar{u} - b\bar{b})$ . The  $J/\psi$  consists of a charm quark and a charm antiquark. The  $\Upsilon(1S)$  consists of a bottom quark and a bottom antiquark.  $J/\psi$  and its excited states are referred to as charmonia; likewise,  $\Upsilon(1S)$  and its excited states are referred to as bottomonia.

The Bjorken- $x$  probed by a specific UPC vector meson is set by the mass  $M_{VM}$ , the rapidity  $y$ , and collision energy  $\sqrt{s}$ , such that

$$x = \frac{M_{J/\psi}}{\sqrt{s}} e^{\pm y}. \quad (2.5)$$

The vector meson mass also sets the hard scale,  $Q^2$ , of the photoproduction. For example, for the  $J/\psi$

$$Q^2 = \frac{M_{VM}}{4}. \quad (2.6)$$

The virtual photons present in UPC can fluctuate into a quark-antiquark pair which can take the form of a low mass meson [66–68]. This meson then interacts with the target nuclei via colorless gluon exchange, emitting a vector meson [69–72]. If the virtual photon interacts coherently with the target nucleus, this is reflected in the transverse momentum of the vector meson [73]. The vector meson decays into a dilepton pair that can be detected by the experiment.

One of the first observations of vector meson photoproduction in UPC was that of exclusive coherent  $\rho^0$  production at STAR. For this process the source nuclei emits a virtual photon that fluctuates into a  $\rho^0$  meson that scatters elastically off the target nuclei. The  $\rho^0$  decays into a pair of oppositely charged pions. These pions leave two back-to-back tracks in the STAR tracker. The

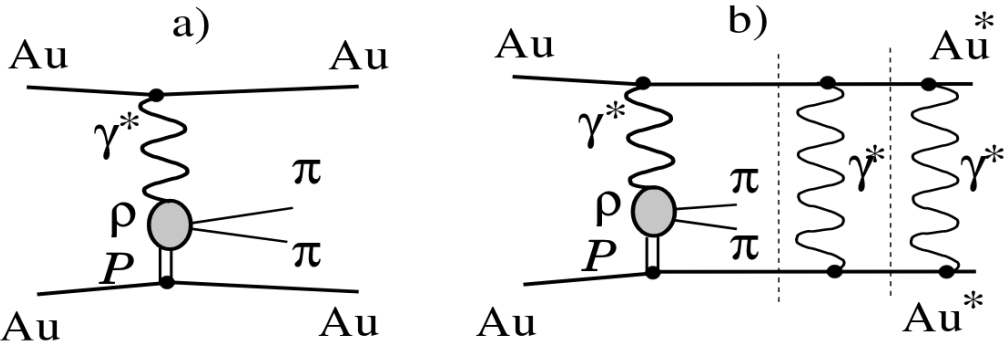


Figure 2.2:  $AuAu \rightarrow AuAu\rho^0$ , (a.) UPC exclusive  $\rho^0$  diagram, (b.) with mutual nuclei excitation [74].

Feynman diagrams for the process are seen in Figure 2.2. In exclusive production there are only two tracks in the tracker, with the rest of the detector being empty. In mutual nuclei excitation, the further exchange of virtual photons excite both nuclei and produce tracks in addition to those of the dipion system. The exclusive events were selected by STAR using a low-multiplicity trigger, while the mutual excitation events were selected using a minimum bias trigger with the additional requirement of neutron emission detected in both ZDCs [74].

One of the key signatures of coherent  $\rho^0$ , and UPC coherent mesons in general is their low  $p_T$ . If the virtual photon has energy of the order of  $1/2R_A$ , where  $R_A$  is the radius of the nuclei, the photon couples with the whole nucleus. The low momentum corresponds to large wavelength of the photon with respect to the nuclear radius [75–78]. The  $p_T$  spectrum of the  $\rho^0$  detected by the topology and minimum-bias triggers are shown in Figure 2.3, where the low  $p_T$   $\rho^0$  candidates are consistent with coherent photoproduction for the two different triggers. STARLIGHT is a Monte Carlo generator designed to model vector meson photoproduction in UPC [79].

More recently, ultra-peripheral coherent  $J/\psi$  photoproduction was studied by the ALICE and CMS collaborations using the 2011 Pb-Pb data [80]. Figure A.2 shows the dimuon invariant mass and  $p_T$  from the decay of coherent  $J/\psi$  [81]. Before discussing the  $J/\psi$  data in UPC PbPb, it is important to notice that the cross section of coherent  $J/\psi$  photoproduction, for  $\gamma + p \rightarrow J/\psi + p$ , has a power-law dependence on the photon-proton center-of-mass energy, as seen in Figure 2.4 [82]. Such data can be sensitive to the gluon distribution in the proton as a function of Bjorken-

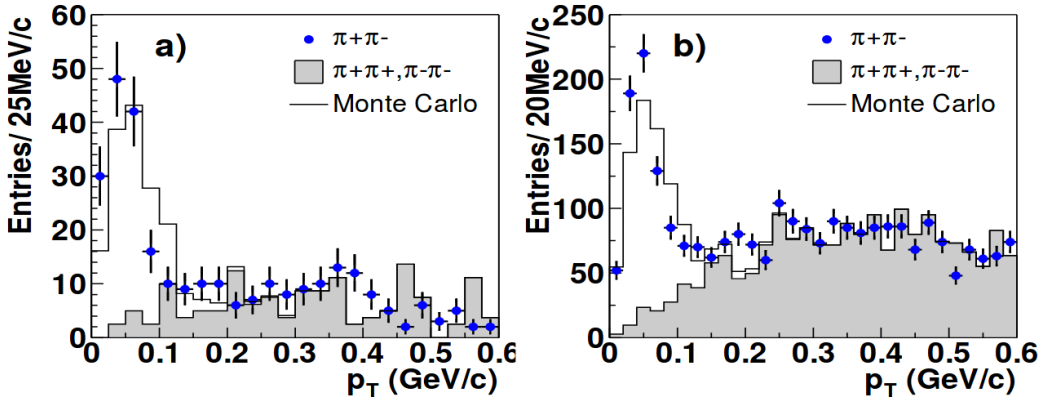


Figure 2.3: UPC exclusive  $\rho^0$   $p_T$ , (a.) topology triggered (b.) minimum bias triggered [74].

$x$  [83].

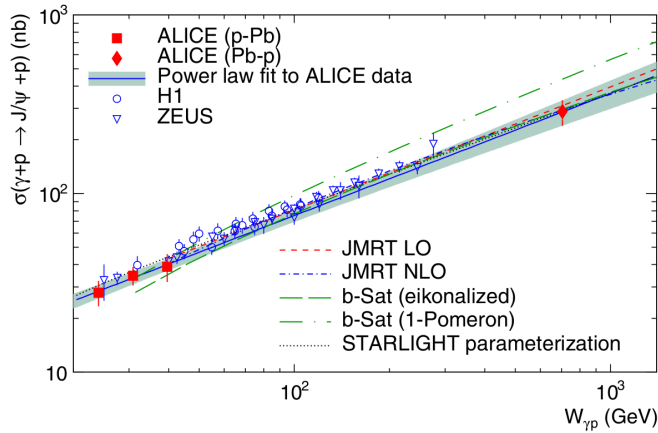


Figure 2.4:  $\gamma$ +proton $\rightarrow J/\psi$ +proton cross section, showing the ALICE and HERA data [84].

In the nucleus-nucleus collision, UPC  $J/\psi$  photoproduction cross section can be calculated using a Glauber model of the heavy-ion [85]. The impulse approximation depicts the nucleus as a sum of protons and neutrons by scaling up the photon-nuclear cross section derived from electron-proton collisions at HERA and at the LHC [86].

Studies of UPC  $J/\psi$  at ALICE and CMS show that the measured cross section is consistent with models of the nucleus that include moderately strong gluon shadowing, in particular EPS09 [87, 88]. Fig 2.6 compares the cross section measured by ALICE and CMS against theoretical models. In the data there is a clear difference from the impulse approximation prediction. The cross sections indicate that, at the energy scale of the  $J/\psi$  mass, the nuclear gluon density is suppressed

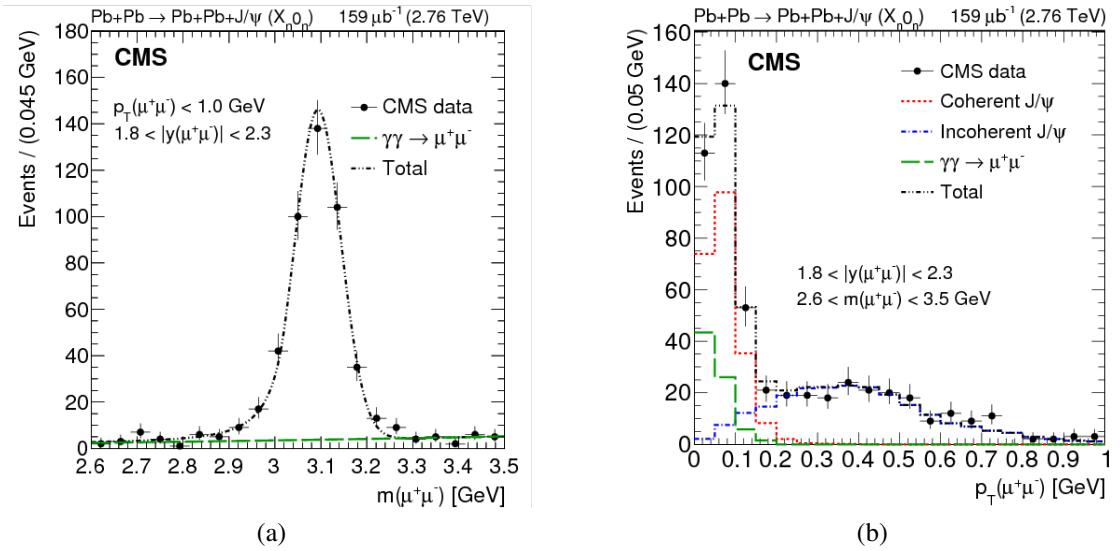


Figure 2.5: (a) dimuon invariant mass spectrum, (b) dimuon  $p_T$  spectrum for  $J/\psi$  candidates. The data has been compared to STARLIGHT MC [81].

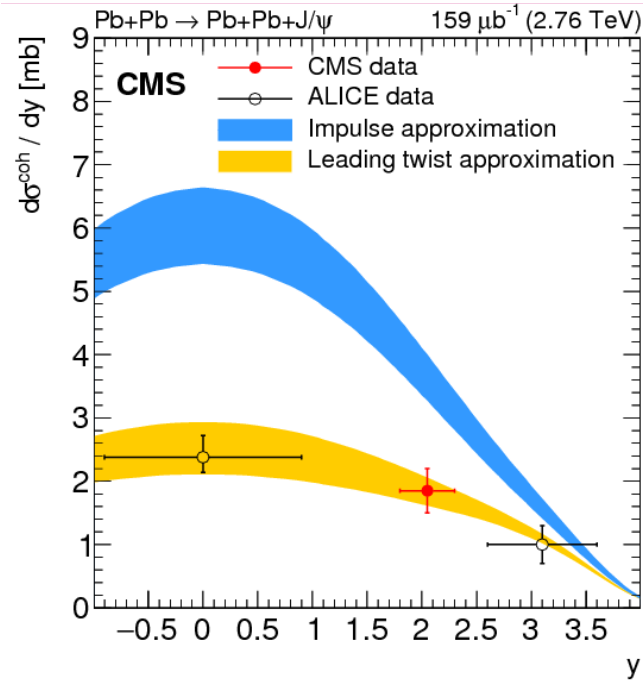


Figure 2.6: Differential cross section versus rapidity for coherent  $J/\psi$  photoproduction in ultra-peripheral PbPb collisions at  $\sqrt{s_{NN}} = 2.76$  TeV. Data are compared to theories incorporating the impulse approximation and the leading twist approximation [81].

with respect to that of the proton [89]. Further studies can be done using UPC  $\Upsilon$ ; although they are less sensitive to nuclear shadowing due to its higher  $Q^2$  values [90, 91]. The ALICE and CMS

data have been used to calculate the nuclear suppression factor, which is equivalent to the nuclear PDF calculation as a function of Bjorken- $x$  discussed in Section 1.5. The LHC data provides evidence for nuclear gluon shadowing at low  $Q^2$  and low Bjorken- $x$ . Figure 2.7 shows ratio of the Pb PDF to the proton PDF, as a function of Bjorken- $x$ , with data from ALICE and CMS compared to theoretical models of nuclear shadowing. This is the first experimental evidence that the Pb nucleus presents shadowing effects at high energies.

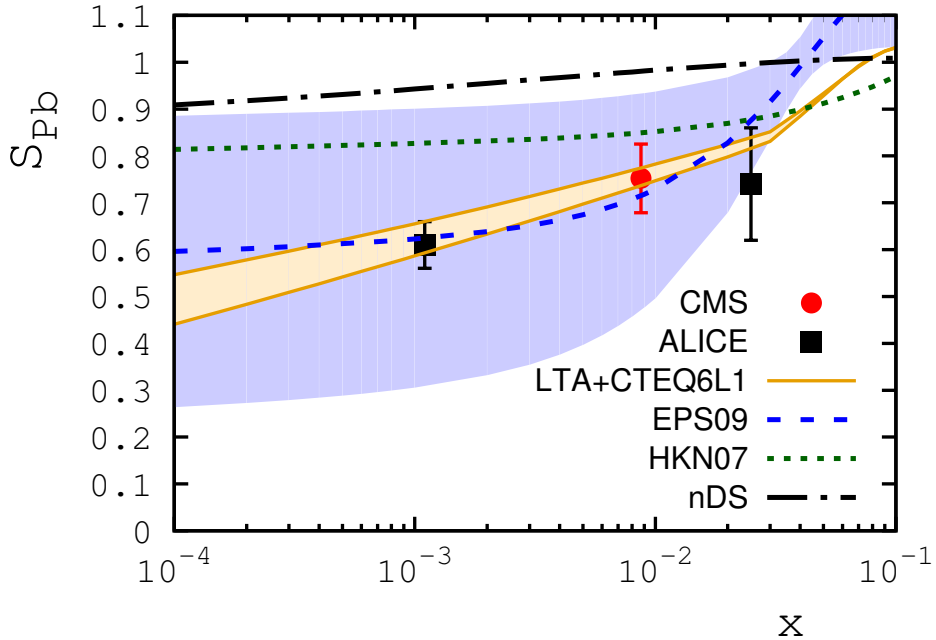


Figure 2.7: Suppression factor of Pb PDF as a function of Bjorken- $x$ . Theoretical models are compared to ALICE and CMS data.

Forward neutron tagging was used to separate the coherently and incoherently produced  $J/\psi$  [92–98].

## 2.3 Dijet photoproduction

In electron-hadron collisions, diffractive photoproduction is characterized by the presence of a large rapidity gap in the final state and an intact nucleus [100–102]. The Feynman diagram of electroproduction in lepton-hadron collisions is similar to that of photoproduction in ultraperipheral collisions, as seen in Figure 2.8 [99]. The large rapidity gap here is due to the leading proton [103].

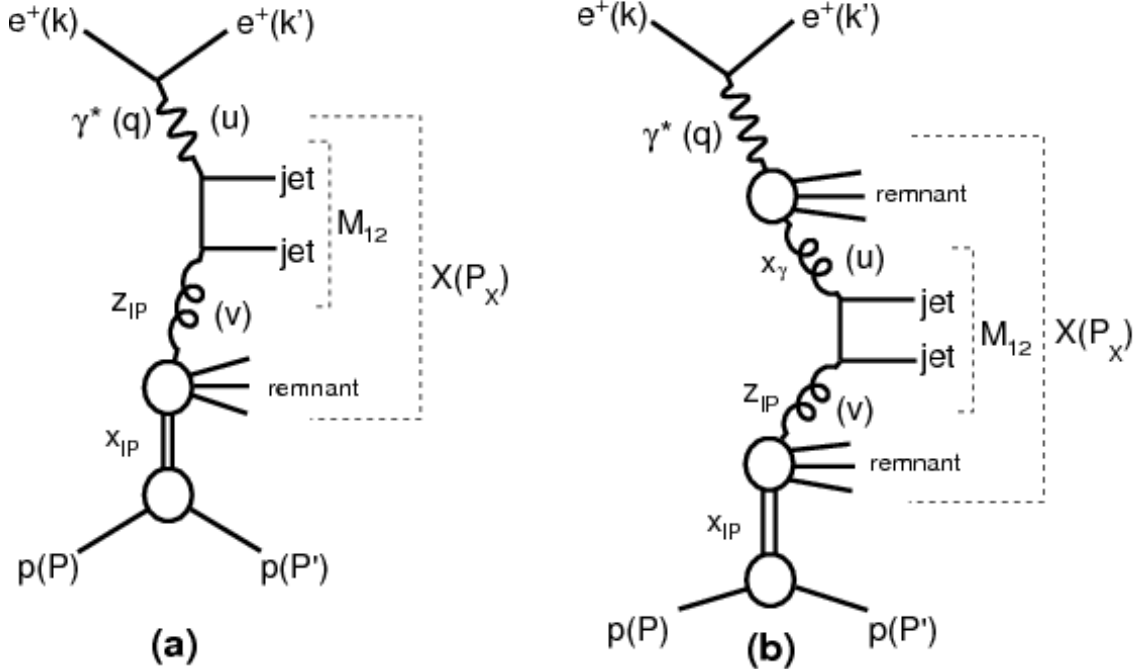


Figure 2.8: Feynman diagrams for coherent jet photoproduction in (a) direct photon in ep interactions, (b) resolved photon in ep interactions. [99].

The diffractive dijet cross section is expressed by the convolution of partonic cross sections  $d\hat{\sigma}$  and diffractive PDFs  $f_{i/p}^D$ .

$$\sigma(ep \rightarrow e + 2\text{jets} + X' + p) = \sum_i \int dt \int dx_{\mathbb{P}} \int dz_{\mathbb{P}} d\hat{\sigma}_{ei \rightarrow 2\text{jets}}(\hat{s}, \mu_R^2, \mu_F^2) \times f_{i/p}^D(z_{\mathbb{P}}, \mu_F^2, x_{\mathbb{P}}, t), \quad (2.7)$$

where  $x_{\mathbb{P}}$  is longitudinal momentum fraction lost by the incoming proton,  $d\hat{\sigma}_{ei \rightarrow 2\text{jets}}$  is the partonic cross-section for the process,  $z_{\mathbb{P}}$  is the longitudinal momentum fraction of the Pomeron entering the hard process,  $\hat{s}$  is the squared invariant energy of the subprocess,  $\mu_R^2$  is the squared renormalization scale,  $\mu_F^2$  is the squared factorisation scale,  $f_{i/p}^D$  is the diffractive parton distribution, and  $t$  is the four-momentum transfer squared at the vertex.

In the proton-vertex factorisation hypothesis, the dependence on  $x_{\mathbb{P}}$  and  $|t|$  is factored out of the dependence on  $\mu_F^2$  and  $z_{\mathbb{P}}$ . Furthermore,  $f_{i/p}^D$  is sum of contributions from the pomeron and Reggeon:

$$f_{i/p}^D(z_{\mathbb{P}}, \mu_F^2, x_{\mathbb{P}}, t) = f_{\mathbb{P}/p}(x_{\mathbb{P}}, t) f_{i/\mathbb{P}}(z_{\mathbb{P}}, \mu_F^2) + n_{\mathbb{R}} f_{\mathbb{R}/p}(x_{\mathbb{P}}, t) f_{i/\mathbb{R}}(z_{\mathbb{P}}, \mu_F^2), \quad (2.8)$$

where  $\mathbb{P}/p$  is the pomeron flux factor,  $f_{\mathbb{R}/p}$  is the Reggeon flux factor,  $n_{\mathbb{R}}$  is the normalization factor of the Reggeon,  $f_{i/\mathbb{P}}$  is the pomeron parton distribution, and  $f_{i/\mathbb{R}}$  is the Reggeon parton distribution. Figure 2.9 compares the cross-section of H1 data to that predicted by NLO-QCD [99]. The H1 data was compared to predictions based on NLO-QCD convoluted with diffractive parton distribution functions (DPDFs) from HERA inclusive diffractive deep-inelastic scattering (DDIS) data. For diffractive pp collisions the high transverse momentum jets yield a hard scale for perturbative QCD [104].

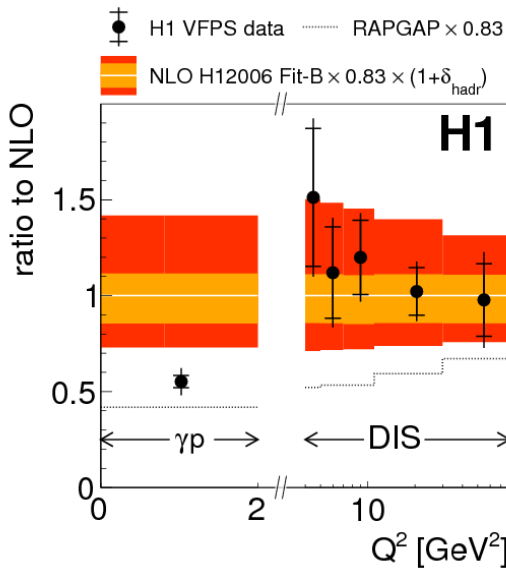


Figure 2.9: Ratio of H1 data cross section to NLO-QCD cross section [99].

H1 used the Very Forward Proton Spectrometer (VFPS) to trigger on low  $Q^2$  protons. The VFPS consists of two Roman Pots located 218 m and 222 m from the H1 interaction-point in the forward direction. The VFPS can detect protons scattered at very low transverse momentum, corresponding to  $0.008 < x_P < 0.028$  and  $|t| < 0.6$ . Each of the Roman Pots contains layers of scintillating fibers, which are covered by a layer of scintillator tiles. The fibers readout to photomultipliers, and the tiles both shield from radiation and trigger on protons. The track efficiency of VFPS is a remarkable 96%, and the background contamination is kept at 1% , making the detector excellent for studying diffractive events [99].

H1 used the RAPGAP MC generator to model diffractive  $e + p \rightarrow e + X + p$  processes. The

requirement of a leading proton, remaining intact or dissociating into a low energy state, was used to sample diffractive events. The collision product kinematics of data and MC are shown in figure 2.10. Not only is the data in good agreement with predictions from RAPGAP, but the cross section of diffractive  $e + p$  scattering is well described by calculations based on DPDFs. For this process,  $\beta$  refers to the fraction of the pomeron's longitudinal momentum transferred to the parton within the nucleus [103].

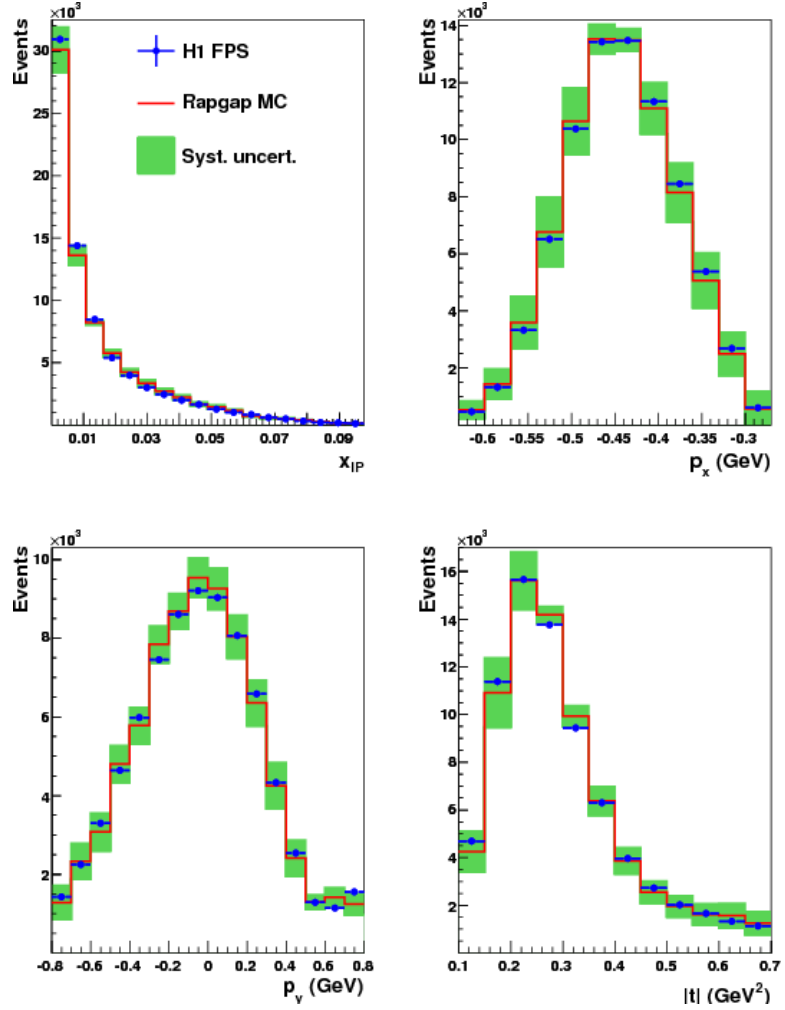


Figure 2.10: H1, diffractive  $e + p$  products, kinematics [103].

## 2.4 Wigner distribution

The Wigner distribution was first developed as part of an attempt by Eugene Wigner to map solutions to Schrödinger equation into phase probability distributions, i.e. a statistical mechanics interpretation of quantum mechanics.

$$P(x, p) \stackrel{\text{def}}{=} \frac{1}{\pi\hbar} \int_{-\infty}^{\infty} \psi^*(x+y)\psi(x-y)e^{2ipy/\hbar} dy \quad (2.9)$$

The Wigner distribution  $P(x, p)$  can be used to calculate the expectation value of any given variable by considering the Wigner transformation  $g(x, p)$  of that variable's operator,  $\hat{G}$ ,

$$\langle \hat{G} \rangle = \int dx dp P(x, p) g(x, p) . \quad (2.10)$$

Notice that in order to derive expectation values, the probability distribution must be integrated with respect to a function of position or momentum, which are still non-commuting according to the uncertainty principle.

The Wigner distribution is a quantum phase space distribution that describes "elliptic" gluons [105]. Specifically, by considering the color dipole scattering amplitude, the angular correlation of the nucleon recoil momentum and the dijet transverse momentum can provide a three-dimensional, tomographic image of the gluons within a high energy nucleus. This tomographic image takes the form of a Wigner distribution, which contains all the information of both TMDs and GPDs without violating the uncertainty principle. Specifically, the angular correlation directly measures the Fourier transform of the gluons. This is possible because the dipole amplitudes are functions of the impact parameter, and because collinear factorization holds.

TMDs and GPDs manifest non-perturbative QCD effects. The Wigner distribution, at this scale, reflects the relationship between the position and momentum of partons. Integrating the Wigner function over the transverse distance yields the TMD, while integrating over transverse momentum yields a GPD with spatial information. Figure 2.11 shows the relationships of different types of parton distribution [106].

Yoshitaka Hatta uses the dipole framework to show that the azimuthal angular correlations of coherent dijets are generated by the underlying Wigner distribution of the small-x gluons [107].

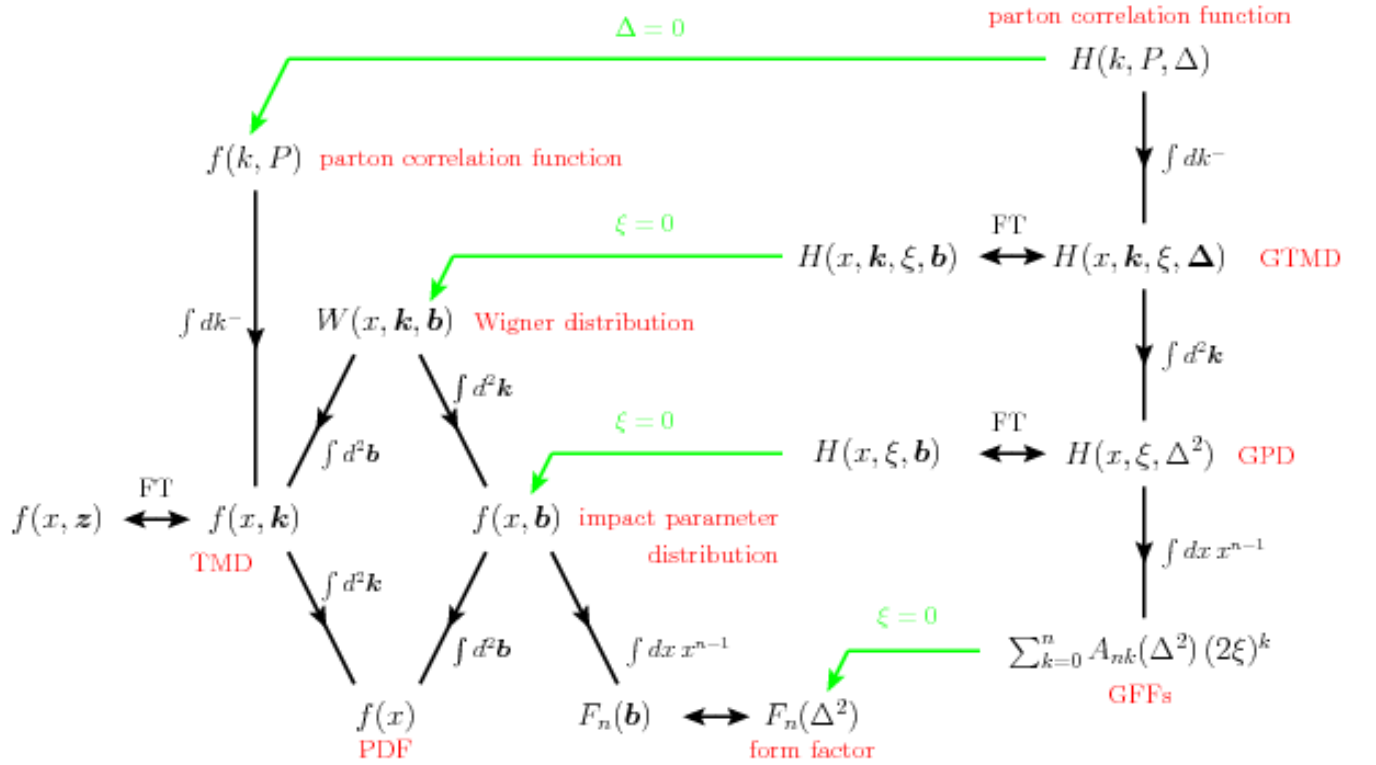


Figure 2.11: Interconnectedness of parton distributions [106].

Furthermore, these correlations are consistent with predictions based on standard collinear factorization [12]. The diagram shows a virtual photon interacting with a nucleon.  $k_1$  and  $k_2$  are the transverse momenta of the final state jets. These jets originate from a quark-antiquark pair [4].

# **Chapter 3**

## **The CMS experiment at CERN LHC**

The analysis presented in this thesis has been carried out using data from the CMS experiment. In this chapter we will first give an overview of the CERN Large Hadron Collider, and then describe the CMS detector in general and justify the reason why the CMS detector is a suitable machine to study this physics process.

### **3.1 Large Hadron Collider**

The Large Hadron Collider (LHC) has a radius of approximately 27 kilometers; as of this writing, it is the largest machine ever constructed. The initial purpose of the LHC was to discover the Higgs boson, and it is capable of investigating a wide variety of other physics phenomena such as dark matter, extra-dimensions, and heavy-ion physics.

The beams are accelerated along a circular path using radio frequency cavities, gaining energy with each revolution. LHC is a hadron collider, meaning it is designed to collide particles made of quarks and gluons. The proton-proton, proton-Pb, and Pb-Pb collision energies are the largest ever probed experimentally. The LHC is a circular collider [108].

#### **3.1.1 ATLAS**

"ATLAS" stands for "A Toroidal LHC ApparatuS". ATLAS was designed as a general purpose detector for LHC physics. Three toroidal superconducting magnets provide the field for particle identification. The looser design constraints of the ATLAS magnets allow for a more efficient, stand-alone measurement of muon momentum [109].

### **3.1.2 ALICE**

"ALICE" stands for "A Large Ion Collider Experiment". ALICE was designed to study the quark-gluon plasma in ultra-relativistic heavy-ion collisions. The primary design consideration was the correct identification of particle species at high multiplicities. ALICE retains excellent PID at approximately  $dN/d\eta = 4000$  in PbPb collisions, and this over a particle momentum range up to 100 GeV. PID is accomplished through a combination of time-of-flight chambers, muon detectors, and the analysis of specific ionization energy [110].

### **3.1.3 LHCb**

"LHCb" stands for "Large Hadron Collider beauty", reflecting the LHCb's purpose: b-quark ("beauty") studies. By examining CP violation in heavy-quark hadrons, LHCb hopes to elucidate the asymmetry of matter and antimatter. LHCb is asymmetric in the z-axis: b-hadron pairs tend to scatter in the same forward rapidity, so the experiment only covers  $1.9 < \eta < 4.9$ . A large dipole magnet projects a field in the vertical plane of LHC. Small asymmetries in the transverse scattering of the b-hadron system are used to test for CP violation [111].

### **3.1.4 TOTEM**

"TOTEM" is a sub-experiment located at CMS. TOTEM uses Roman Pots (RPS), placed far forward of CMS, to measure the total proton-proton interaction cross-section. The RPS have high acceptance for the flux very close to the beam. There are two sets of RPS, one on each side of CMS, located approximately 400 meters down the z-axis from the interaction point. The differential cross section of proton-proton scattering grows exponentially with the  $|t|$  at low values of  $|t|$ . More precise measurements of this differential cross section can help distinguish between competing models of proton structure. Furthermore, the total interaction cross section is an important benchmark for analyzing cosmic ray showers, and can be used to independently calibrate the beam luminosity measured at other LHC experiments. Diffractive studies at TOTEM complement those

at CMS.

### 3.1.5 CASTOR

CASTOR – Centauro And Strange Object Research – is a calorimeter at CMS covering 5.1 – 6.55 pseudorapidity. The calorimeters are both electromagnetic and hadronic, and located on either side of CMS, beyond the hadronic forward calorimeters. CASTOR was designed to detect centauro events which are thought to be caused by exotic matter produced in heavy-ion collisions. Typical centauro events are low multiplicity and high transverse momentum of the order of 100 GeV/c, with suppressed electromagnetic activity. There is also the possibility of a very high energy, high penetrating particle in the forward region : the so called "long flying component". Centauro events have already been observed in cosmic-ray experiments, and there are phenomenological models for their production in QGP, and while these events have not been observed at the LHC, CASTOR provided interesting measurements related to very forward inclusive dijets sensitive to saturation physics [112].

## 3.2 Compact Muon Solenoid

The Compact Muon Solenoid (CMS) is a general-purpose particle detector located at Point-5 of the LHC interaction point. CMS was designed to precisely measure the momentum of muons. The titular superconducting solenoid magnet was designed to generate a 4 Tesla field and has been operating at 3.8 T to increase longevity. This field is homogeneous and parallel to the beam line close to the interaction point. The momentum of muons are measured from how they deflect when moving through the magnetic field [113]. Altogether, CMS weighs approximately 12,500 metric tons, with a diameter of 14.6 m and a length of 21.6 meters [114].

The solenoid volume contain silicon pixel and strip tracker, a lead tungsten crystal electromagnetic calorimeter (ECAL), and a brass and scintillator hadron calorimeter (HCAL), each composed of a barrel and two endcap sections. Fig.3.1 radial layering of CMS component systems [115].

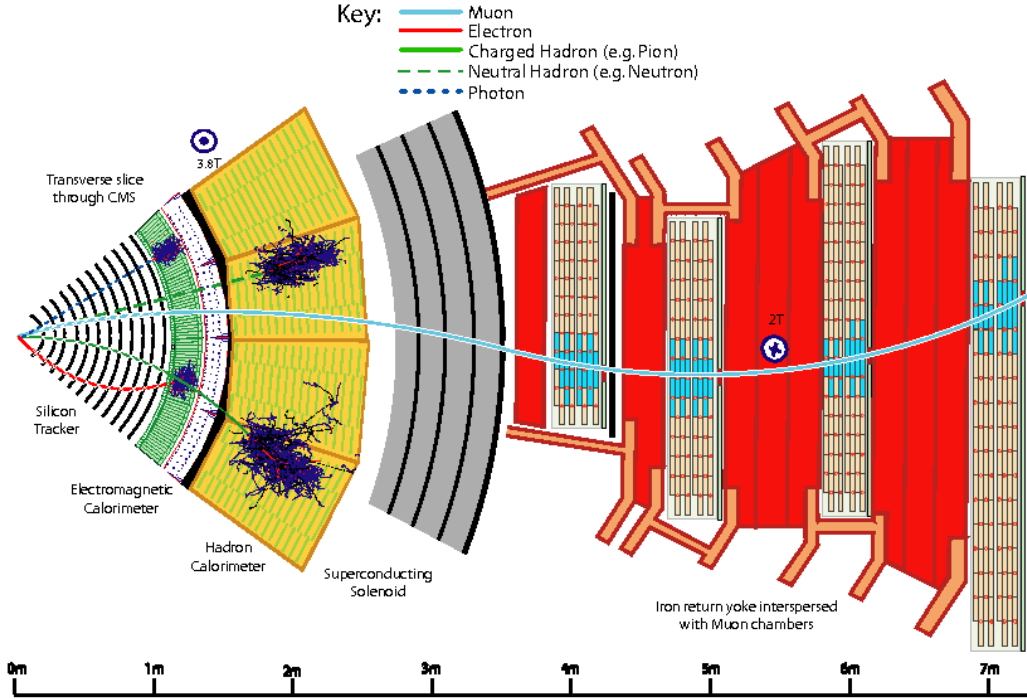


Figure 3.1: Cutout of CMS; radial cross section view [115].

### 3.2.1 Tracker

The tracker measures the momentum of charged particles via their trajectory through a homogeneous magnetic field. The tracker consists of two units, the pixel tracker and the strip tracker, both of which are made of silicon. Compared to large-volume gas detectors, which are less expensive, silicon detectors have a faster response time. The number of tracker layers is optimized for the highest penetration by charged particles while minimizing the occurrence of multiple scattering [116].

Multiple scattering reduces the efficiency and resolution of the tracker because of bremsstrahlung. When a charged lepton passes through an electric field, the changes in acceleration will change the energy of lepton. The lepton will release photons that will contaminate the signals read by the tracker.

The high luminosities reached by LHC in the proton-proton run mode typically achieve some 20 to 30 collisions per bunch crossing, and increasing the number of hits in the tracker improves the pattern recognition of the particle flow algorithm (see section 3.2.6).

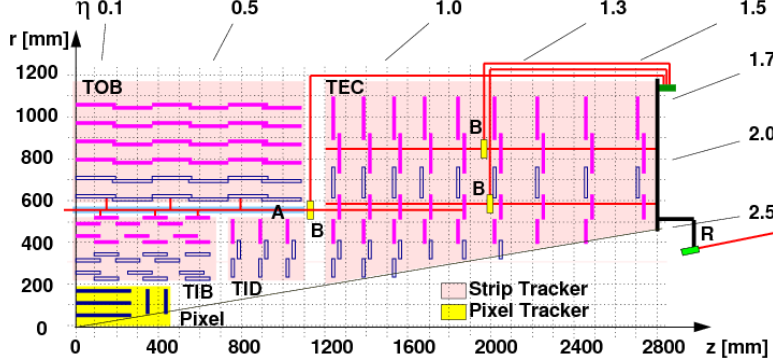


Figure 3.2: Pseudorapidity acceptance of tracker [117].

A charged particle causes an electrical signal when passing through a silicon pixel or silicon microstrip. CMS reconstructs these electrical signals, taken at specific points of position and time, into tracks. These tracks are accurate to 10 micrometers. The tracker is meant to have a particle pass all the way through it, with only minimal effect particle's trajectory.

The tracker system is designed for high granularity and fast readout, such that each trajectory can be associated with its corresponding bunch crossing. The tracker is resilient enough to withstand the high flux of particles accompanying every bunch crossing; at design luminosity of  $10^{34} \text{ cm}^{-2} \text{ s}^{-1}$ , some 1000 particles will traverse the tracker every 25 ns. However, the mass of the tracker is minimal enough to suppress multiple scattering, off its material, that would distort particle trajectories. These design constraints – resistance and transparency – are satisfied silicon. The tracker has approximately  $200 \text{ m}^2$  of silicon surface, making it the largest silicon detector ever constructed. The pseudorapidity coverage of the pixel and strip trackers is shown in figure 3.2 [117].

In addition to excellent track reconstruction, the tracker provides high precision vertex reconstruction. Vertex reconstruction is a key ingredient in several high-profile LHC studies – Higgs, SUSY, extra-dimensions – because of the use of vertices in distinguishing non-prompt decays of heavy-quarks. The tracker is also instrumental in detecting the leptonic decays of W and Z bosons.

### 3.2.1.1 Pixel tracker

The first layer of the tracker is made of silicon pixel modules. This layer has a time resolution on the scale of 25 ns, meaning that it can take data for individual bunch crossings. Pixel technology is used because the high flux of particles, present at high beam luminosities, require high spatial resolution for proper pattern recognition. A major design constraint is that the pixel tracker had to be able to separate distinct tracks in high multiplicity environments. Tracks reconstructed by the pixels can be used to cross-check the results from the other parts of the tracker.

Every silicon-pixel has a corresponding readout chip. The readout chips are soldered through the bump-bonding method. The readout chip amplifies signals from the pixel. The pixel tracker is precise enough to distinguish the vertices of tracks originating from short-lived particles, such as bottomonia. The innermost elements of the pixel tracker come within 4.4 cms of the CMS interaction point. The pixel tracker covers a pseudorapidity range of  $|\eta| < 2.5$  with some  $66 \times 10^6$  separate pixels.

### 3.2.1.2 Strip tracker

Outside the pixel tracker are the layers of the strip tracker. They function similar to the components of the pixel tracker, except the strip tracker consists of thin silicon plates. The strip tracker itself can be broken down into four components: the inner barrel layer, the inner endcaps, the outer barrel layer, and the outer endcaps. In total, these layers contain some  $9.3 \times 10^6$  strips.

## 3.2.2 Electromagnetic calorimeter

The Electromagnetic Calorimeter (ECAL) is the dedicated CMS calorimeter for detecting electrons and photons. The calorimeter is comprised of lead tungstate ( $PbWO_4$ ) crystals arranged in cylinder about the beam, including two endcaps, as seen in Figure 3.3 [118]. The granularity of these crystals gives the ECAL excellent energy resolution, angular resolution, and spatial resolution; for example, the ECAL has the resolution suitable for the decay of the Higgs boson into two photons.

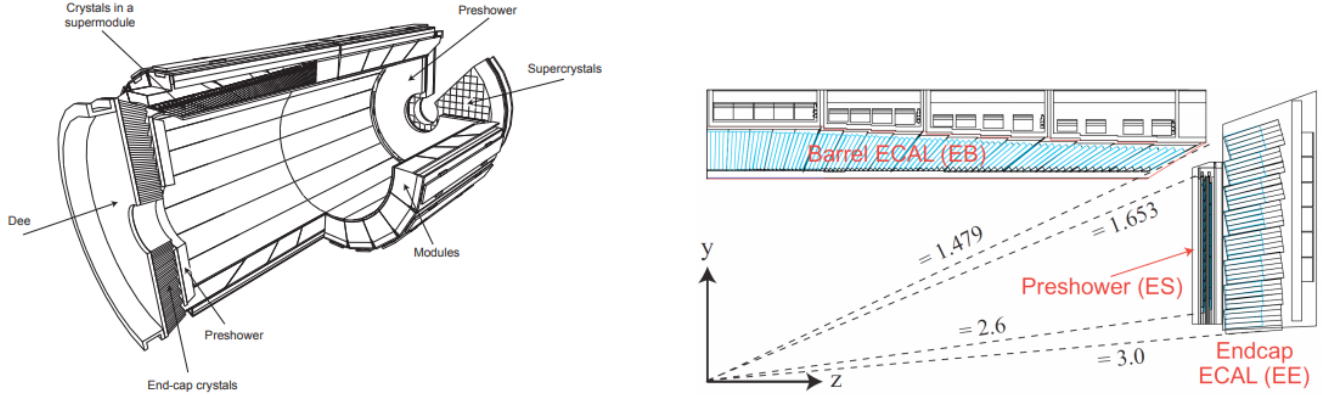


Figure 3.3: ECAL components [118].

The ECAL is both hermetic and homogenous [119].

The data readout is fast enough that CMS can trigger off signals in the ECAL. It takes about 25 ns for an ECAL hit to scintillate 80 percent of its lights, putting the calorimeter's rate on the same scale as the bunch crossing. Scintillation in the crystals activates photodetectors that transmit information to the L1 trigger. In the barrel these photodetectors are avalanche photodiodes (APDs). The endcaps use vacuum phototriodes (VPTs). ECAL's energy resolution, as a function of energy, is given by figure 3.4 [120]. The resolution increases with energy because, at large energies, parton showers become more similar as their random fluctuations average-out.

In CMS trigger development, "EG" triggers fire based on energy deposits in the ECAL; Figure 3.5 gives the EG trigger energy resolution [120]. This energy comes primarily from electrons and photons. When these particles strike a tungstate crystal, the particle shower size is approximately that of the crystal. Electrons are distinguished from photons by the correlation of track to ECAL energy. The L1 trigger does not fire on tracks, which are reconstructed at the HLT level. Thus, L1 EG triggers do not distinguish between electrons and photons.

### 3.2.3 Hadronic calorimeter

The Hadronic Calorimeter (HCAL) is the next layer outside the ECAL. The HCAL is a sampling calorimeter, meaning that it absorbs particles and measures their energy and momentum via scin-

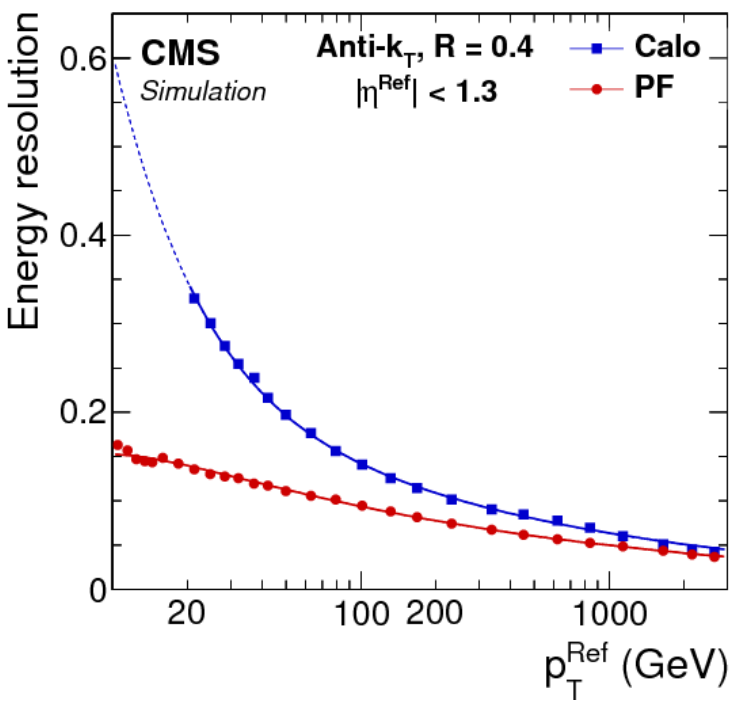
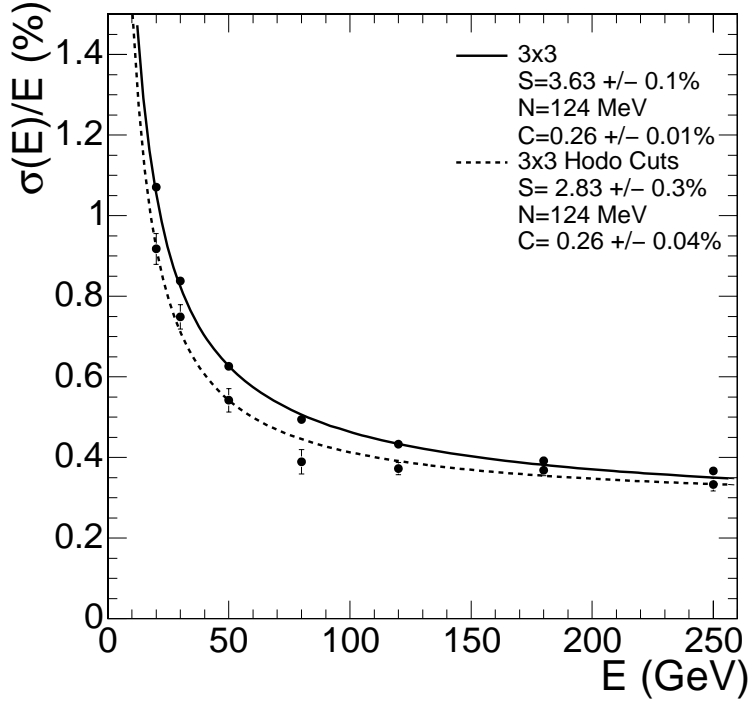


Figure 3.5: L1 trigger, ECAL energy resolution, showing the results for calorimetry (calo) and particle flow (PF) approaches [120].

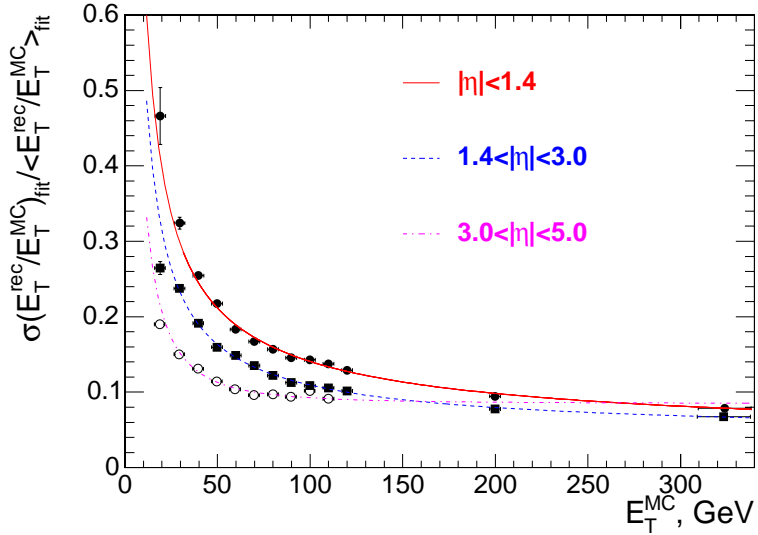


Figure 3.6: HCAL energy resolution as a function of pseudorapidity [120].

tillation. HCAL has such a large acceptance that it can indirectly observe non-interacting particles such as neutrinos. The HCAL is designed to be hermetic, so that imbalances of momentum and energy can be precisely measured [121]. Figure 3.6 plots the HCAL’s energy resolution; note that the resolution changes with  $|\eta|$  [120].

There are four sub-sections of the HCAL: the inner barrel (HB) and the outer barrel (HO), two endcaps (HE), and two forward calorimeters (HF). The HF are the most relevant to this analysis because of their use in triggering on non-hadronic events. Figure 3.7 shows the HCAL components and their locations [120].

### 3.2.3.1 Hadronic forward calorimeters

The Hadronic Forward Calorimeters (HF) absorbs the greatest portion of energy from collisions. As named, it is located in the forward region ( $3.0 < |\eta| < 5.2$ ) of CMS and complements the coverage provided by the barrel and endcap detectors.

HCAL is made of quartz fibers and steel absorbers for maximum radiative resistance. When high energy particles pass through the quartz fibers, these particles are moving faster than the speed of light in the medium, depositing energy that causes particle showers. These showers give off light, in the form of Cherenkov radiation, that the fibers transmit to photomultiplier tubes (PMTs).

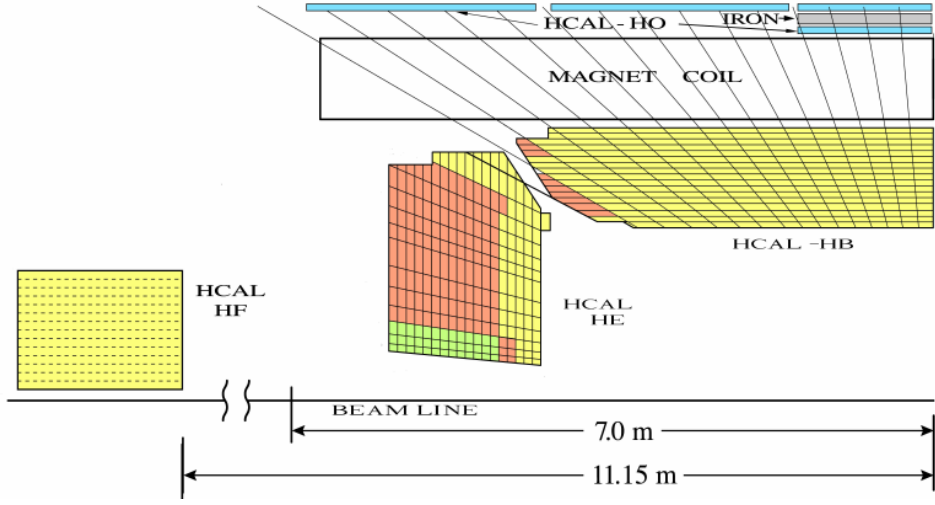


Figure 3.7: HCAL components; HB, HE, and HF [120].

The PMT signals are converted into a digital signal by a charge integration encoder (QIE) chip. Then HCAL trigger and readout boards (HTR) use these digital signals to calculate luminosity. The HTR information is part of the data used for L1-triggering. Triggering on HF can also be done by vetoing on HF activity.

Hits in the HF are used to measure the instantaneous luminosity of CMS. As shown in Figure 3.6, the HF have a finer  $E_T$  resolution than the other parts of the HCAL, making it suitable for high precision measurement of luminosity. Furthermore, because HF electronic noise is comparatively small with respect to HF threshold for a minimum bias event, applying a veto on the HF threshold is a reliable measure for UPC processes characterized by low event activity.

### 3.2.4 Muon detector

The outermost layer of CMS consists of the muon detectors, as seen in Figure 3.8 [120]. Muons are particles nearly identical to electrons, except for their mass, which exceeds that of the electron by some two orders of magnitude. High mass particles, like the Higgs boson, often decay into a final state containing muons. The muon detector not only identifies muons, but also measures their momentum. The muon detector has a readout fast enough for triggering on muons [122] [123].

The muon detector consists of three types of component: muon drift tubes (DT), cathode strip

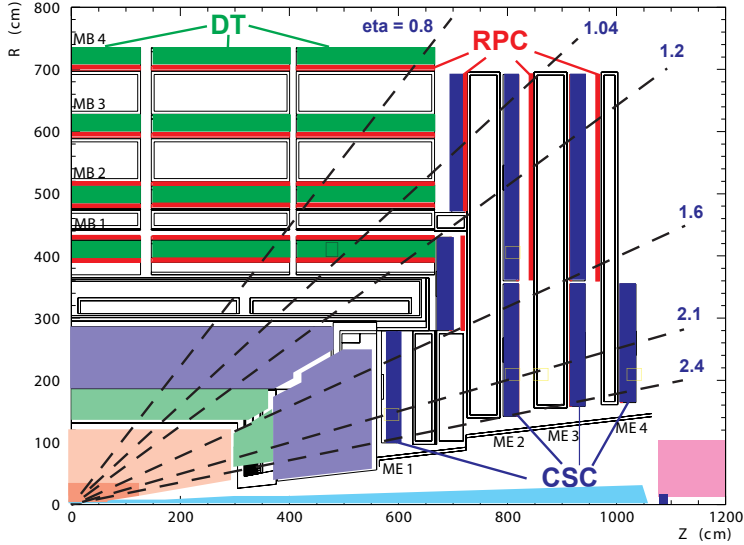


Figure 3.8: Pseudorapidity acceptance of muon detector [120].

chambers (CSC), and resistive plate chambers (RPC). The DTs are gas filled chambers that contain a stretched metal wire. When muons pass through the DT gas, electrons are excited. These electrons escape from the gas atoms and are attracted to the metal wire, which triggers a signal. The CSC, located in the endcaps, operate under similar principles, but contain perpendicular arrays of positively charged and negatively charged wires immersed in gas. The RPC do not use electrode wires to detect excited electrons; instead, high-resitivitiy plates are used as alternating cathodes and anodes [124].

### 3.2.5 Zero degree calorimeter

The zero degree calorimeters are located at both sides of CMS, approximately 140 meters from the interaction point. Each ZDC consists of two independent systems: an electromagnetic calorimeter, for detecting very forward photons, and a hadronic calorimeter, for detecting neutrons. Because these neutrons result from the dissociation of nuclei, the ZDC can measure the centrality of heavy-ion collisions. Hadrons in the forward region have energy on the TeV scale, so the ZDC's hadronic calorimeter is made of thick tungsten plates [125]. For a UPC process, the photon emitting nucleus is most likely to remain intact; therefore, ZDC data can the photon direction of a process, and by

extension its energy. Tagging forward neutrons can also be used as an online luminometer [126].

### 3.2.6 Particle flow algorithm

Raw data from the sub-detectors is combined, for data analysis, by the particle-flow (PF) algorithm. The PF takes the data about tracks in the tracker and energy deposits in the calorimeter, and uses them to reconstruct physics-related data objects like jets and to identify specific particles, such as photons and muons. The PF also identifies missing energy and momentum for use in neutrino studies.

Unlike physics-objects in the data of previous experiments, PF physics-objects can fire HLTs. After an event passes the L1 trigger, a partial event reconstruction is performed. Energy deposits in the HCAL that can be associated with a track signify charged hadron candidates; if the track-associated energy deposit is in the ECAL, the corresponding object is an electron candidate. Tracks not associated with a calorimeter deposit are considered muon candidates. Left over energy deposits are used to create neutral hadron candidates, if in the HCAL, or photon candidates, if in the ECAL. Each of these candidates is assigned a four-vector based on the sub-detector information [127].

The collection of basic PF candidates are used to create more complex physics objects. The total transverse momentum of the event is used to locate "missing transverse momentum" (MET). MET candidates have a four-vector, and can be used to construct exotic physics-objects such as neutrinos. The curvature of tracks is used to measure the momentum and charge to mass ratio of the charged hadrons, and thus their particle species. The identity of the particles can then be interpreted as the decay of short-lived particles, such as the  $\tau$  lepton. The speed and efficiency of the calculation and combination of PF objects enables CMS to trigger for a wide variety of physics by modifying software.

The PF is also responsible for implementing the jet reconstruction algorithms of CMS. In the analysis presented in this thesis the anti- $kt$  jet reconstruction algorithm. Anti- $kt$  algorithms are sequential algorithms that take into account two quantities: the distance between two given particles

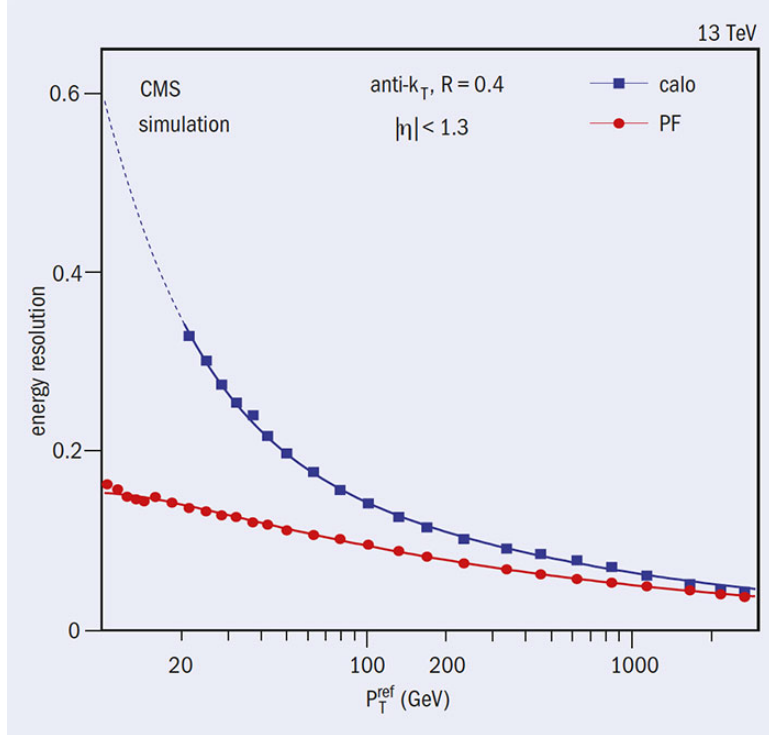


Figure 3.9: Performance of particle flow algorithm compared to calorimeter readout [129].

$i$  and  $j$ ,  $d_{ij}$ , and the distance between a given particle  $i$  and the beam,  $d_{iB}$ . For a specific particle  $i$ , all the  $d_{ij}$  and  $d_{iB}$  are calculated. If the smallest quantity in the collection is  $d_{ij}$ , the particles  $i$  and  $j$  are combined as four-vectors. The sum four-vector replaces particle  $i$ , and all of the distances are recalculated. If the smallest quantity  $d_{iB}$  is the smallest quantity, then  $i$  is designated a "jet" and removed from the collection. This process iterates until all particles are removed from the collection, replaced by "jets" associated with one or more particles [128].

CMS gains significant jet reconstruction efficiency via the PF. At low transverse momentum, PF reconstructs jets at nearly twice the resolution of HCAL and ECAL. This increase in efficiency comes from the PF integrating in track data with the calorimeter tower data. Figure 3.9 compares the performance of the PF algorithm to the calorimeter reconstruction [129].

CMS was the first modern collider experiment to replace traditional triggering, based on energy-deposits and tracks, with HLTS leveraging PF-reconstructed particles. This achievement was enabled by the high precision, high accuracy technologies described in this chapter. Experimentalists, now more than ever, prepare their analyses with unprecedentedly accurate analogues to processes

calculated by theorists. For a given process, a theorist can determine the properties of the final state particles, and encode these in an MC generator. Experimentalists can then run the MC through a simulation of CMS and compare what the PF reconstructs to the MC-truth. This technique is particularly useful for emulating the performance of trigger menus for specific particle productions [127].

# Chapter 4

## Measuring luminosity

Although the analysis results presented in this thesis do not require a precise knowledge of the measured luminosity, it is important to introduce it since the author contributed in this direction.

### 4.1 Instantaneous luminosity

One of the most important quantities measured by CMS is luminosity. Luminosity is necessary to convert the number of events detected, for a given channel into a collision cross section. Collision cross sections are among the primary observables predicted by theoretical physicists. For particle physics, the collision cross-section of a process is typically measured through the relation:

$$\sigma = \frac{R}{L}, \quad (4.1)$$

where  $\sigma$  is the cross section,  $R$  is the rate at which the process occurs per collision, and  $L$  is the instantaneous luminosity.  $L$  is measured via the rate of a given luminometer and taking into account the acceptance  $A$

$$L = \frac{R}{\sigma_o(E)A(t, \mu, n_b, \dots)}, \quad (4.2)$$

The denominator is typically measured as the visible cross section,  $\sigma_{vis}$ ,

$$\sigma_{vis} = \sigma_o(E)A(t, \mu, n_b, \dots), \quad (4.3)$$

where  $\sigma_o(E)$  comes from separating out the dependence of  $\sigma_{vis}$  on collision energy E.  $\sigma_{vis}$  ideally has no dependence on time or experiment conditions, i.e. constant with respect to pile-up and invariant to filling scheme. For example activity in the HF scales with the instantaneous luminosity. Therefore, the visible cross-section – which has no time dependence – can be used as calibration constant for converting the rate of HF activity into instantaneous luminosity. Every luminometer

should have its own characteristic visible cross section. In this way, multiple independent luminometers can cross check each other [130–132].

## 4.2 Luminometers

Within CMS, the Beam Radiation and Luminosity (BRIL) group is responsible for providing luminosity measurements and studying the radiation levels for the various detectors. There are two kinds of CMS luminometer: online and offline. Online luminometers readout the luminosity per bunch in real time. As of 2015 there are three online luminometers: the pixel luminosity telescope (PLT), the HF, and the beam conditions monitor (BCM1f). There is a high-rate, independent data-acquisition system for each of the online luminometers. Offline luminometers measure the rate of reconstructed objects. The primary offline lumimometer is the pixel tracker. In general, the offline lumimometers have better stability over time. [133]

The online and offline luminometers complement each other for high precision data analysis. Specifically, the offline data can be used to calibrate out imperfections in the online data.

In addition to these hardware luminometers, CMS can use physics processes as luminosity benchmarks. For example, the measured the Z-boson cross-section to a high accuracy and high precision is an alternative.

### 4.2.1 Pixel cluster counting

One of the primary methods of measuring instantaneous luminosity is through pixel cluster counting (PCC) in the pixel-tracker. The collision rate is linked to instantaneous luminosity  $L$  via the total inelastic cross-section  $\sigma_T$

$$v\mu = L\sigma_T, \quad (4.4)$$

where  $v = 11246$  Hz is the beam revolution frequency and  $\mu$  is the number of collisions per bunch crossing. We define the average number of pixel clusters per event,  $\langle n \rangle$ , as

$$\langle n \rangle = \mu n_1, \quad (4.5)$$

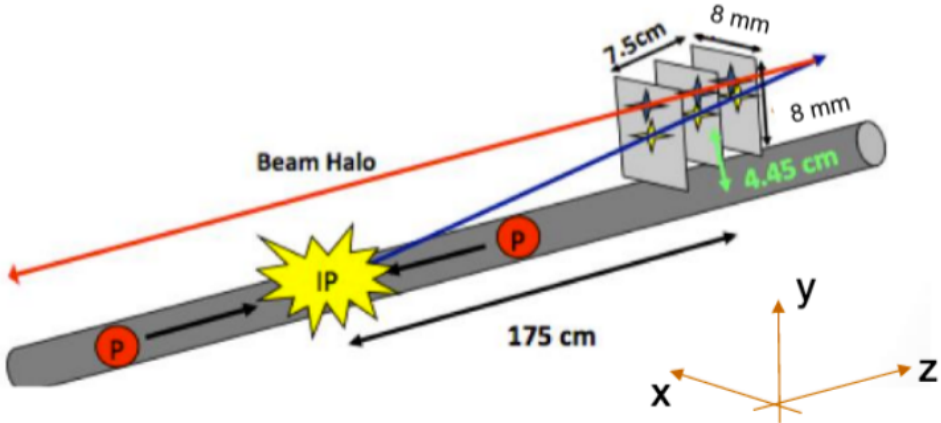


Figure 4.1: PLT triple coincidence.

and the visible cross section  $\sigma_{vis}$  as

$$\sigma_{vis} = \sigma_T n_1, \quad (4.6)$$

where  $n_1$  is the average number of pixel clusters per inelastic collision. Leveraging the previous two equations, the instantaneous luminosity reduces to

$$L = \frac{v \langle n \rangle}{\sigma_{vis}}, \quad (4.7)$$

such that  $L$  can be calculated after measuring the actual  $\langle n \rangle$  of the data [130]

## 4.2.2 Pixel luminosity telescope

The pixel luminosity telescope (PLT) is one of the online luminometers of CMS. The PLT consists of 8 pixel telescopes arranged around the beamline on either side of the CMS interaction point. Each telescope has three layers of silicon pixel detector. Triple coincidences in these telescopes are measured as luminosity on a bunch-by-bunch basis. As an independent luminometer, the PLT data is also useful for reducing the systematic uncertainty of the luminosity delivered to CMS.

The PLT was installed as part of the CMS Run-2 upgrades. The hardware of the pixel sensors and the readout chip are similar to those used by the pixel tracker. However, the readout chips (ROC) of the PLT are capable of delivering fast-OR formatted data; the pixel tracker cannot do this. The fast-OR readout is optimized for delivering triple-coincidence data; whereas the standard

pixel data readout has a maximum frequency of 100 kHz, the PLT fast-OR readout maxes out at an orders of magnitude greater frequency, at 40 MHz [134].

### 4.2.3 Hadronic forward calorimeter

As mentioned before in section 3.2.3.1, the hadronic forward calorimeter (HF) of CMS is capable of measuring luminosity. Because of the high flux of particles through the forward region, the HF-luminosity is less subject to statistical uncertainty than the PCC-luminosity. The HF can measure luminosity per bunch through its own dedicated high-rate acquisition system (HTR) that is separate from the CMS DAQ. Within the HF, the HTR boards each have an additional HF luminosity transmission circuit (HLX). The HLX are mounted in one of the mezzanine expansion slots of the HTR.

The HF luminosity is subject to two difficulties. Because the PMTs require a calibrated voltage, the accumulation of gain changes over long periods of time will cause calibration drifts. Furthermore, the HF detector response has been shown to be nonlinear with respect to vertex pile-up. Substantial data analysis goes into calculating the corrections to these two sources of error [130].

### 4.2.4 Fast Beam Conditions Monitor

The CMS Beam Conditions and Radiation Monitoring System (BRM) provides a wide variety of information on the accumulated radiation dosage into CMS. This information is essential for protecting CMS from radiation damage. There are many subcomponents to the BRM system, one of which is the Fast Beam Conditions Monitor (BCM1F). The BCM1F is capable of measuring the beam-halo background and the flux from collision products. Similar to the PLT, BCM1F is located close to the beam pipe; however, BCM1F uses diamonds instead of silicon pixels. The readout from BCM1F is not digital, but an analog signal sent through optical fibres.

There are 24 single crystal diamond sensors in the BCM1F system. The BCM1F is located very close to interaction point, specifically 1.8 m on either side. This location is chosen specifically to take advantage of the 25 ns between bunch crossings. From the BCM1F vantage point there is a

12.5 ns delay between particle fluxes from the machine induced background and those coming from actual collisions. Thus the BCM1F can use timing to distinguish between signal and background [135].

### 4.3 Van de Meer scanning calibration

The luminometers of CMS produce signals proportional to the instantaneous luminosity of the LHC beam. However, these signals need to be properly calibrated with respect to a known visible cross-section for each luminometer. This calibration is accomplished via Van de Meer scanning [136]. The opposing beams of LHC are moved back and forth in the transverse plane. During the scan, the detector response is measured as a function of beam displacement. The beam widths are calculated from Gaussian fits to the detector response. The visible cross-section of the luminometer in question is then derived from the width of the beams, and acts as the calibration of the detector response. Figure 4.2 presents the fitting of the VdM scan in the X and Y planes [130]. The visible cross section, in terms of VDM scan variables, is

$$\sigma_{vis} = \frac{2\pi\Sigma_x\Sigma_y v \langle n \rangle_{\Delta=0}}{N_1 N_2}, \quad (4.8)$$

where  $\Sigma_x\Sigma_y$  is the beam overlap,  $v$  is the revolution frequency,  $\langle n \rangle_{\Delta=0}$  is the amplitude of the VDM rate profile, and  $N_1 N_2$  is the product of the number of protons (or heavy-ions) in the beams.

### 4.4 Corrections to VDM scans

Several corrections must be applied to VdM scan data before calculating the visible cross section. These corrections are considered uncorrelated, i.e. it does not matter in what order they are applied. The results of the VDM scan must be corrected for the following phenomena: the length scale, the ghosts and satellite background, the growth in beam emittance, orbit drift, and beam-beam electromagnetic effects. These affect the normalization of the VDM scans, and so the corrections take the form of calibration constants derived from additional scans and beam monitoring subdetectors [130].

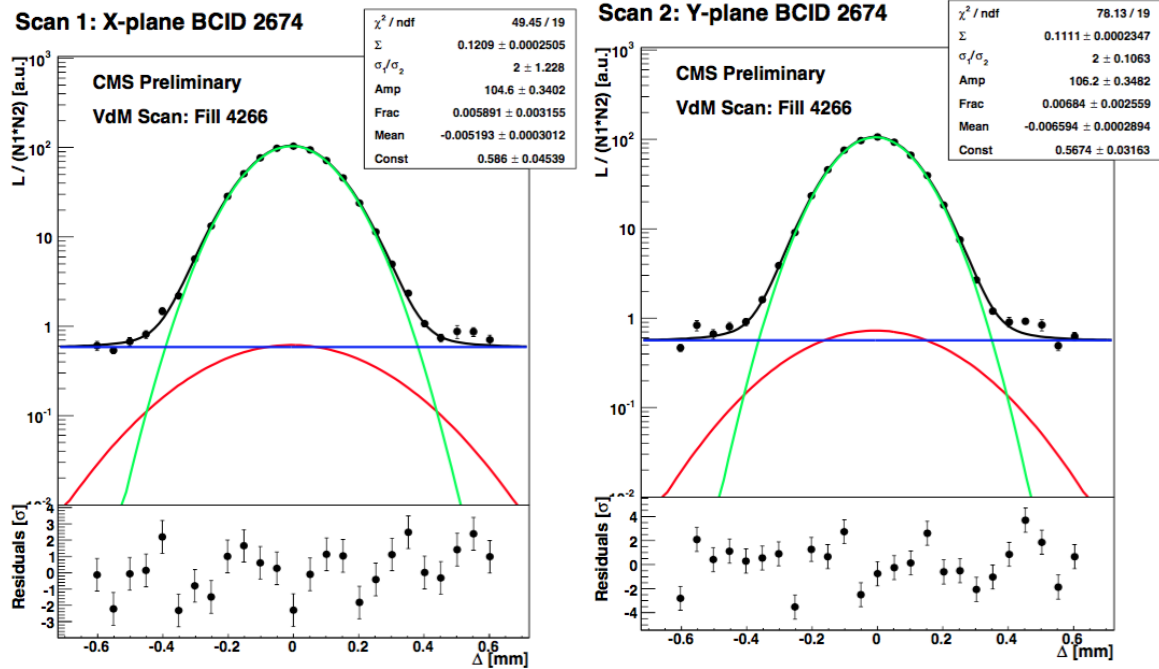


Figure 4.2: PCC VdM Scans [130].

The length scale correction is derived by comparing the effects of a length scan to the response of the tracker; checking the difference between the reported beam displacement and that seen in the tracker. In addition to the circulating bunches, the LHC beams can be polluted by foreign particles that were not intended for injection by LHC commissioning. The presence of these foreign particles – fleeting "ghosts" and persistent "satellites" – can be detected by comparing the total beam current, measured by the DC beam current transformer, against the per bunch current measured by the Fast Beam Current Transformers (FBCT). The FBCT, because it is timed for bunch crossings, is less likely to interact with ghosts and satellites. Variations in beam emittance affect the VdM scans by changing the amplitude and width of the rate profile. The orbit drift correction is based on data from the Beam Position Monitors (BPM), which measure the position of the beam orbit in LHC. Lastly, beam-beam effects refer to the electromagnetic forces that the beams exert on each other; for example, when the beams are transversely separated there is a small, but statistically significant, induced magnetic force.

	Systematic	correction (%)	uncertainty (%)
Integration	Stability	-	1
	type 1	7 – 9	0.6
	type 2	0 – 4	0.7
	CMS deadtime	-	0.5
	Dynamic Inefficiency	-	0.4
Normalization	XY-Correlations	1.1	1.5
	Beam current calibration	-	0.3
	Ghosts and satellites	-	0.2
	Length scale	-3.2	1.5
	Orbit Drift	-	0.4
	Beam-beam deflection	1.8	0.4
	Dynamic- $\beta$	-	0.5
	Total		2.7

Table 4.1: Systematic uncertainty during the 2015 pp run [130].

## 4.5 Systematic uncertainty

Table 4.1 displays the systematic uncertainties associated with the delivered luminosity. The "normalization" uncertainties are for the visible cross section,  $\sigma_{vis}$ . The "integration" uncertainties are for the integrated luminosity that is calculated using the  $\sigma_{vis}$ . The stability uncertainty is calculated from comparing the relative contributions of pixel tracker layers to total number of pixel clusters measured in a span of time. From run to run, each pixel layer contribution varies by no more than 1%. It is possible for the rate of high track multiplicity events to exceed the temporary storage capacity of the tracker read-out buffer; the resulting inefficiencies are mainly found in the first barrel layer of the tracker. The "afterglow" refers to background noise associated with electrical excitations in the detector material, and warrants a correction factor to the integrated luminosity.

## 4.6 Author's contributions

The 2015 heavy-ion run itself recorded about  $1.4 pb^{-1}$  in integrated luminosity. This integrated luminosity is reconstructed into data on the order of pentabytes. Table 4.2 presents LHC the 2015 PbPb run luminosity information, and presents for each fill the peak instantaneous luminosity, delivered integrated luminosity, and recorded integrated luminosity. The last column, EffbyLumi, is the ratio of the delivered to recorded integrated luminosities.

I contributed to CMS luminosity validation and performed studies on the long-term stability

Fill	Begin Time YYYY.MM.DD HH:MM	Duration HH:MM	PeakInstLumi $\times 10^{30} \text{cm}^{-2}\text{s}^{-1}$ pp $\times 10^{24} \text{cm}^{-2}\text{s}^{-1}$ ions	DeliveredLumi $\text{pb}^{-1}$ pp $\text{pb}^{-1}$ PbPb	RecordedLumi $\text{pb}^{-1}$ pp $\text{pb}^{-1}$ PbPb	EffByLumi %
4658	2015.11.25 09:59	05:40	1	0.0	0.0	84.4
4659	2015.11.25 22:51	02:12	89	0.6	0.5	95.6
4661	2015.11.26 07:04	02:55	97	0.8	0.5	69.6
4664	2015.11.26 16:33	04:27	547	5.3	4.5	85.7
4666	2015.11.27 08:34	05:05	721	7.0	6.2	88.8
4669	2015.11.27 21:31	06:10	1327	16.1	12.8	79.2
4671	2015.11.28 11:13	09:03	1115	16.5	14.3	86.9
4672	2015.11.28 23:53	06:55	1085	14.0	11.9	84.6
4677	2015.11.29 17:42	06:54	1011	14.0	12.5	89.6
4679	2015.11.30 08:27	06:58	1092	14.5	12.9	88.8
4680	2015.11.30 21:17	05:13	1820	19.6	16.7	85.4
4681	2015.12.01 07:40	11:51	1856	28.4	25.1	88.2
4685	2015.12.02 05:39	03:28	1040	8.5	6.0	70.4
4688	2015.12.03 02:44	00:18	1887	1.9	1.0	51.1
4689	2015.12.03 09:03	09:04	1254	10.2	9.9	97.1
4690	2015.12.03 22:10	08:27	2030	22.0	21.7	98.5
4691	2015.12.04 12:51	07:31	2072	26.7	25.8	96.6
4692	2015.12.04 23:23	07:40	2334	30.3	29.7	98.1
4693	2015.12.05 10:22	00:60	2314	7.1	6.9	97.2
4695	2015.12.05 17:29	07:14	2216	27.8	26.2	94.3
4696	2015.12.06 07:03	05:29	1795	19.9	19.4	97.7
4697	2015.12.06 16:34	05:30	1879	20.5	20.1	98.2
4698	2015.12.07 01:41	00:09	2102	1.0	0.9	87.2
4699	2015.12.07 05:30	05:40	1885	21.5	20.4	94.8
4705	2015.12.08 05:37	02:24	183	1.1	1.1	97.8
4706	2015.12.08 11:08	04:32	2433	23.5	22.7	96.5
4709	2015.12.09 08:41	05:47	2161	23.3	22.8	97.8
4710	2015.12.09 17:42	05:52	2967	32.8	32.2	98.3
4711	2015.12.10 02:38	06:37	2886	31.6	31.1	98.4
4714	2015.12.11 01:20	06:39	2500	29.3	28.2	96.2
4715	2015.12.11 11:37	06:31	2559	30.6	29.3	95.7
4717	2015.12.11 23:00	10:21	0	0.0	0.0	0.0
4719	2015.12.12 17:26	04:36	2652	27.2	25.6	94.1
4720	2015.12.13 01:10	10:60	3036	44.9	44.2	98.5
Summary		199:09	3036	578.4	543.1	93.9

Table 4.2: Luminosity by CMS fill.

of the BRIL luminometers. On a week by week basis, I would examine the data from online and offline luminometers and certify that it met the quality standards of CMS. If the data exhibited non-linear behavior, I would de-certify the corresponding lumi-sections in the BRIL files, which are in the JSON format.

All CMS data has to go through a data certification workflow. Data certification insures that only valid data is used in CMS analyses. Decisions on data certification are recorded in two systems: the DQM Run Registry, shown here in Figure 4.3, and the normtag JSON files of the BRIL group. There are occasions when the sub-detectors of CMS might record poor quality data. For example, the software reading out data from the PLT could crash and thus compromise the

output. In this case the certification workers would record the lumi sections during which the PLT software crashed. These lumi sections would be removed from the certifying JSON file passed on to the BRIL group. If all the luminometers are malfunctioning, a whole run could be invalidated in the run registry.

Ru...	Run Class ...	Dataset Name	Database	Dataset Created	Last Shifter	Cms	Castor	Csc	Dt	Ecal	Es
305842	Collisions17	/PromptReco/Collisions2017F/DQM	OPEN	Sun 05-11-17 02:52:33	DQMGUI Tr...	GOOD	EXCLUDED	GOOD	GOOD	GOOD	GOOD
305841	Collisions17	/PromptReco/Collisions2017F/DQM	OPEN	Sat 04-11-17 15:26:04	DQMGUI Tr...	GOOD	EXCLUDED	GOOD	GOOD	GOOD	GOOD
305839	Collisions17	/PromptReco/Collisions2017F/DQM	OPEN	Sun 05-11-17 05:13:10	DQMGUI Tr...	GOOD	EXCLUDED	GOOD	GOOD	GOOD	GOOD
305833	Collisions17	/PromptReco/Collisions2017F/DQM	OPEN	Sat 04-11-17 12:21:31	DQMGUI Tr...	GOOD	EXCLUDED	GOOD	GOOD	GOOD	GOOD
305832	Collisions17	/PromptReco/Collisions2017F/DQM	OPEN	Mon 06-11-17 11:07:35	DQMGUI Tr...	GOOD	EXCLUDED	GOOD	GOOD	GOOD	GOOD
305821	Collisions17	/PromptReco/Collisions2017F/DQM	OPEN	Sun 05-11-17 23:46:43	DQMGUI Tr...	GOOD	EXCLUDED	GOOD	GOOD	GOOD	GOOD
305814	Collisions17	/PromptReco/Collisions2017F/DQM	OPEN	Sun 05-11-17 17:47:24	DQMGUI Tr...	GOOD	EXCLUDED	GOOD	GOOD	GOOD	GOOD
305809	Collisions17	/PromptReco/Collisions2017F/DQM	OPEN	Sat 04-11-17 03:52:37	DQMGUI Tr...	GOOD	EXCLUDED	GOOD	GOOD	GOOD	GOOD
305766	Collisions17	/PromptReco/Collisions2017F/DQM	OPEN	Fri 03-11-17 22:59:06	DQMGUI Tr...	GOOD	EXCLUDED	GOOD	GOOD	GOOD	GOOD
305758	Collisions1...	/PromptReco/SpecialRun2017/DQM	OPEN	Thu 02-11-17 02:07:15	DQMGUI Tr...	GOOD	EXCLUDED	GOOD	GOOD	GOOD	GOOD
305757	Collisions1...	/PromptReco/SpecialRun2017/DQM	OPEN	Thu 02-11-17 09:02:13	DQMGUI Tr...	GOOD	EXCLUDED	GOOD	GOOD	GOOD	GOOD
305756	Collisions1...	/PromptReco/SpecialRun2017/DQM	OPEN	Wed 01-11-17 23:56...	DQMGUI Tr...	GOOD	EXCLUDED	GOOD	GOOD	GOOD	GOOD
305755	Collisions1...	/PromptReco/SpecialRun2017/DQM	OPEN	Thu 02-11-17 01:32:47	DQMGUI Tr...	GOOD	EXCLUDED	GOOD	GOOD	GOOD	GOOD

Figure 4.3: CMS Run Registry.

In addition to data certification, I reviewed the long-term stability of the BRIL luminometers during the 2015 and 2016 proton-proton runs. Stability refers to the comparative performance of the different luminometers. Ideally, the ratio of the instantaneous luminosity reported by separate luminometers should be a constant ratio, but in fact there is a tendency for this ratio to drift as a result of radiation damage to the luminometers. This drift can be seen in plotting the average ratio as a function of interaction rate and of the different measures of LHC time: runs, lumi-sections, and bunch-crossings. Instantaneous luminosity, in theory, should be independent of machine conditions like acceptance and efficiency. Figure 4.4 is records the sum of the delivered and recorded integrated luminosity for each day of the 2015 Pb-Pb run.

Figure 4.5 is the CMS-recorded integrated luminosity for each proton-proton era of LHC. Notice that as the collision energy increases, the recorded luminosity grows at steeper and steeper rate. This acceleration in the recorded luminosity is consistent with the higher multiplicity of high energy collisions. As LHC pushes the energy frontier, high quality luminosity analyses will become even more fundamental for the continued performance of CMS. The "High Luminosity

### CMS Integrated Luminosity, PbPb, 2015, $\sqrt{s} = 5.02$ TeV/nucleon

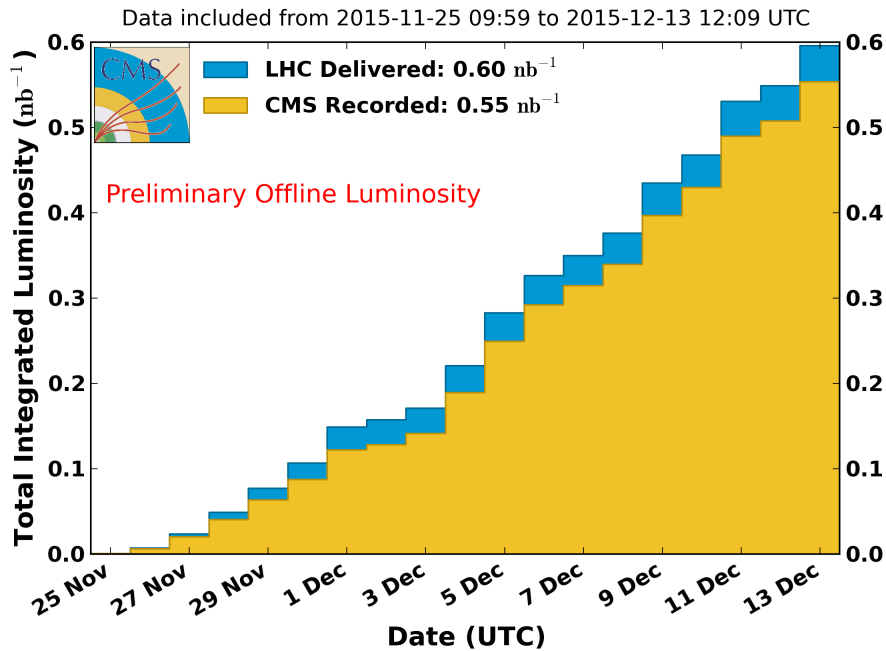


Figure 4.4: CMS lumi during the 2015 PbPb run.

Large Hadron Collider" (HL-LHC) is a project to increase the design luminosity of LHC by an order of magnitude by 2025. To fully leverage the power of this increased luminosity, particularly for studying possible anomalous couplings, CMS must continue providing measures of luminosity with tightly controlled systematic uncertainty.

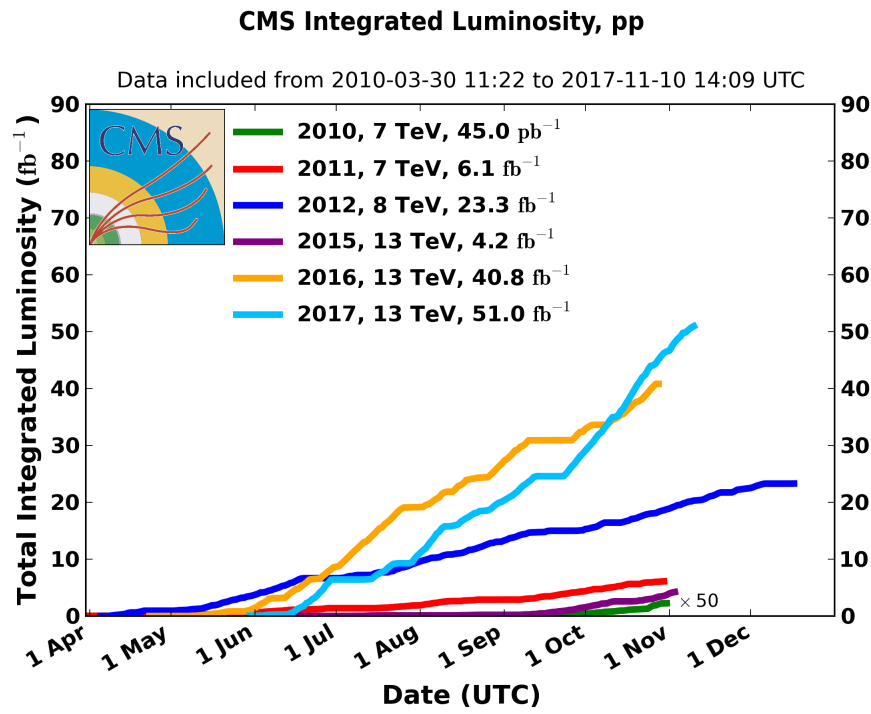


Figure 4.5: Total integrated luminosity for the various pp periods in 2010 until 2017.

# Chapter 5

## Trigger development and performance

### 5.1 Triggering at CMS

At stable beams, the LHC delivers bunch crossings every 25 nanoseconds. Each bunch crossing in turn will have some 20 hadron collisions. The resulting interaction rate –  $10^9$  interactions per second – is orders of magnitude greater than the frequency that events can be written to disk,  $10^2$  events per second. CMS therefore needs a means of filtering out the most interesting  $10^2$  interactions per second while declining the other  $10^6$  interactions per second.

CMS uses a two-tiered triggering system. The first tier, the L1 trigger, is hardware based. The second tier, the high-level trigger (HLT), is software based. The L1 trigger receives raw data from the calorimeters and the muon detectors; this determines when the tracker will readout data. The raw data from the tracker, calorimeters, and muon detectors is then passed on to a computer farm running the HLT menu. The HLT then performs a simplistic reconstruction of the raw data into physics objects useful for analysis: jets, tracks, and identifiable particles. If an event passes the HLT, the raw data is permanently stored in preparation for a more complex reconstruction [137] [138].

Figure 5.1 is an outline of the flow of information between the subcomponents of the L1 trigger. The first division is between the calorimeters and the muon detectors. Calorimeter energy deposits are registered by the regional calorimetry trigger. Zero counting information is then sent to the global calorimetry trigger. The muon detector send signals to pattern recognition circuits that associate the detector hits into low resolution tracks; the hits and tracks are then sent to the global muon trigger. The global calorimetry trigger and the global muon trigger then combine at the

global trigger, which uses information from the TTC (Timing, Triggering, and Control) system to synchronize signals back to the tracker, ECAL, HCAL, and muon detectors [139].

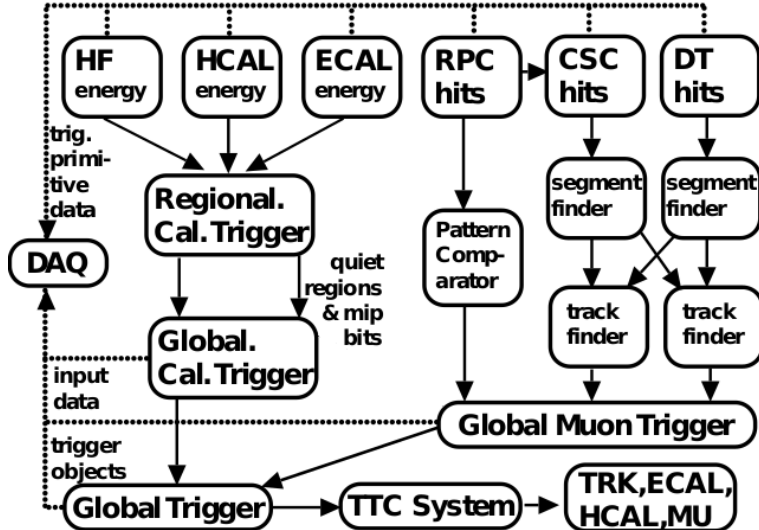


Figure 5.1: Flow of information in L1 trigger [139].

The initial interaction rate is approximately  $3.2 \mu\text{s}$ . The L1 trigger can only pass some 1 in 1000 interactions to the HLT. The L1 trigger menu has an output rate of approximately 100 kHz. L1 achieves this rate by only considering data of reduced granularity and reduced resolution. A buffer is used to store the full event data while the L1 runs. The HLT menu reduces this to about 100 Hz as required by the limit on disk writing.

The 2015 UPC triggers were for low multiplicity events and low transverse momentum events. Typical heavy-ion collisions are high multiplicity events. Hard scattering dominates. Fig.5.2 is an event display of one of the first heavy-ion collisions at CMS in 2010.

Fig.5.3 is the event display of a UPC upsilon candidate. Notice that there are only two reconstructed tracks, and that CMS is an otherwise empty detector. These events constitute a complement to those passing conventional more heavy-ion triggers.

For this analysis that focuses on coherent dijet photoproduction, the L1 trigger applies two selections. First, the L1 checks that at least one of the HF is empty. This is the most important part of the trigger as it suppressed the hadronic contamination of the dataset. Then, if there is at least 5

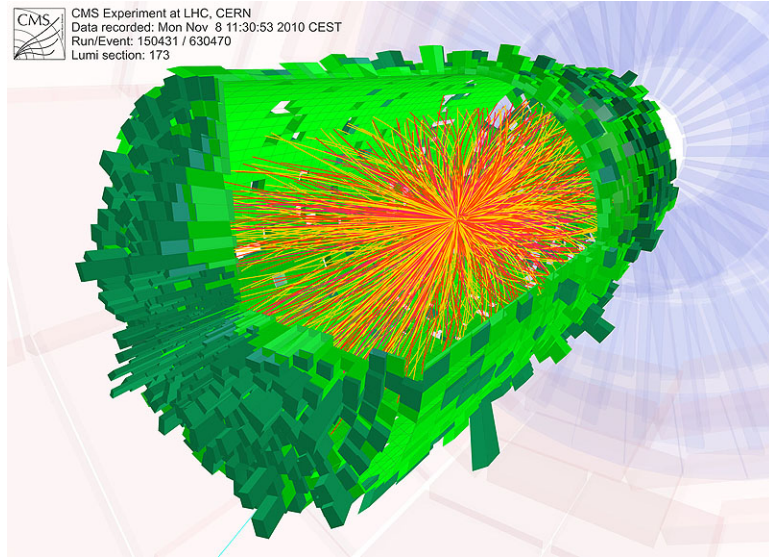


Figure 5.2: High multiplicity PbPb collision.

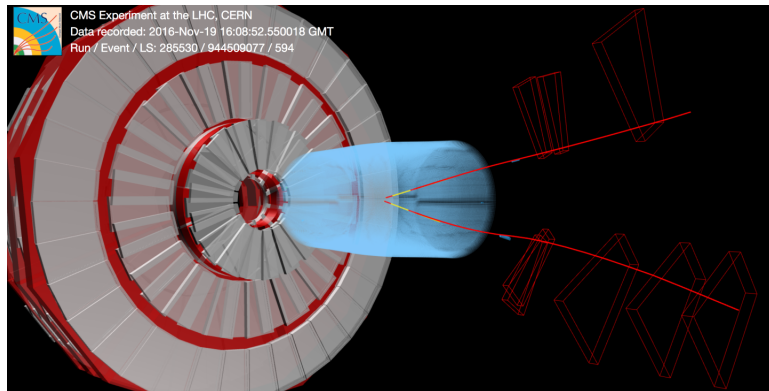


Figure 5.3: UPC Upsilon candidate.

GeV of energy deposited in the ECAL, the event passes to the HLT.

Low multiplicity events are difficult to distinguish from background. To compensate, the HLT in turn requires that there be at least one reconstructed track from the pixel tracker to ensure that there are particles that will be reconstructed by the complete tracker. Only the pixel tracker is used for these HLTs to increase the speed of reconstruction while decreasing needed computer cycles.

## 5.2 Author’s contributions

In preparation for the 2015 heavy-ion run and the 2016 p-Pb run, we prepared high-level trigger menus for the CMS Forward Heavy-Ion group. This trigger menu was optimized for firing on ultra-peripheral collisions. We tested the menu’s performance on Monte Carlo generated by STARLIGHT [79] and reconstructed through a GEANT4 [140] simulation of CMS. During the experiment, I was present at CERN to monitor the trigger rates and deliver daily reports on their performance.

The CMS software (CMSSW) includes an emulator for the L1 trigger. This software can re-emulate alternative L1 menus on previously taken CMS data. The performance of a trigger on the 2011 PbPb data, taken at  $\sqrt{s_{NN}} = 2.7$  TeV is extrapolated to the higher energy,  $\sqrt{s_{NN}} = 5.2$  TeV of the 2015 PbPb run.

The HLT menu was tested on both STARLIGHT MC and on data from the 2011 Pb+Pb run. STARLIGHT is a MC generator for ultra-peripheral collisions, in particular for the vector-meson photoproduction channels. I used STARLIGHT to generate MC sets for  $Pb + Pb \rightarrow J/\Psi + Pb + Pb$  and  $Pb + Pb \rightarrow \Upsilon(1s) + Pb + Pb$ . I then used CMSSW to test the performance of the component bits of the HLT paths with respect to these MC sets.

It was my responsibility to carefully observe the state of the UPC triggers during the heavy-ion run. If the total HLT rate ever drifted above 100 Hz, the HLT menu could crash and CMS lose considerable data. It was important for the trigger contacts to make sure that there HLT paths were behaving stably. I also analyzed express physics data to test that the vector-meson triggers saw appropriate mass resonances. Table 5.1 shows the L1 rates for a high integrated luminosity run during the 2015 PbPb period. Table 5.2 shows the HLT rates for the same run.

For the 2016 pPb run I prepared a trigger menu similar to that of the 2015 PbPb run. Table 5.3 shows the L1 rates for a high integrated luminosity run during the 2016 pPb period. Table 5.4 shows the HLT rates for the same run.

The UPC HLTs we designed are useful to study a wide variety of physics processes. In addition to the coherent dijet study that is the subject of this thesis, the data gathered through the 2015

Table 5.1: L1 Trigger Average Rates for Run 263757

L1 Type	Pre-DT Rate (Hz)	Pre-DT RMS Rate (Hz)	Post-DT Rate (Hz)	Post-DT RMS Rate (Hz)	Initial Prescale	Final Prescale
Double muon + HF veto (thresh. 1)	7.78	8.39	7.64	8.24	0	0
Double muon + HF veto (thresh. 2)	7.86	8.49	7.71	8.33	0	0
Single muon + HF veto (thresh. 2)	85.58	89.76	84.31	88.53	0	0
Double EG2 + HF veto (thresh. 2)	2.26	2.62	2.19	2.54	0	0
Single EG5 + HF veto (thresh. 2)	13.71	16.13	10.8	13.14	0	0

Table 5.2: HLT Average Rates for Run 263757

HLT Type	L1 Seed	Average Rate of HLT (Hz)
L1 pass through	Double muon + HF veto (thresh. 1)	7.64
Requires pixel track	Double muon + HF veto (thresh. 1)	1.09
L1 pass through	Double muon + HF veto (thresh. 2)	7.71
Requires pixel track	Double muon + HF veto (thresh. 2)	1.11
L1 pass through	Single muon + HF veto (thresh. 2)	22.41
Requires pixel track	Single muon + HF veto (thresh. 2)	11.18
L1 pass through	Double EG2 + HF veto (thresh. 2)	2.19
Requires pixel track	Single EG5 + HF veto (thresh. 2)	3.96

Table 5.3: L1 Trigger Average Rates for Run 285530

L1 Type	Pre-DT Rate Before Prescale (Hz)	Pre-DT Rate After Prescale (Hz)	Post-DT Rate (Hz)
Double muon + HF veto (1 Tower)	5.47	5.47	5.38
Double muon + HF veto (2 Tower)	5.47	5.47	5.38
Single muon + HF veto (1 Tower)	123.31	123.31	121.15
Single muon + HF veto (2 Tower)	123.31	123.31	121.15
Double EG2 + HF veto (1 Tower)	228.22	N/A	N/A
Double EG2 + HF veto (2 Tower)	228.22	N/A	N/A
Single EG5 + HF veto (1 Tower)	211.17	211.17	207.00
Single EG5 + HF veto (2 Tower)	211.17	211.17	207.00

trigger menu can address UPC photoproduction of coherent and incoherent  $J/\psi$ , coherent  $\psi(2s)$ , coherent  $\rho^0$ , possible  $\rho^0$  excited states, and light-by-light scattering. The 2016 trigger menu is

Table 5.4: HLT Average Rates for Run 285530

HLT Type	L1 Seed	Average Rate of HLT (Hz)
L1 pass through	Double muon + HF veto (1 Tower)	5.40
Requires pixel track	Double muon + HF veto (1 Tower)	1.20
L1 pass through	Double muon + HF veto (2 Tower)	5.40
Requires pixel track	Double muon + HF veto (2 Tower)	1.20
L1 pass through	Single muon + HF veto (1 Tower)	121.70
Requires pixel track	Single muon + HF veto (1 Tower)	58.16
L1 pass through	Single muon + HF veto (2 Tower)	121.70
Requires pixel track	Single muon + HF veto (2 Tower)	58.16
L1 pass through	Double EG2 + HF veto (1 Tower)	N/A
Requires pixel track	Double EG2 + HF veto (1 Tower)	N/A
L1 pass through	Double EG2 + HF veto (2 Tower)	N/A
Requires pixel track	Double EG2 + HF veto (2 Tower)	N/A
L1 pass through	Single EG5 + HF veto (1 Tower)	208.18
Requires pixel track	Single EG5 + HF veto (1 Tower)	159.79
L1 pass through	Single EG5 + HF veto (2 Tower)	208.18
Requires pixel track	Single EG5 + HF veto (2 Tower)	159.79

uniquely suited for studying exclusive vector meson photoproduction off the proton in pPb UPC and it is also possible to study UPC jets. All of these studies have the potential for expanding our knowledge of the nuclear gluon PDFs at small-x, from  $10^{-2}$  to  $10^{-5}$ .

# Chapter 6

## Data analysis

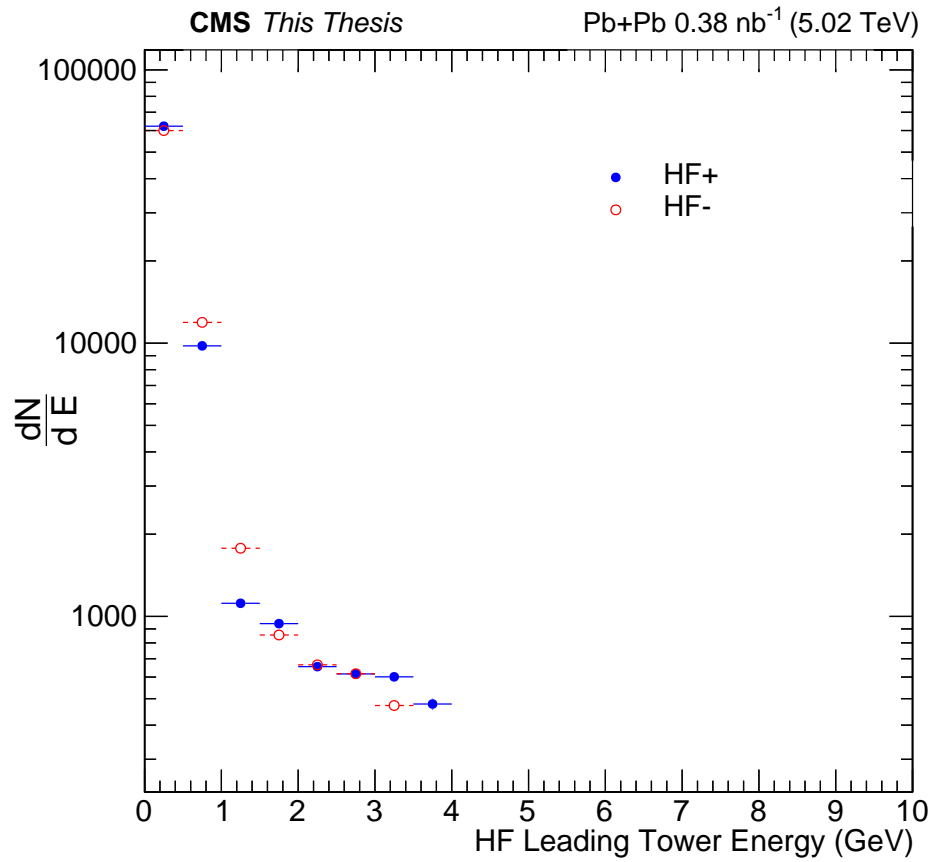


Figure 6.1: 29, 34.

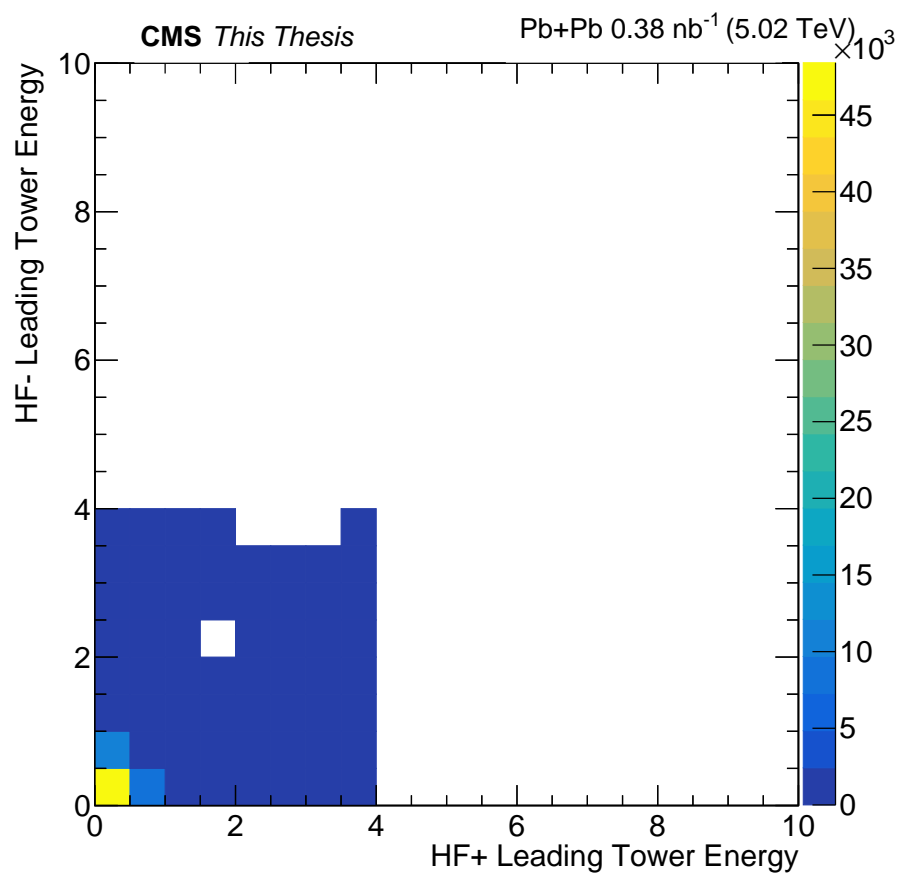


Figure 6.2: 39.

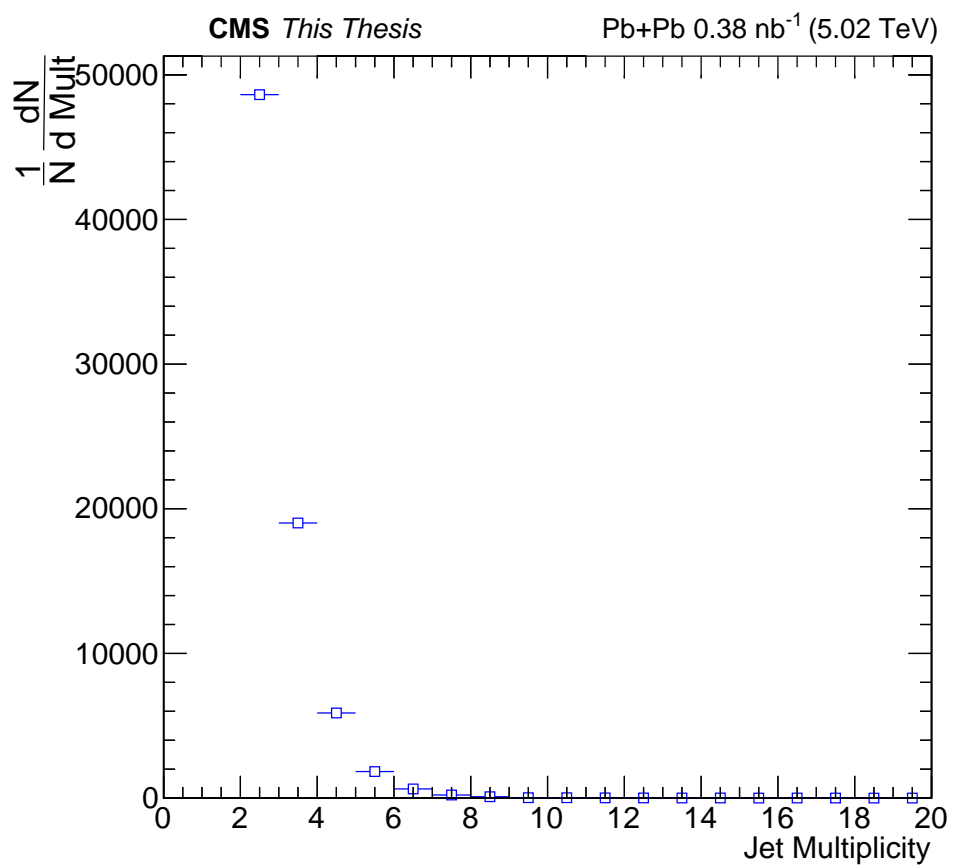


Figure 6.3: 40.

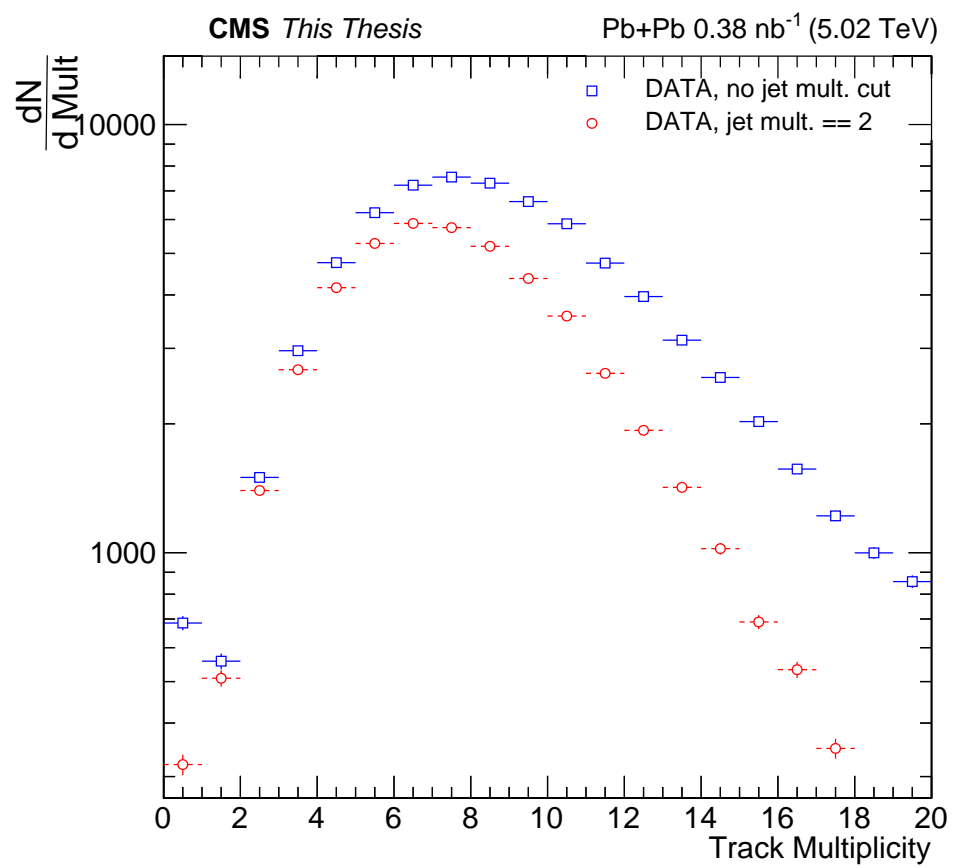


Figure 6.4: 41.

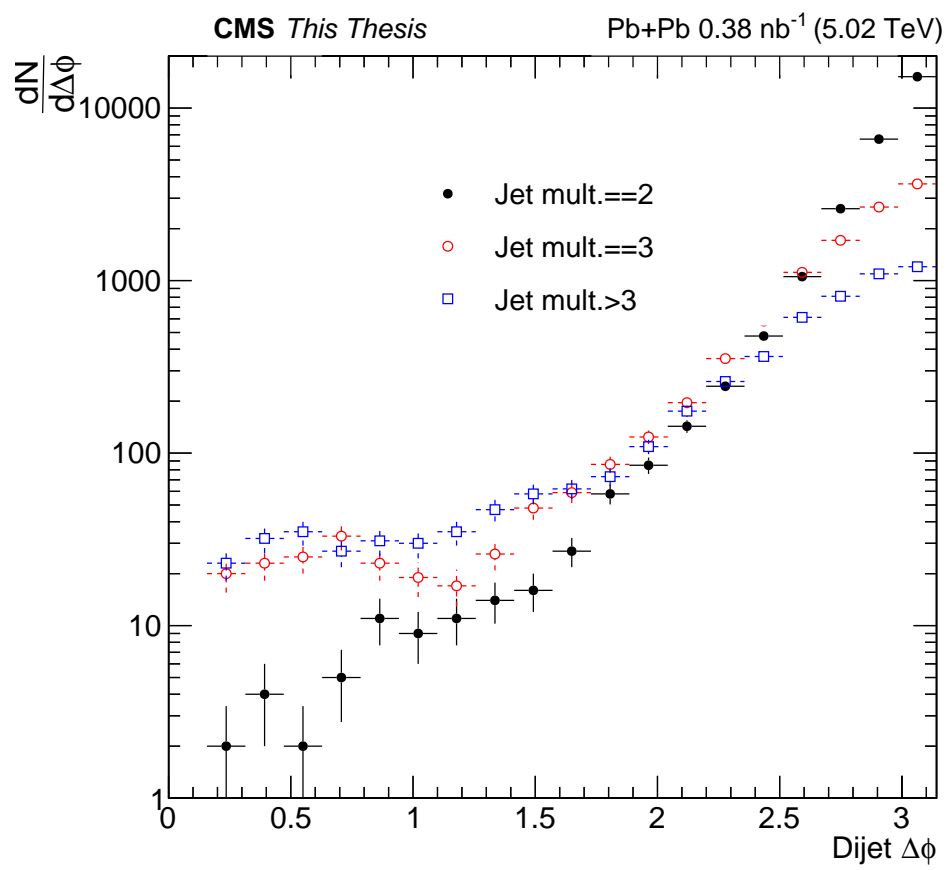


Figure 6.5: 43, 44, 45.

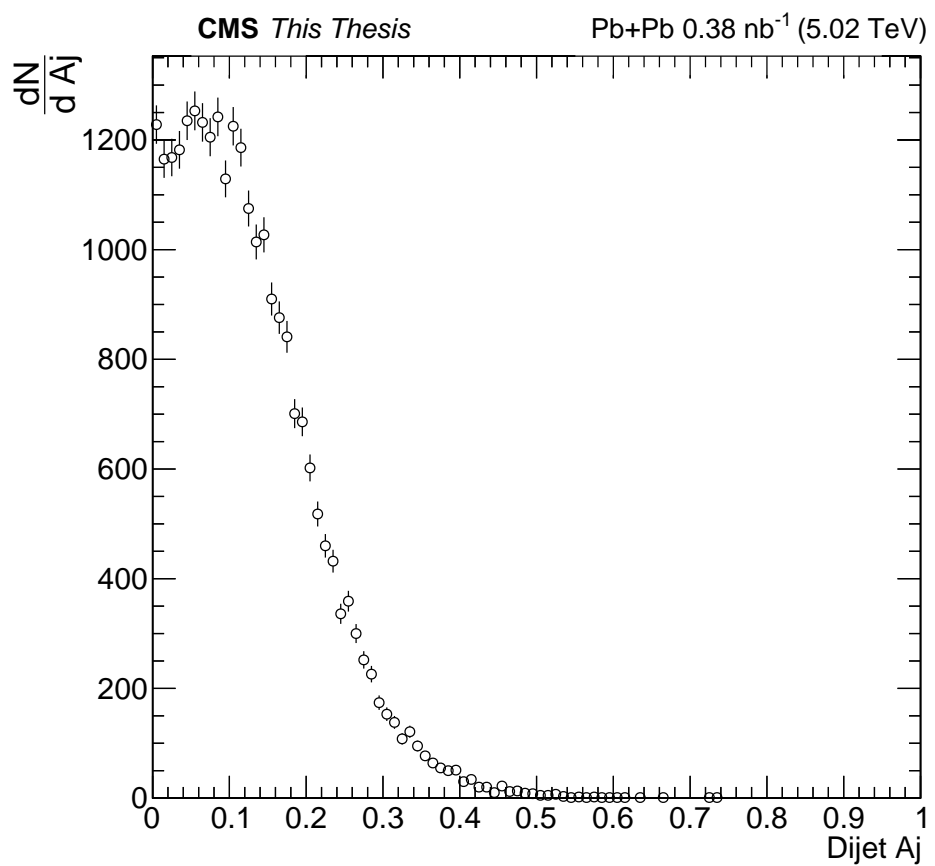


Figure 6.6: 46.

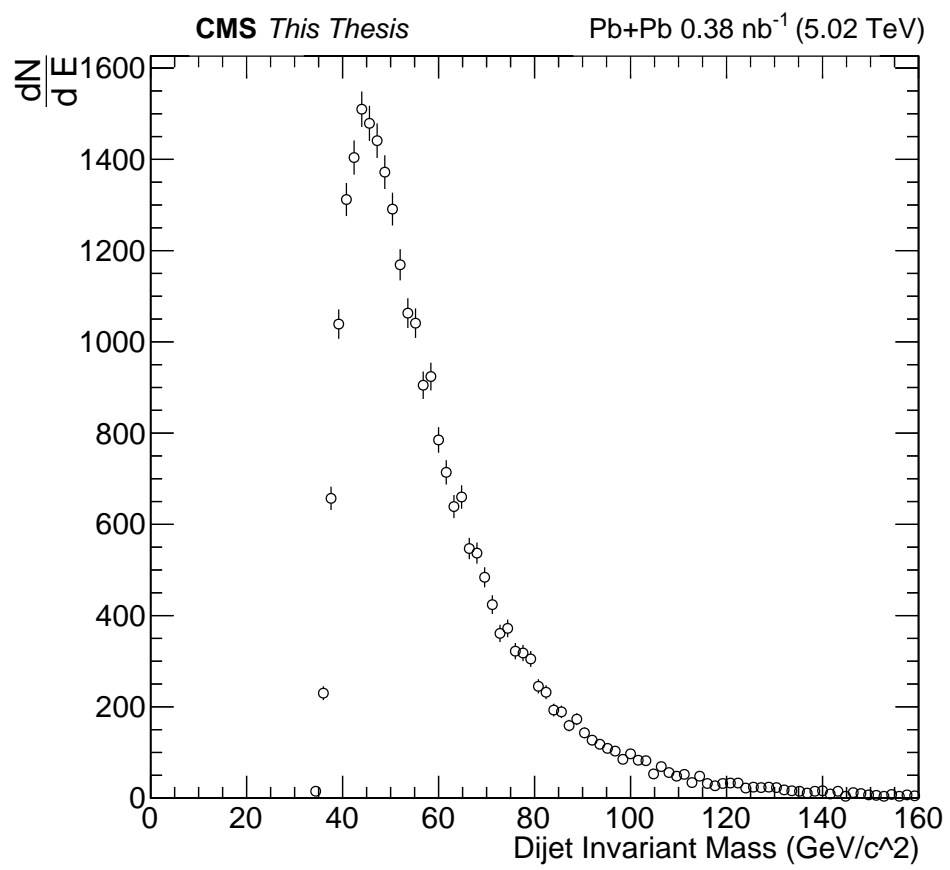


Figure 6.7: 49.

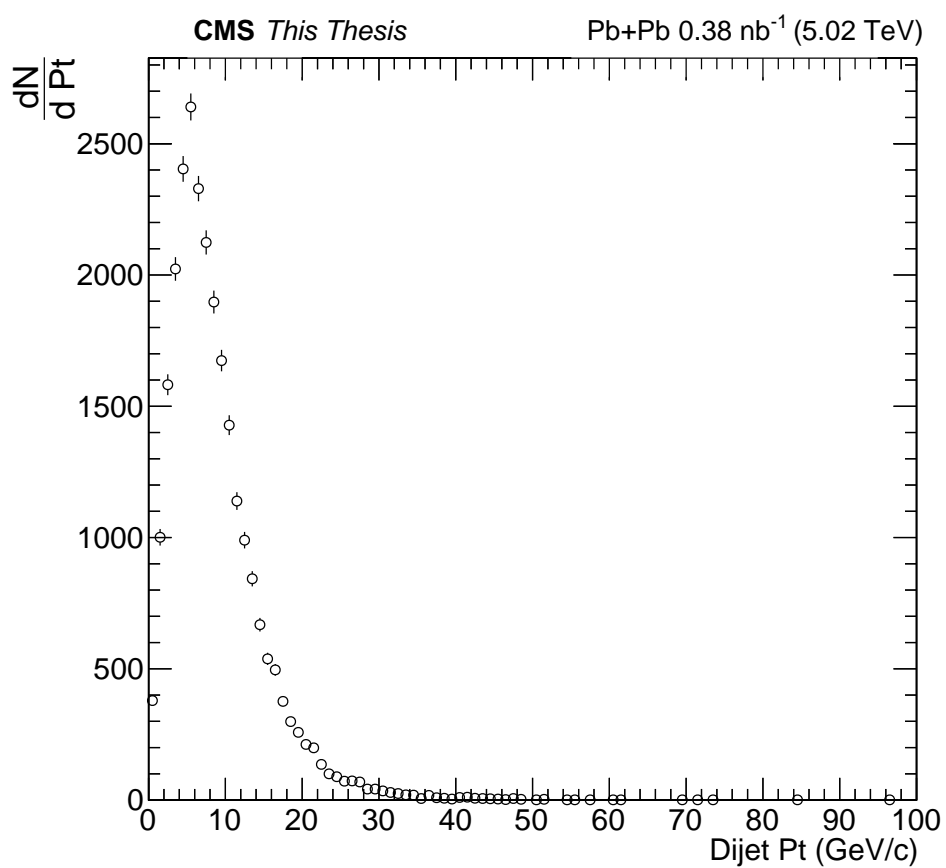


Figure 6.8: 52.

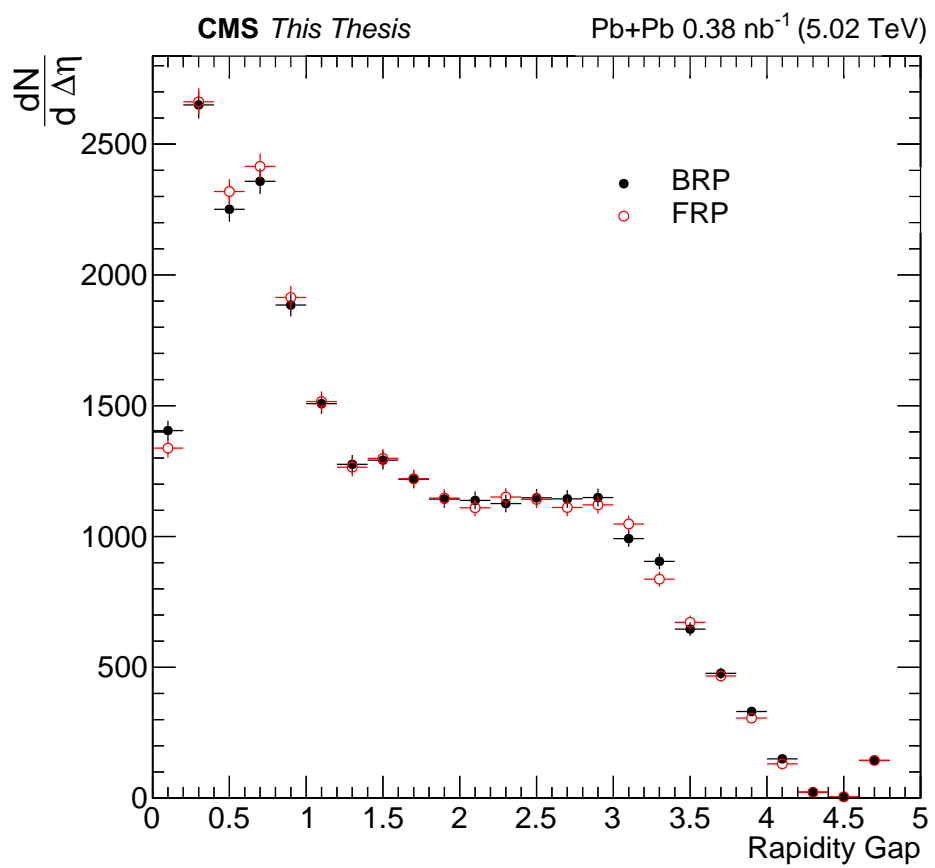


Figure 6.9: 55, 56.

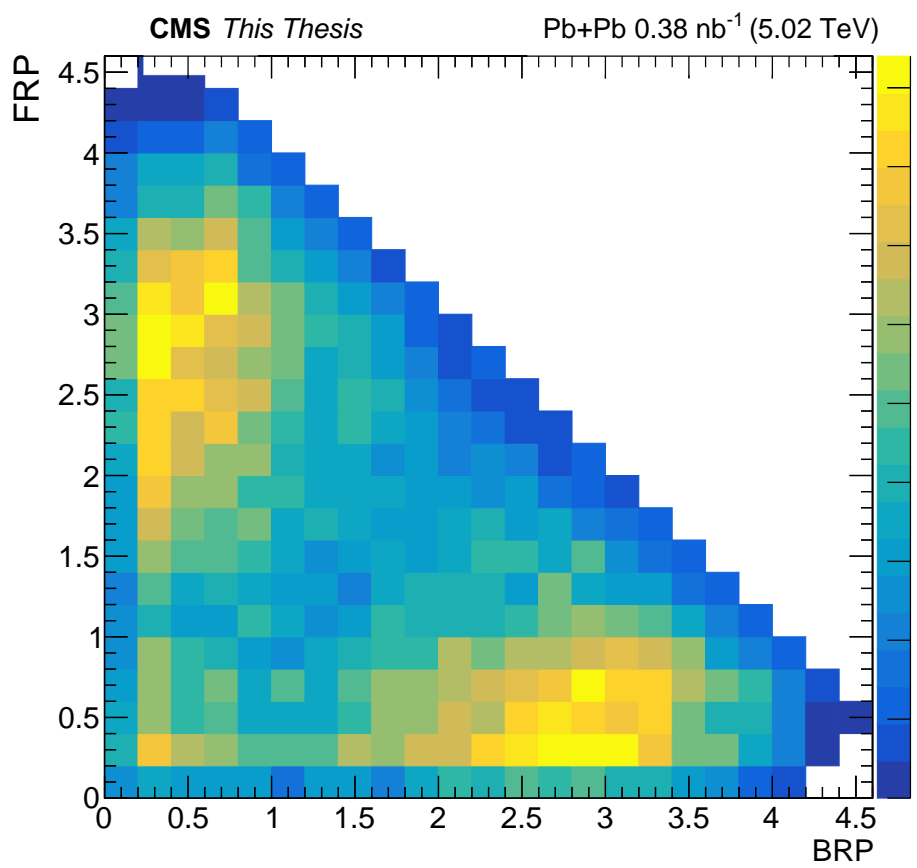


Figure 6.10: 57.

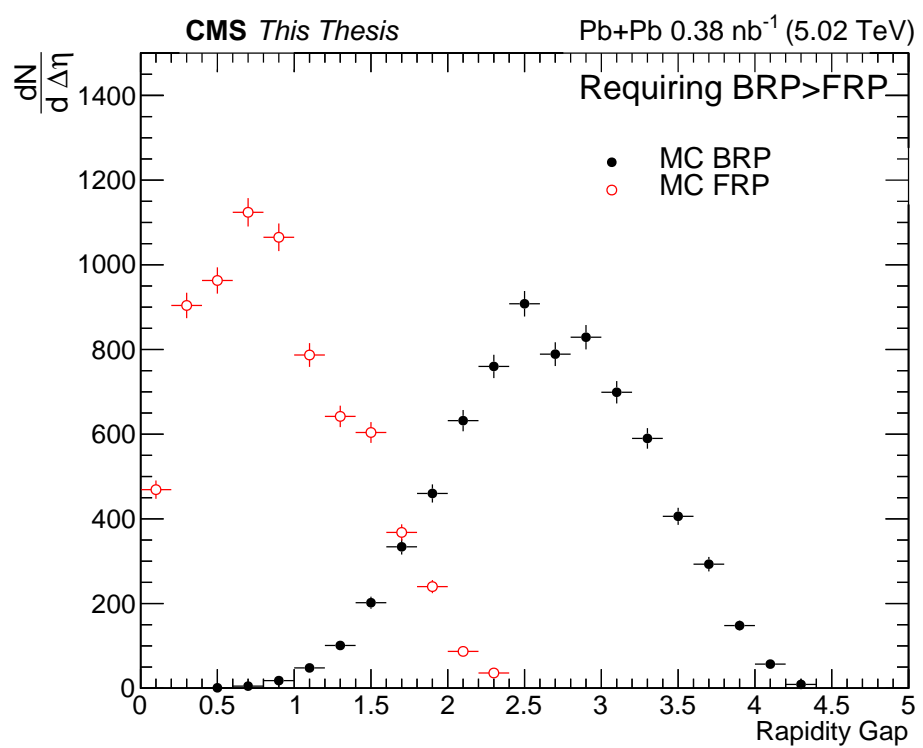


Figure 6.11: mc gap comp.

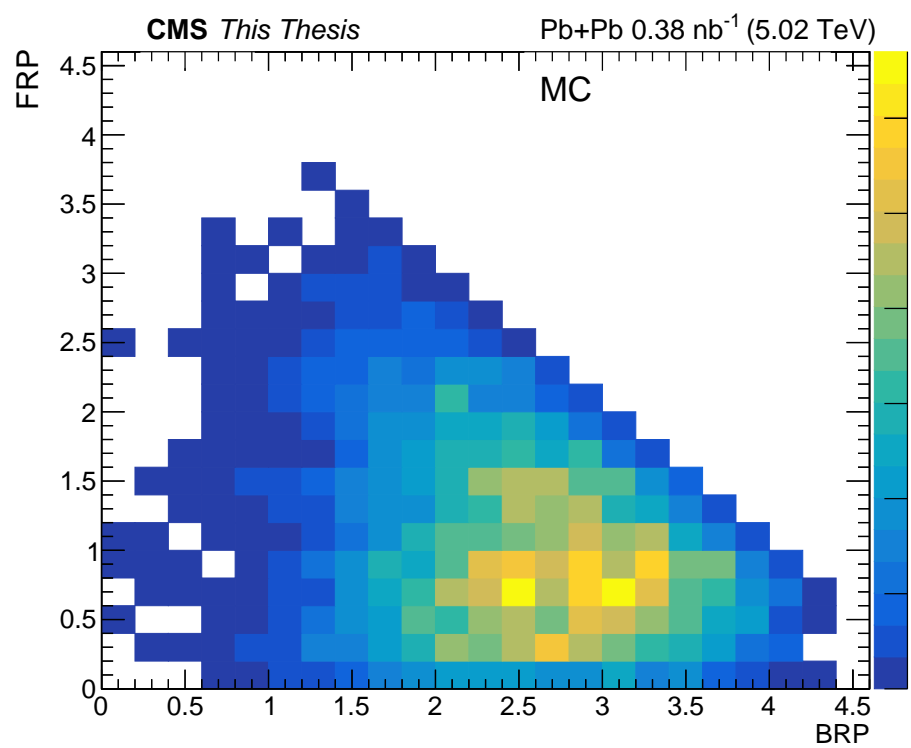


Figure 6.12: mc 2D gap comp.

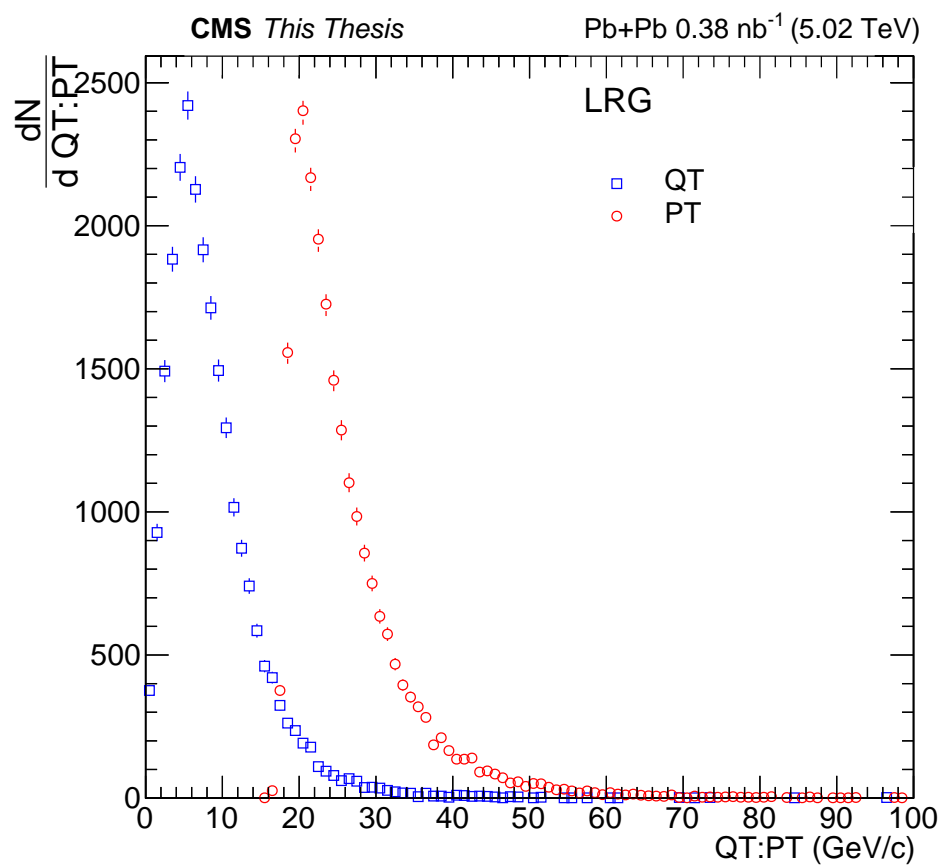


Figure 6.13: 60, 61.

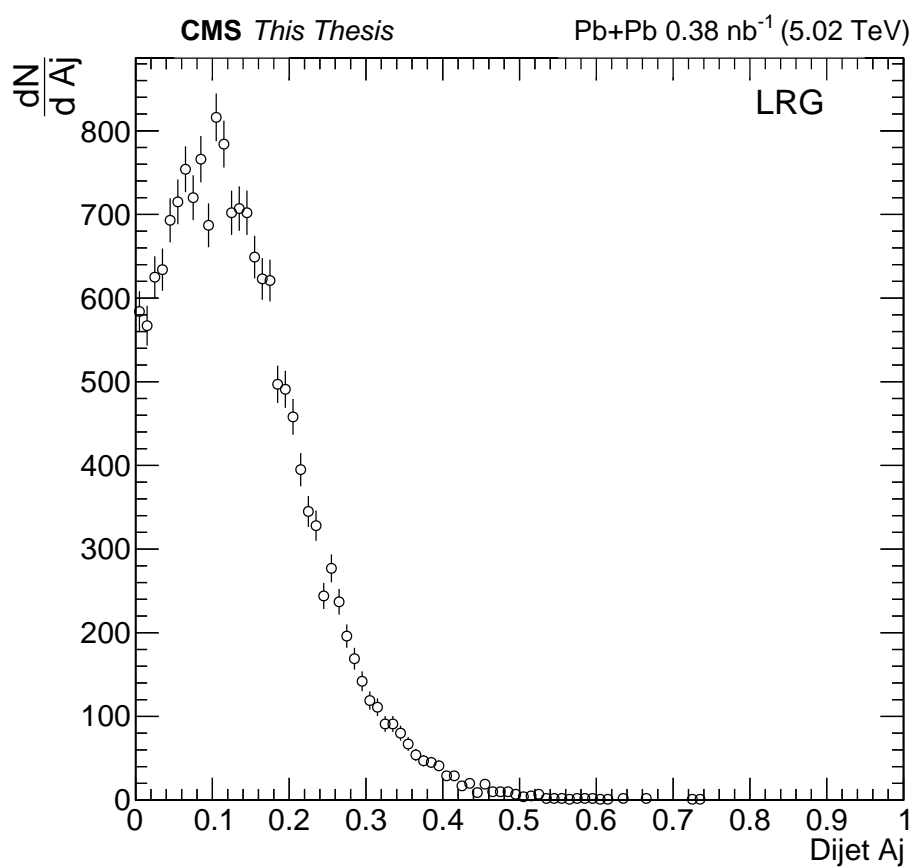


Figure 6.14: 62.

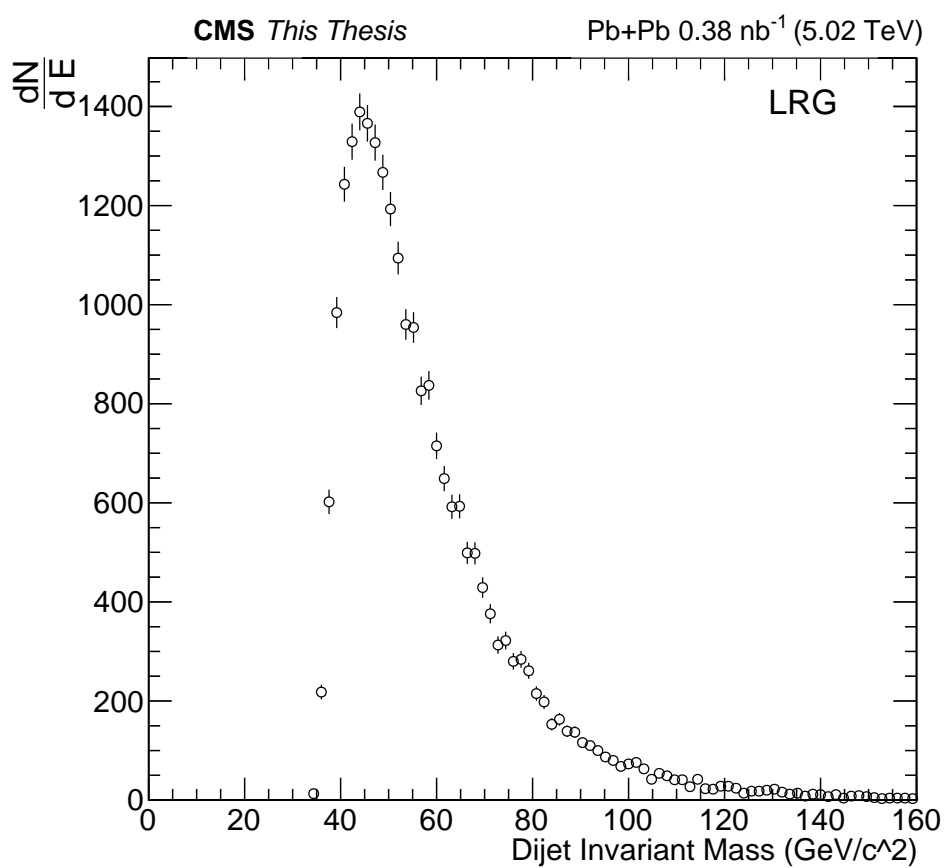


Figure 6.15: 66.

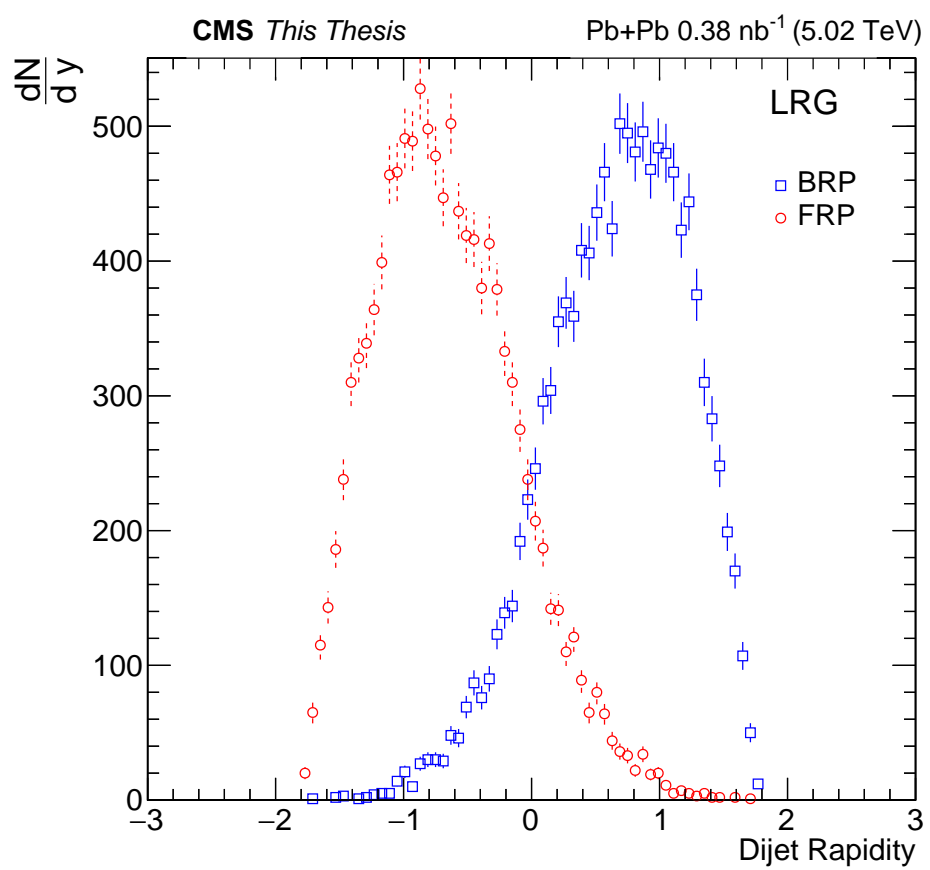


Figure 6.16: 70.

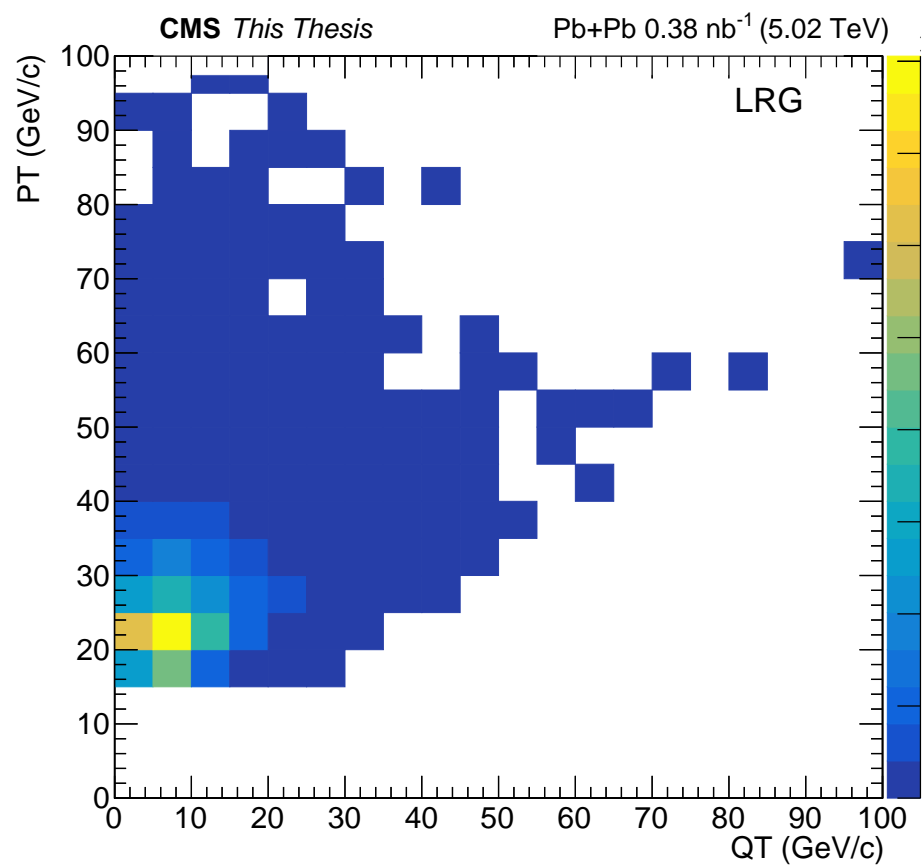


Figure 6.17: 109.

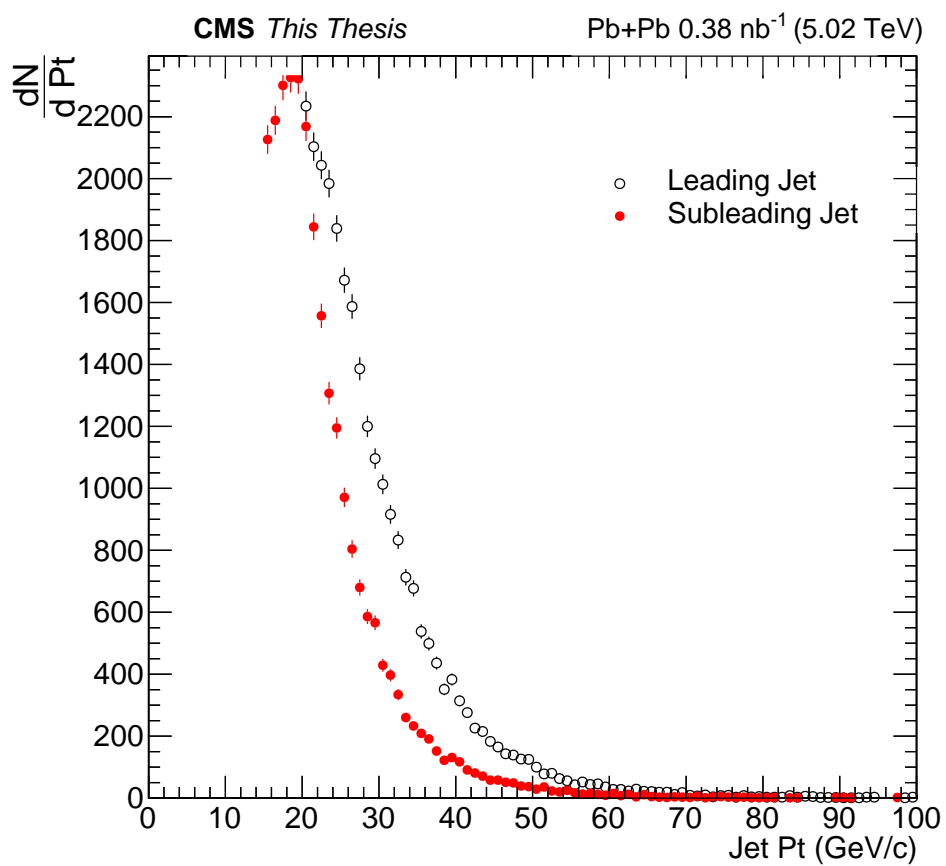


Figure 6.18: Individual Jet.

# Chapter 7

## Systematic uncertainties

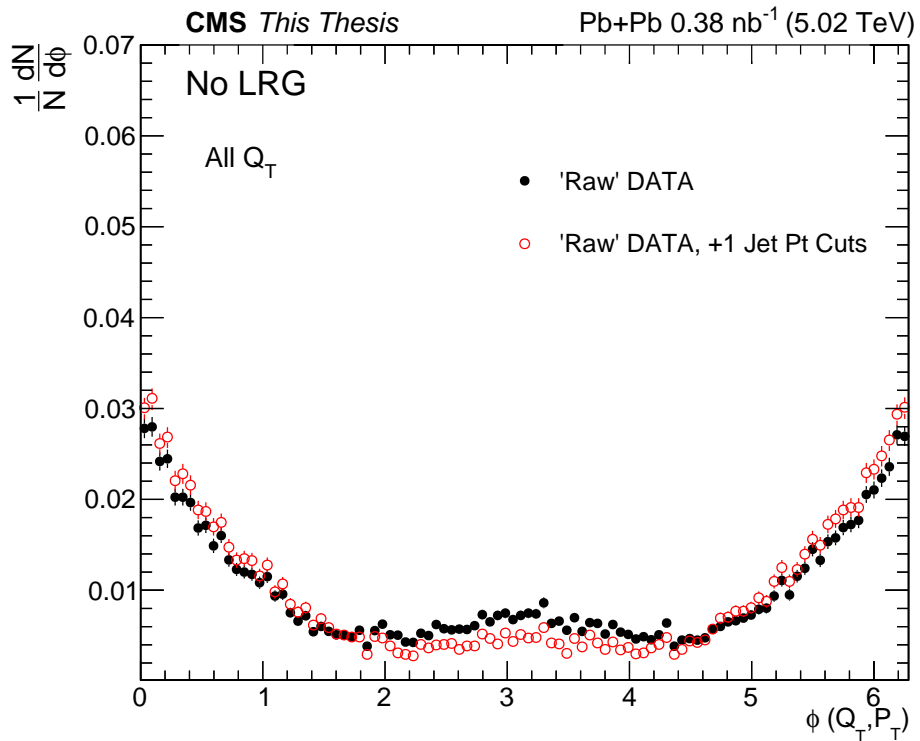


Figure 7.1: Jet Pt sys.

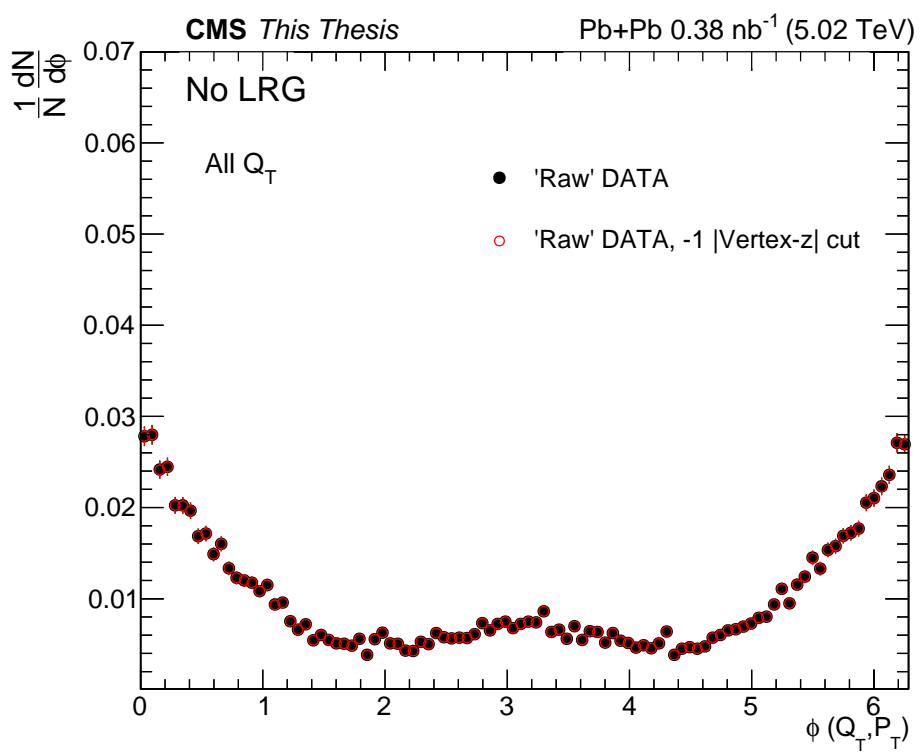


Figure 7.2: Vertex sys.

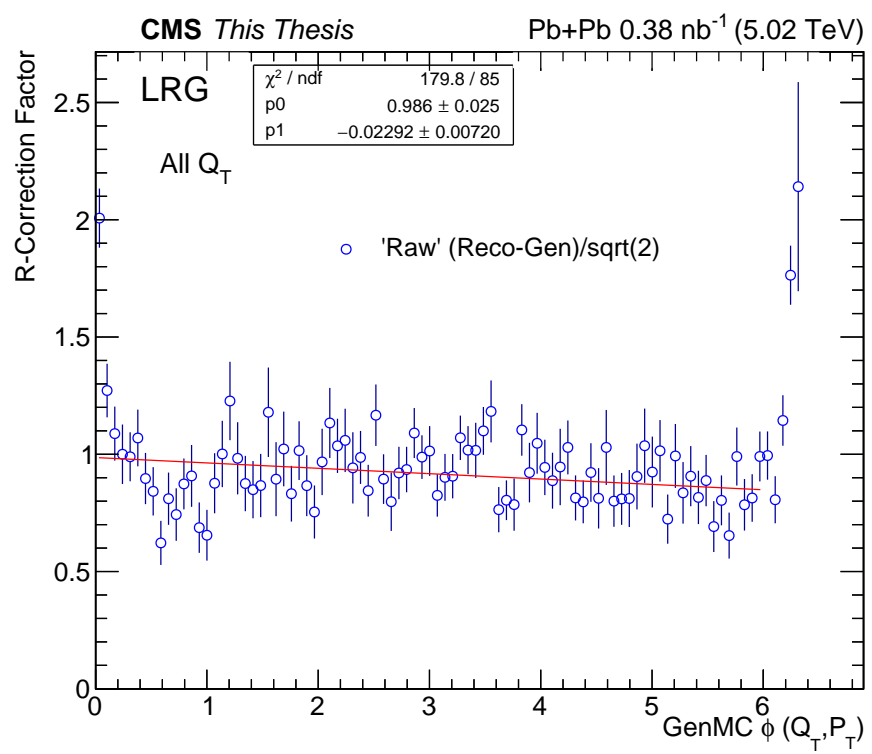


Figure 7.3: Correction factor.

# **Chapter 8**

## **Results and conclusions**

In this chapter, the angular anisotropy of the elliptic gluons is compared to theoretical predictions from variations of NLO-QCD.

## References

- [1] J. Rafelski, “Connecting QGP-Heavy Ion Physics to the Early Universe,” 2013. [Nucl. Phys. Proc. Suppl. 243-244, 155 (2013)].
- [2] I. Arsene *et al.*, “Quark gluon plasma and color glass condensate at RHIC? The Perspective from the BRAHMS experiment,” *Nucl. Phys.*, vol. A757, pp. 1–27, 2005.
- [3] “The Frontiers of Nuclear Science, A Long Range Plan,” 2008.
- [4] Y. Hagiwara, Y. Hatta, and T. Ueda, “Wigner, Husimi, and generalized transverse momentum dependent distributions in the color glass condensate,” *Phys. Rev.*, vol. D94, no. 9, p. 094036, 2016.
- [5] J. G. Contreras and J. D. Tapia Takaki, “Ultra-peripheral heavy-ion collisions at the LHC,” *Int. J. Mod. Phys.*, vol. A30, p. 1542012, 2015.
- [6] C. von Weizsäcker, “Radiation emitted in collisions of very fast electrons,” *Z. Phys.*, vol. 88, pp. 612–625, 1934.
- [7] E. Williams, “Nature of the high-energy particles of penetrating radiation and status of ionization and radiation formulae,” *Phys. Rev.*, vol. 45, pp. 729–730, 1934.
- [8] F. J. Dyson and A. Lenard, “Stability of matter. I,” vol. 8, pp. 423–434, Mar. 1967.
- [9] K. Huang, *Statistical Mechanics*. John Wiley & Sons, 2 ed., 1987.
- [10] F. Halzen and A. D. Martin, *QUARKS AND LEPTONS: AN INTRODUCTORY COURSE IN MODERN PARTICLE PHYSICS*. 1984.

- [11] M. E. Peskin and D. V. Schroeder, *An Introduction to quantum field theory*. Reading, USA: Addison-Wesley, 1995.
- [12] Y. Hatta, B.-W. Xiao, and F. Yuan, “Probing the Small-  $x$  Gluon Tomography in Correlated Hard Diffractive Dijet Production in Deep Inelastic Scattering,” *Phys. Rev. Lett.*, vol. 116, no. 20, p. 202301, 2016.
- [13] D. Griffiths, *Introduction to elementary particles*. 2008.
- [14] R. Bouchendira, P. Clade, S. Guellati-Khelifa, F. Nez, and F. Biraben, “New determination of the fine structure constant and test of the quantum electrodynamics,” *Phys. Rev. Lett.*, vol. 106, p. 080801, 2011.
- [15] G. Abbiendi *et al.*, “Measurement of the running of the QED coupling in small-angle Bhabha scattering at LEP,” *Eur. Phys. J.*, vol. C45, pp. 1–21, 2006.
- [16] M. Gell-Mann, “A Schematic Model of Baryons and Mesons,” *Phys. Lett.*, vol. 8, pp. 214–215, 1964.
- [17] R. Brock *et al.*, “Handbook of perturbative QCD: Version 1.0,” *Rev. Mod. Phys.*, vol. 67, pp. 157–248, 1995.
- [18] F. Wilczek, “QCD made simple,” *Phys. Today*, vol. 53N8, pp. 22–28, 2000.
- [19] T. Schäfer, “Phases of QCD,” in *20th Annual Hampton University Graduate Studies Program (HUGS 2005) Newport News, Virginia, May 31-June 17, 2005*, 2005.
- [20] S. Bethke, “Experimental tests of asymptotic freedom,” *Prog. Part. Nucl. Phys.*, vol. 58, pp. 351–386, 2007.
- [21] A. Deur, S. J. Brodsky, and G. F. de Teramond, “The QCD Running Coupling,” *Prog. Part. Nucl. Phys.*, vol. 90, pp. 1–74, 2016.

- [22] J. D. Bjorken, “Asymptotic Sum Rules at Infinite Momentum,” *Phys. Rev.*, vol. 179, pp. 1547–1553, 1969.
- [23] M. Thomson, *Modern particle physics*. New York: Cambridge University Press, 2013.
- [24] D. d’Enterria, “Hard spectra and qcd matter: Experimental review,” *J. Phys.*, vol. G30, pp. S767–S774, 2004.
- [25] J. Bjorken, “Highly Relativistic Nucleus-Nucleus Collisions: The Central Rapidity Region,” *Phys. Rev.*, vol. D27, pp. 140–151, 1983.
- [26] S. Shimizu, “Low  $Q^{**2}$  Structure Functions including the Longitudinal Structure Function,” in *QCD and high energy interactions. Proceedings, 44th Rencontres de Moriond, La Thuile, Italy, March 14-21, 2009*, pp. 301–304, 2009.
- [27] A. Martin, W. Stirling, R. Thorne, and G. Watt, “Parton distributions for the LHC,” *Eur.Phys.J.*, vol. C63, pp. 189–285, 2009.
- [28] K. J. Eskola, H. Paukkunen, and C. A. Salgado, “An Improved global analysis of nuclear parton distribution functions including RHIC data,” *JHEP*, vol. 0807, p. 102, 2008.
- [29] J. Pumplin, D. Stump, J. Huston, H. Lai, P. M. Nadolsky, *et al.*, “New generation of parton distributions with uncertainties from global QCD analysis,” *JHEP*, vol. 0207, p. 012, 2002.
- [30] S. Chatrchyan *et al.*, “ $\text{J}/\psi$  and  $\psi(2s)$  production in pp collisions at  $\sqrt{s} = 7$  tev,” *Journal of High Energy Physics*, vol. 2012, no. 2, 2012.
- [31] P. Paakkinen, “Nuclear parton distribution functions,” in *Old and New Strong Interactions from LHC to Future Colliders (LFC17) Trento, Italy, September 11-15, 2017*, 2018.
- [32] L. McLerran, “The Color Glass Condensate and Glasma,” 2008.
- [33] A. Accardi, V. Guzey, A. Prokudin, and C. Weiss, “Nuclear physics with a medium-energy Electron-Ion Collider,” *Eur. Phys. J.*, vol. A48, p. 92, 2012.

- [34] H. Satz, “The SPS heavy ion programme,” *Phys.Rept.*, vol. 403-404, pp. 33–50, 2004.
- [35] P. Steinberg, “Relativistic heavy ion physics: Results from AGS to RHIC,” *eConf*, vol. C020620, p. FRBT03, 2002.
- [36] H. Song, S. A. Bass, U. Heinz, T. Hirano, and C. Shen, “200  $a$  gev Au + Au collisions serve a nearly perfect quark-gluon liquid,” *Phys. Rev. Lett.*, vol. 106, p. 192301, May 2011.
- [37] R. S. Bhalerao, “Relativistic heavy-ion collisions,” pp. 219–239. 21 p, Apr 2014. Comments: Updated version of the lectures given at the First Asia-Europe-Pacific School of High-Energy Physics, Fukuoka, Japan, 14-27 October 2012. Published as a CERN Yellow Report (CERN-2014-001) and KEK report (KEK-Proceedings-2013-8), K. Kawagoe and M. Mulders (eds.), 2014, p. 219. Total 21 pages.
- [38] S. Hands, “The Phase diagram of QCD,” *Contemp.Phys.*, vol. 42, pp. 209–225, 2001.
- [39] A. Bandyopadhyay, *Non-perturbative study of spectral function and its application in Quark Gluon Plasma*. PhD thesis, Saha Inst., 2017.
- [40] E. Witten, “Cosmic Separation of Phases,” *Phys.Rev.*, vol. D30, pp. 272–285, 1984.
- [41] M. Gyulassy and M. Plumer, “Jet Quenching in Dense Matter,” *Phys.Lett.*, vol. B243, pp. 432–438, 1990.
- [42] T. Matsui and H. Satz, “ $J/\psi$  Suppression by Quark-Gluon Plasma Formation,” *Phys.Lett.*, vol. B178, p. 416, 1986.
- [43] S. Margetis, K. Safarik, and O. Villalobos Baillie, “Strangeness production in heavy-ion collisions,” *Ann.Rev.Nucl.Part.Sci.*, vol. 50, pp. 299–342, 2000.
- [44] B. Alver *et al.*, “Importance of correlations and fluctuations on the initial source eccentricity in high-energy nucleus-nucleus collisions,” *Phys. Rev. C*, vol. 77, p. 014906, Jan 2008.

- [45] S. Chatrchyan *et al.*, “Multiplicity and transverse momentum dependence of two- and four-particle correlations in pPb and PbPb collisions,” *Phys.Lett.*, vol. B724, pp. 213–240, 2013.
- [46] F. Karsch, E. Laermann, and A. Peikert, “Quark mass and flavor dependence of the QCD phase transition,” *Nucl.Phys.*, vol. B605, pp. 579–599, 2001.
- [47] B. Abelev *et al.*, “Long-range angular correlations on the near and away side in  $p$ -Pb collisions at  $\sqrt{s_{NN}} = 5.02$  TeV,” *Phys.Lett.*, vol. B719, pp. 29–41, 2013.
- [48] J.-Y. Ollitrault, “Anisotropy as a signature of transverse collective flow,” *Phys.Rev.*, vol. D46, pp. 229–245, 1992.
- [49] P. Sorensen, “Elliptic Flow: A Study of Space-Momentum Correlations In Relativistic Nuclear Collisions,” 2009.
- [50] R. Bhalerao, N. Borghini, and J. Ollitrault, “Genuine collective flow from Lee-Yang zeroes,” *Phys.Lett.*, vol. B580, pp. 157–162, 2004.
- [51] N. Borghini, P. M. Dinh, and J.-Y. Ollitrault, “Flow analysis from cumulants: A Practical guide,” 2001.
- [52] K. Ackermann *et al.*, “Elliptic flow in Au + Au collisions at  $(S(NN))^{**}(1/2) = 130$  GeV,” *Phys.Rev.Lett.*, vol. 86, pp. 402–407, 2001.
- [53] N. Borghini, R. Bhalerao, and J. Ollitrault, “Anisotropic flow from Lee-Yang zeroes: A Practical guide,” *J.Phys.*, vol. G30, pp. S1213–S1216, 2004.
- [54] U. W. Heinz, “The Strongly coupled quark-gluon plasma created at RHIC,” *J. Phys.*, vol. A42, p. 214003, 2009.
- [55] H. Wang, *Study of particle ratio fluctuations and charge balance functions at RHIC*. PhD thesis, Michigan State U., 2012.

- [56] J. D. Bjorken, “Highly relativistic nucleus-nucleus collisions: The central rapidity region,” *Phys. Rev. D*, vol. 27, pp. 140–151, Jan 1983.
- [57] R. Vogt, “Quark-Gluon Plasma Signatures,” 1998.
- [58] G. Roland, K. Safarik, and P. Steinberg, “Heavy-ion collisions at the LHC,” *Prog.Part.Nucl.Phys.*, vol. 77, pp. 70–127, 2014.
- [59] L. Frankfurt, M. Strikman, and C. Weiss, “Small- $x$  physics: From hera to lhc and beyond,” *Ann. Rev. Nucl. Part. Sci.*, vol. 55, pp. 403–465, 2005.
- [60] R. Vogt, “Heavy quark production in heavy ion colliders,” *Heavy Ion Phys.*, vol. 18, pp. 11–20, 2003.
- [61] A. Baltz, G. Baur, D. d’Enterria, L. Frankfurt, F. Gelis, *et al.*, “The Physics of Ultraperipheral Collisions at the LHC,” *Phys.Rept.*, vol. 458, pp. 1–171, 2008.
- [62] J. D. Jackson, *Classical electrodynamics*. New York, NY: Wiley, 3rd ed. ed., 1999.
- [63] C. A. Bertulani, S. R. Klein, and J. Nystrand, “Physics of ultra-peripheral nuclear collisions,” *Ann.Rev.Nucl.Part.Sci.*, vol. 55, pp. 271–310, 2005.
- [64] J. Nystrand, “Electromagnetic interactions in nucleus nucleus and proton proton collisions,” *Nucl. Phys.*, vol. A752, pp. 470–479, 2005.
- [65] M. Wilde, “Measurement of direct photons in pp and pb–pb collisions with {ALICE},” *Nuclear Physics A*, vol. 904–905, no. 0, pp. 573c – 576c, 2013. The Quark Matter 2012 Proceedings of the {XXIII} International Conference on Ultrarelativistic Nucleus-Nucleus Collisions.
- [66] V. Rebyakova, M. Strikman, and M. Zhalov, “Coherent rho and J/psi photoproduction in ultraperipheral processes with electromagnetic dissociation of heavy ions at RHIC and LHC,” *Phys.Lett.*, vol. B710, pp. 647–653, 2012.

- [67] S. Chekanov *et al.*, “Exclusive photoproduction of J / psi mesons at HERA,” *Eur.Phys.J.*, vol. C24, pp. 345–360, 2002.
- [68] M. Klasen, “Hard photoproduction at hera,” 2007.
- [69] H. Emling, “Electromagnetic excitation of the two phonon giant dipole resonance,” *Prog.Part.Nucl.Phys.*, vol. 33, pp. 729–786, 1994.
- [70] E. de Passos, M. Hussein, L. Canto, and B. Carlson, “The Mean energy, strength and width of triple giant dipole resonances,” *Phys.Rev.*, vol. C65, p. 034326, 2002.
- [71] M. Ryskin, “Diffractive J / psi electroproduction in LLA QCD,” *Z.Phys.*, vol. C57, pp. 89–92, 1993.
- [72] M. Goldhaber and E. Teller, “On nuclear dipole vibrations,” *Phys.Rev.*, vol. 74, pp. 1046–1049, 1948.
- [73] V. Goncalves and M. Machado, “Vector Meson Production in Coherent Hadronic Interactions: An update on predictions for RHIC and LHC,” *Phys.Rev.*, vol. C84, p. 011902, 2011.
- [74] C. Adler *et al.*, “Coherent  $\rho^0$  production in ultra-peripheral heavy ion collisions,” *Phys. Rev. Lett.*, vol. 89, p. 272302, 2002.
- [75] V. Guzey and M. Zhalov, “Rapidity and momentum transfer distributions of coherent  $J/\psi$  photoproduction in ultraperipheral pPb collisions at the LHC,” *JHEP*, vol. 1402, p. 046, 2014.
- [76] L. Frankfurt, M. Strikman, and M. Zhalov, “Large t diffractive  $\rho$ -meson photoproduction with target dissociation in ultraperipheral p a and a a collisions at lhc,” 2006.
- [77] A. J. Baltz, S. R. Klein, and J. Nystrand, “Coherent vector meson photoproduction with nuclear breakup in relativistic heavy ion collisions,” *Phys. Rev. Lett.*, vol. 89, p. 012301, 2002.

- [78] S. R. Klein and J. Nystrand, “Photoproduction of quarkonium in proton proton and nucleus nucleus collisions,” *Phys. Rev. Lett.*, vol. 92, p. 142003, 2004.
- [79]
- [80] B. Abelev *et al.*, “Coherent  $J/\psi$  photoproduction in ultra-peripheral Pb-Pb collisions at  $\sqrt{s_{NN}} = 2.76$  TeV,” *Phys.Lett.*, vol. B718, pp. 1273–1283, 2013.
- [81] V. Khachatryan *et al.*, “Coherent  $J/\psi$  photoproduction in ultra-peripheral PbPb collisions at  $\sqrt{s_{NN}} = 2.76$  TeV with the CMS experiment,” *Phys. Lett.*, vol. B772, pp. 489–511, 2017.
- [82] S. Klein and J. Nystrand, “Ultraperipheral nuclear collisions,” *Phys. Today*, vol. 70, no. 10, pp. 40–47, 2017.
- [83] A. Adeluyi and C. A. Bertulani, “Gluon distributions in nuclei probed at energies available at the CERN large hadron collider,” *Phys. Rev. C*, vol. 84, p. 024916, Aug 2011.
- [84] B. B. Abelev *et al.*, “Exclusive  $J/\psi$  photoproduction off protons in ultra-peripheral p-Pb collisions at  $\sqrt{s_{NN}}=5.02$  TeV,” 2014.
- [85] S. J. Brodsky, L. Frankfurt, J. Gunion, A. H. Mueller, and M. Strikman, “Diffractive lepto-production of vector mesons in QCD,” *Phys.Rev.*, vol. D50, pp. 3134–3144, 1994.
- [86] M. L. Miller, K. Reygers, S. J. Sanders, and P. Steinberg, “Glauber modeling in high energy nuclear collisions,” *Ann.Rev.Nucl.Part.Sci.*, vol. 57, pp. 205–243, 2007.
- [87] V. Guzey, E. Kryshen, M. Strikman, and M. Zhalov, “Evidence for nuclear gluon shadowing from the ALICE measurements of pbpb ultraperipheral exclusive production,” *Physics Letters B*, vol. 726, no. 1–3, pp. 290 – 295, 2013.
- [88] K. Eskola, H. Paukkunen, and C. Salgado, “EPS09: A New Generation of NLO and LO Nuclear Parton Distribution Functions,” *JHEP*, vol. 0904, p. 065, 2009.

- [89] L. Frankfurt, V. Guzey, and M. Strikman, “Leading Twist Nuclear Shadowing Phenomena in Hard Processes with Nuclei,” *Phys.Rept.*, vol. 512, pp. 255–393, 2012.
- [90] A. Adeluyi and T. Nguyen, “Coherent photoproduction of  $\psi$  and  $\Upsilon$  mesons in ultraperipheral pPb and PbPb collisions at the CERN Large Hadron Collider at  $\sqrt{S_{NN}} = 5$  TeV and  $\sqrt{S_{NN}} = 2.76$  TeV,” *Phys. Rev. C*, vol. 87, p. 027901, Feb 2013.
- [91] A. Cisek, W. Schafer, and A. Szczurek, “Exclusive coherent production of heavy vector mesons in nucleus-nucleus collisions at LHC,” *Phys.Rev.*, vol. C86, p. 014905, 2012.
- [92] V. Guzey, M. Strikman, and M. Zhalov, “Disentangling coherent and incoherent  $J/\psi$  photoproduction on nuclei by neutron tagging in ultraperipheral ion collisions at the LHC,” 2013.
- [93] M. Strikman, M. Tverskoy, and M. Zhalov, “Neutron tagging of quasielastic J/psi photoproduction off nucleus in ultraperipheral heavy ion collisions at RHIC energies,” *Phys.Lett.*, vol. B626, pp. 72–79, 2005.
- [94] V. Rebyakova, M. Strikman, and M. Zhalov, “Coherent  $\rho$  and  $J/\Psi$  photoproduction in ultraperipheral processes with electromagnetic dissociation of heavy ions at RHIC and LHC,” *Physics Letters B*, vol. 710, no. 4–5, pp. 647 – 653, 2012.
- [95] I. A. Pshenichnov, J. P. Bondorf, I. N. Mishustin, A. Ventura, and S. Masetti, “Mutual heavy ion dissociation in peripheral collisions at ultrarelativistic energies,” *Phys. Rev. C*, vol. 64, p. 024903, Jul 2001.
- [96] I. A. Pshenichnov, I. N. Mishustin, J. P. Bondorf, A. S. Botvina, and A. S. Iljinov, “Particle emission following coulomb excitation in ultrarelativistic heavy-ion collisions,” *Phys. Rev. C*, vol. 60, p. 044901, Sep 1999.
- [97] P. Chomaz, “Collective excitations in nuclei,” 1997.

- [98] M. Chiu, A. Denisov, E. Garcia, J. Katzy, A. Makeev, M. Murray, and S. White, “Measurement of mutual coulomb dissociation in  $\sqrt{s_{\text{NN}}} = 130\text{GeV}$   $au + au$  collisions,” *Phys. Rev. Lett.*, vol. 89, p. 012302, Jun 2002.
- [99] V. Andreev *et al.*, “Diffractive Dijet Production with a Leading Proton in  $ep$  Collisions at HERA,” *JHEP*, vol. 05, p. 056, 2015.
- [100] L. Frankfurt, M. Strikman, and M. Zhalov, “Elastic and large t rapidity gap vector meson production in ultraperipheral proton-ion collisions,” *Phys.Lett.*, vol. B640, pp. 162–169, 2006.
- [101] C. Alexa *et al.*, “Elastic and Proton-Dissociative Photoproduction of J/psi Mesons at HERA,” *Eur.Phys.J.*, vol. C73, p. 2466, 2013.
- [102] A. Aktas *et al.*, “Diffractive photoproduction of  $\rho$  mesons with large momentum transfer at hera,” *Phys. Lett.*, vol. B638, pp. 422–431, 2006.
- [103] F. D. Aaron *et al.*, “Measurement of the cross section for diffractive deep-inelastic scattering with a leading proton at HERA,” *Eur. Phys. J.*, vol. C71, p. 1578, 2011.
- [104] F. D. Aaron *et al.*, “Diffractive Dijet Photoproduction in  $ep$  Collisions at HERA,” *Eur. Phys. J.*, vol. C70, pp. 15–37, 2010.
- [105] A. V. Belitsky, X.-d. Ji, and F. Yuan, “Quark imaging in the proton via quantum phase space distributions,” *Phys. Rev.*, vol. D69, p. 074014, 2004.
- [106] M. Diehl, “Generalized parton distributions,” *Phys. Rept.*, vol. 388, pp. 41–277, 2003.
- [107] Y. Hatta, B.-W. Xiao, and F. Yuan, “Gluon Tomography from Deeply Virtual Compton Scattering at Small-x,” *Phys. Rev.*, vol. D95, no. 11, p. 114026, 2017.
- [108] L. Evans and P. Bryant, “LHC Machine,” *JINST*, vol. 3, p. S08001, 2008.

- [109] G. Aad *et al.*, “The ATLAS Experiment at the CERN Large Hadron Collider,” *JINST*, vol. 3, p. S08003, 2008.
- [110] K. Aamodt *et al.*, “The ALICE experiment at the CERN LHC,” *JINST*, vol. 3, p. S08002, 2008.
- [111] J. Alves, A. Augusto *et al.*, “The LHCb Detector at the LHC,” *JINST*, vol. 3, p. S08005, 2008.
- [112] V. Andreev, X. Aslanoglou, A. Azman, M. Bakirci, S. Basegmez, *et al.*, “Performance studies of a full-length prototype for the CASTOR forward calorimeter at the CMS experiment,” *Eur.Phys.J.*, vol. C67, pp. 601–615, 2010.
- [113] G. Bayatian *et al.*, “CMS technical design report, volume II: Physics performance,” *J.Phys.*, vol. G34, pp. 995–1579, 2007.
- [114] D. G. d’Enterria *et al.*, “CMS physics technical design report: Addendum on high density QCD with heavy ions,” *J. Phys.*, vol. G34, pp. 2307–2455, 2007.
- [115] L. R. F. Castillo, “The atlas and cms detectors,” in *The Search and Discovery of the Higgs Boson*, 2053-2571, pp. 4–1 to 4–8, Morgan and Claypool Publishers, 2015.
- [116] *The CMS tracker: addendum to the Technical Design Report*. Technical Design Report CMS, Geneva: CERN, 2000.
- [117] S. Chatrchyan *et al.*, “Alignment of the CMS Silicon Tracker during Commissioning with Cosmic Rays,” *JINST*, vol. 5, p. T03009, 2010.
- [118] A. Benaglia, “The CMS ECAL performance with examples,” *JINST*, vol. 9, p. C02008, 2014.
- [119] S. Baffioni, C. Charlot, *et al.*, “Electron reconstruction in cms,” *CMS NOTE 2006/40*, 2006.
- [120] G. L. Bayatian *et al.*, “CMS Physics,” 2006.

- [121] G. Baiatian *et al.*, “Design, Performance, and Calibration of CMS Hadron-Barrel Calorimeter Wedges,” 2007.
- [122] M. M. I. Bloch, E. J. A., E. D. Barge, C. Campagnari, P. Kalavase, V. Krutelyov, D. Kovalskyi, J. Ribnik, and N. Amapane, “Muon identification in cms,” *CMS Note*, vol. 2008/098, 2008.
- [123] T. C. collaboration, “Performance of cms muon reconstruction in pp collision events at  $\sqrt{s} = 7$  tev,” *Journal of Instrumentation*, vol. 7, no. 10, p. P10002, 2012.
- [124] C. Albajar, J. de Troconiz, J. Rohlf, and G. Wrochna, “Conceptual design of an improved CMS RPC muon trigger using the hadron outer scintillators,” *Nucl.Instrum.Meth.*, vol. A545, pp. 97–113, 2005.
- [125] O. A. Grachov *et al.*, “Status of zero degree calorimeter for CMS experiment,” *AIP Conf.Proc.*, vol. 867, pp. 258–265, 2006.
- [126] A. J. Baltz, C. Chasman, and S. N. White, “Correlated forward–backward dissociation and neutron spectra as a luminosity monitor in heavy-ion colliders,” *Nuclear Instruments and Methods in Physics Research Section A: Accelerators, Spectrometers, Detectors and Associated Equipment*, vol. 417, no. 1, pp. 1 – 8, 1998.
- [127] F. Beaudette, “The CMS Particle Flow Algorithm,” in *Proceedings, International Conference on Calorimetry for the High Energy Frontier (CHEF 2013): Paris, France, April 22-25, 2013*, pp. 295–304, 2013.
- [128] S. D. Ellis and D. E. Soper, “Successive combination jet algorithm for hadron collisions,” *Phys. Rev.*, vol. D48, pp. 3160–3166, 1993.
- [129] A. M. Sirunyan *et al.*, “Particle-flow reconstruction and global event description with the CMS detector,” *JINST*, vol. 12, no. 10, p. P10003, 2017.

- [130] C. Collaboration, “CMS Luminosity Based on Pixel Cluster Counting - Summer 2013 Update,” 2013.
- [131] S. Chatrchyan *et al.*, “Measurement of CMS Luminosity,” 2010.
- [132] M. W. Krasny, J. Chwastowski, and K. Slowikowski, “Luminosity measurement method for lhc: The theoretical precision and the experimental challenges,” 2006.
- [133] CMS, “Measurement of CMS Luminosity,” 2010.
- [134] A. Kornmayer, “The CMS pixel luminosity telescope,” *Nucl. Instrum. Meth.*, vol. A824, pp. 304–306, 2016.
- [135] M. Guthoff, “Instrumentation for beam radiation and luminosity measurement in the CMS experiment using novel detector technologies,” *Nucl. Instrum. Meth.*, vol. A845, pp. 565–569, 2017.
- [136] S. van der Meer, “Calibration of the Effective Beam Height in the ISR,” 1968.
- [137] S. Dasu *et al.*, “CMS. The TriDAS project. Technical design report, vol. 1: The trigger systems,” 2000.
- [138] P. Sphicas, “CMS: The TriDAS project. Technical design report, Vol. 2: Data acquisition and high-level trigger,” 2002.
- [139] V. Khachatryan *et al.*, “The CMS trigger system,” *JINST*, vol. 12, no. 01, p. P01020, 2017.
- [140] S. Agostinelli *et al.*, “GEANT4: A Simulation toolkit,” *Nucl. Instrum. Meth.*, vol. A506, pp. 250–303, 2003.

## Appendix A

### Monte Carlo Generation and Reconstruction

The Monte Carlo (MC) for this analysis was generated using the RAPGAP software package. RAPGAP is a generator for electron-proton MC. The structure functions measured at HERA are used to model a variety of diffractive processes. Each event has a characteristic energy for the virtual photon exchanged by the electron and proton. This photon energy is used to reweigh the MC to model the energy distribution of the Weizacker Williams photon flux.

$$w(E) = \frac{dN_\gamma^{eff}}{dE} / \frac{dN_\gamma^{RAPGAP}}{dE} \quad (\text{A.1})$$

$dN_\gamma^{RAPGAP}/dE$  is obtained by fitting the formula for the total electron-proton cross-section,  $\sigma_{\gamma p}$  to the RAPGAP MC's energy distribution.

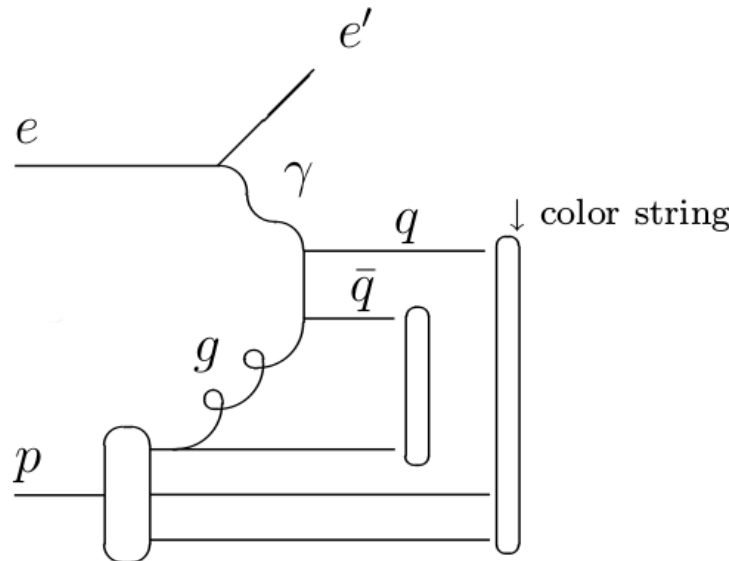


Figure A.1: RAPGAP process: boson-gluon fusion.

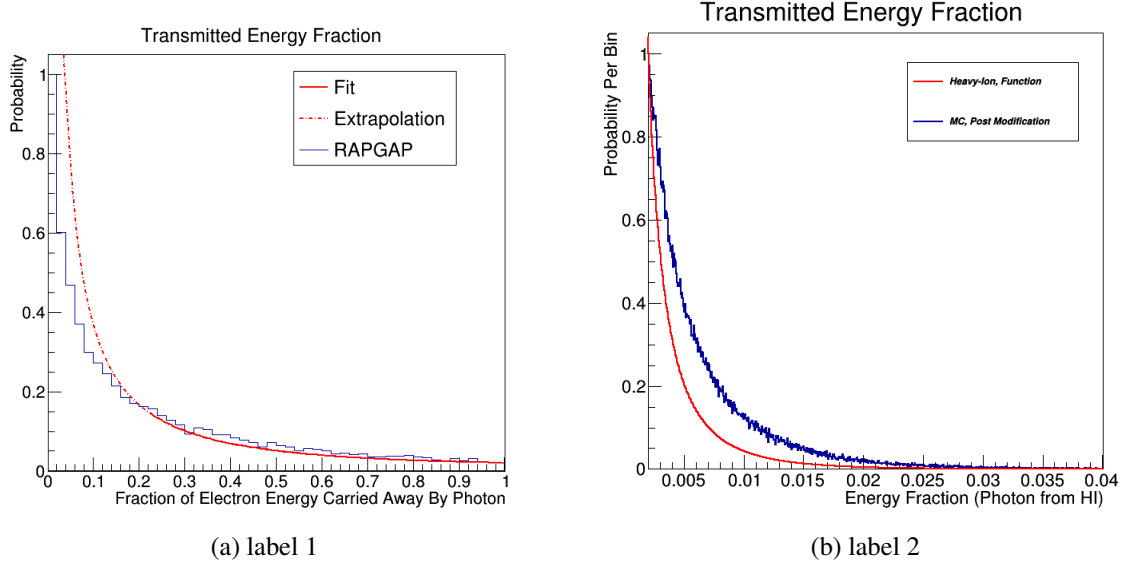


Figure A.2: Left: Energy Distribution Before Fitting, Right: Energy Distribution After Fitting

$$\frac{d^2\sigma_{ep}}{dy dQ^2} = \frac{\alpha}{2\pi Q^2} \left( \frac{1 + (1-y)^2}{y} - \frac{2(1-y)}{y} \cdot \frac{Q_{min}^2}{Q^2} \right) \cdot \sigma_{\gamma^* p}^{tot}(W_{\gamma^* p}), \quad (\text{A.2})$$

where

$$Q_{min}^2 \approx \frac{m_e^2 y^2}{1-y}. \quad (\text{A.3})$$

In this context,  $y$  is the energy fraction carried away from the electron by the mediating virtual photon,  $Q^2$  is the photon virtuality,  $m_e$  is the electron mass,  $\sigma_{\gamma^* p}^{tot}(W_{\gamma^* p})$  is the total photon-proton cross section, and  $W_{\gamma^* p}$  is the center of mass energy of the photon-proton collision.